

SEISMIC ATTENUATION ANALYSIS OF VERTICAL
SEISMIC PROFILES FOR GAS BEARING
SEDIMENTARY RESERVOIRS

MD. WAHEDUZZAMAN TALUKDER

SEISMIC ATTENUATION ANALYSIS OF VERTICAL SEISMIC
PROFILES FOR GAS-BEARING SEDIMENTARY RESERVOIRS

by

Md. Waheduzzaman Talukder

SUBMITTED IN PARTIAL FULFILLMENT OF THE
REQUIREMENTS FOR THE DEGREE OF
MASTER OF SCIENCE

AT

DEPARTMENT OF EARTH SCIENCES
FACULTY OF SCIENCE
MEMORIAL UNIVERSITY OF NEWFOUNDLAND
ST. JOHN'S, NEWFOUNDLAND

SEPTEMBER 2008

© Copyright by Md. Waheduzzaman Talukder

Abstract

Quality factor (Q) estimation of vertical seismic profiles requires precise computation of seismic energy or amplitude over a certain frequency band width of a propagating wave field through the earth media. It is a big challenge to have the correct amplitude spectra over a frequency band for reliable estimation of anelastic attenuation factor in seismic data. Q is a very useful petrophysical parameter in the characterization of different layered earth media. Estimation of Q in this study is for both numerically generated zero-offset vertical seismic profiles and field VSP. A finite difference technique has been applied to model wave propagation in elastic isotropic layered media. In finite difference modeling a staggered grid scheme is implemented in second-order in time and second-order in space that provides a convenient way to define model boundaries. For forward 2D Q analysis of model VSP and field VSP data, spectral ratio (SR) and centroid frequency down shift (CFD) methods have been used in this study. Validity and sensitivity studies of SR and CFD methods, has been done on synthetically generated model VSP data prior to attenuation analysis of field VSP data. The use of two different methods (SR and CFD methods) provides an opportunity to validate attenuation measurements. The results of the synthetic modeling studies with and without intrinsic attenuation in different models shows very close agreement with model values and validates these methods. The Q analysis

of total field VSP over the 30m depth interval, illustrates that the Q estimation is satisfactory, however a few shows a physically unrealizable phenomenon of negative values. The formation wise average Q analysis result of the field VSP indicates that the Bhuban formation is more attenuative than Tipam and Bokabil formations and the gas bearing zone (2420-2460m) has a low Q value (SR=28 and CFD=23). This highly attenuative thin gas bearing layer alters the seismic signal both in shape and size. The spectral analysis and estimated Q values of the total VSP section indicates that amplitude spectra drastically losses energy when the signal passes through the gas bearing zone.

Acknowledgements

First and foremost I must thanks to almighty God. I am indebted to many people who provided assistance through the various steps of this research. I am grateful to PPSC (Pan Atlantic Petroleum System Consortium) for financial support during the period in which this research was carried out. Thanks also due to Bangladesh Petroleum Exploration and Production Co. Ltd. (BAPEX) for providing field VSP data. I gratefully acknowledge the friendship and support to me by the faculties, staff, graduate students of the Earth Science Department during my perusal period at MUN.

It is my great pleasure to thanks my supervisor Dr. Ralph Phillip Bording, for his guidance, direction, mentoring and thoughtful input provided throughout the duration of this research work. I also extended my heartiest thanks to all of my colleagues for their cordial support, encouragement and enlightening conversation that enhanced my understanding and to solve different critical issue.

I also thanks Dr. Andreras Atle for providing valuable theoretical and practical input and helpful suggestion in solving different computational issue.

Table of Contents

Abstract	ii
Acknowledgements	iv
List of Figures	viii
List of Symbols and Abbreviations	xix
Chapter 1 Introduction	1
1.1 Introduction	1
1.2 Geological Setting	2
1.3 Previous Study and Exploration Activities	5
Chapter 2 Vertical Seismic Profiling	6
2.1 Vertical Seismic Profiling	6
2.1.1 VSP Survey	8
2.1.2 VSP Data Processing	8
2.1.3 Zero-offset VSP	10
2.2 Wave Mode Separation	10
2.3 Seismic Attenuation of VSP	13
Chapter 3 Seismic Attenuation Measurement	17

3.1	Seismic Attenuation	17
3.2	Attenuation Measurement of VSP Data	19
3.2.1	Spectral-ratio (SR) Method	20
3.2.2	Centroid Frequency Down Shift (CFD) Method	22
3.3	Factors Affecting Attenuation Measurement	25
Chapter 4	Synthetic VSP and Attenuation Model	28
4.1	Introduction	28
4.2	Synthetic Earth Models	29
4.2.1	Model Boundary Condition and Source Function	29
4.3	Single Layered Model	31
4.4	Non Attenuative Model	32
4.5	Attenuative Model	32
4.5.1	Single Layered Isotropic Model	35
4.5.2	Double Layered Model	41
4.5.3	Three Layered Model	50
4.6	Conclusion	61
Chapter 5	Forward Q Modeling of Field VSP	63
5.1	Introduction	63
5.2	Description of VSP data	63
5.3	VSP Data Acquisition	64

5.4	VSP Data Processing	65
5.5	Data Preparation for Q estimation	67
5.6	Q Computation	74
5.6.1	Application of SR and CFD Method	74
5.6.2	Spectral Ratio Method	75
5.6.3	Centroid Frequency Down Shift Method	76
5.7	Result and Discussion	76
5.8	Conclusion	86
5.9	Suggested Future Work	87
	Bibliography	88
	Appendix A Seismic modeling and finite difference formulation	90
A.1	Equations of Motion	90
A.2	Finite-difference implementation	91

List of Figures

Figure 1.1	Map showing location of major exploration wells in Bangladesh. Lalmai well-3 is indicated by star mark. Source: Petrobangla (Bangladesh Oil Gas and Mineral Corporation)	3
Figure 1.2	Generalized stratigraphic succession of Lalmai area (After: Khan, 1991)	4
Figure 2.1	Vertical seismic profiling schema illustrating (a) acquisition set up geometry (b) record of upgoing and downgoing wavefield. .	7
Figure 2.2	Generalized VSP data processing flow chart	9
Figure 2.3	Schematic diagram of principle of median filtering operation. .	12
Figure 2.4	Snell's law and mode conversion between the elastic homoge- neous half-space for (a) an incident P-wave and (b) an incident S-wave	15
Figure 3.1	Effect of geophone-formation coupling on seismic signal (Hardage, 2000).	27

Figure 4.1	Model boundary condition. The model space is made up of unit cells in 2D space. The upper boundary is free surface and the both side walls and bottom interface having absorbing boundary condition.	30
Figure 4.2	Source function, single ricker wavelet with 50Hz dominant frequency is used in seismic modeling (a) in time domain (b) in frequency domain	30
Figure 4.3	A snapshot of movie frame of wavefield within the numerical model with $V_p=3500$ m/s, $\rho=2.60$ gm/cm ³ (a) non-attenuative media (b) attenuative media ($Q=5$)	31
Figure 4.4	Non-attenuative model with $V_p=3500$ m/s, $\rho=2.60$ gm/cm ³ (a) single layer model and VSP source receiver geometry (b) total wavefield in time domain (c) windowed downgoing direct wavefield in time and frequency domain	33
Figure 4.5	Non-attenuative model with $V_p=3500$ m/s, $\rho=2.60$ gm/cm ³ (a) amplitude spectra of the traces recorded at 90m (blue) and 190m (red) depth (b) logarithmic spectral ratio of total frequency band width (c) logarithmic spectral ratio of frequency band width 20-100Hz	34

Figure 4.6	Attenuative model with $V_p=3500$ m/s, $\rho=2.60$ gm/cm ³ , $Q=5$ (a) single layer model and VSP source receiver geometry (b) total wavefield in time domain (c) windowed downgoing direct wavefield in time and frequency domain	36
Figure 4.7	Attenuative model with $V_p=3500$ m/s, $\rho=2.60$ gm/cm ³ , $Q=5$ (a) amplitude spectra of the traces recorded at 90m (blue) and 190m (red) depth (b) logarithmic spectral ratio of total fre- quency band width (c) logarithmic spectral ratio of frequency band width 20-100Hz.	37
Figure 4.8	Attenuative model with $V_p=4500$ m/s, $\rho=2.80$ gm/cm ³ , $Q=50$ (a) single layer model and VSP source receiver geometry (b) total wavefield in time domain (c) windowed downgoing direct wavefield in time and frequency domain	38
Figure 4.9	Attenuative model with $V_p=4500$ m/s, $\rho=2.80$ gm/cm ³ , $Q=50$ (a) amplitude spectra of the traces recorded at 90m (blue) and 190m (red) depth (b) logarithmic spectral ratio of total fre- quency band width (c) logarithmic spectral ratio of frequency band width 20-100Hz.	39

Figure 4.10 Illustration of centroid frequency shift of attenuative model with $V_p=3500$ m/s, $\rho=2.60$ gm/cm ³ , $Q=5$ (a) gaussian shaped amplitude spectrum of trace recorded at 90m depth where centroid frequency is 56.834671Hz (b) gaussian shaped amplitude spectrum of trace recorded at 190m depth where centroid frequency is 52.400165Hz.	40
Figure 4.11 Q modeling result where shows model value (blue line) and estimated values from SR method (red line) and CFD method (orange line) (a) attenuative model with $V_p=3500$ m/s, $\rho=2.60$ gm/cm ³ , $Q=5$ (b) attenuative model with $V_p=4500$ m/s, $\rho=2.80$ gm/cm ³ , $Q=50$	41
Figure 4.12 Double layered attenuative model with first layer: $V_p=3500$ m/s, $\rho=2.60$ gm/cm ³ , $Q=5$, and second layer: $V_p=4500$ m/s, $\rho=2.80$ gm/cm ³ , $Q=50$ (a) layer model and VSP source receiver geometry (b) total wavefield in time domain (c) windowed downgoing direct wavefield in time and frequency domain . . .	43
Figure 4.13 Double layer attenuative model is shown in the Figure-4.12 (a) amplitude spectra of the traces recorded at 90m (blue) and 190m (red) depth (b) top: logarithmic spectral ratio of total frequency band width, bottom: logarithmic spectral ratio of frequency band width 5-105Hz	44

Figure 4.14 Double layer attenuative model is shown in the Figure-4.12 (a)	
amplitude spectra of the traces recorded at 210m (blue) and	
390m (red) depth (b) top: logarithmic spectral ratio of total	
frequency band width, bottom: logarithmic spectral ratio of	
frequency band width 20-100Hz	45
Figure 4.15 Double layered attenuative model with first layer: $V_p=4500$ m/s,	
$\rho=2.80$ gm/cm ³ , $Q=50$, and second layer: $V_p=3500$ m/s, $\rho=2.60$	
gm/cm ³ , $Q=5$ (a) layer model and VSP source receiver geome-	
try (b) total wavefield in time domain (c) windowed downgoing	
direct wavefield in time and frequency domain	46
Figure 4.16 Double layer attenuative model is shown in the Figure-4.15 (a)	
amplitude spectra of the traces recorded at 90m (blue) and	
190m (red) depth (b) top: logarithmic spectral ratio of total	
frequency band width, bottom: logarithmic spectral ratio of	
frequency band width 0-100Hz.	47
Figure 4.17 Double layer attenuative model is shown in the Figure-4.15 (a)	
amplitude spectra of the traces recorded at 210m (blue) and	
390m (red) depth (b) top: logarithmic spectral ratio of total	
frequency band width, bottom: logarithmic spectral ratio of	
frequency band width 10-85Hz.	48

Figure 4.18 Q modeling result where shows model value (blue line) and estimated values from SR method (red line) and CFD method (orange line) (a) double layered attenuative model shown in the Figure-4.12a (b) double layered attenuative model shown in the Figure-4.15a	49
Figure 4.19 Three layer attenuative model with first layer: $V_p=3500$ m/s, $\rho=2.60$ gm/cm ³ , $Q=5$, second layer: $V_p=4500$ m/s, $\rho=2.80$ gm/cm ³ , $Q=50$, and third layer: $V_p=3500$ m/s, $\rho=2.60$ gm/cm ³ , $Q=5$ (a) layer model and VSP source receiver geometry (b) total wavefield in time domain (c) windowed downgoing direct wavefield in time and frequency domain.	51
Figure 4.20 Amplitude and spectral ratio of the three layered attenuative model shown in Figure-4.19 (a) amplitude spectra of the traces recorded at 90m (blue) and 190m (red) depth (b) top: logarithmic spectral ratio of total frequency band width, bottom: logarithmic spectral ratio of frequency band width 0-110Hz . .	52
Figure 4.21 Amplitude and spectral ratio of the three layered attenuative model shown in Figure-4.19 (a) amplitude spectra of the traces recorded at 210m (blue) and 390m (red) depth (b) top: logarithmic spectral ratio of total frequency band width, bottom: logarithmic spectral ratio of frequency band width 10-100Hz .	53

Figure 4.22 Amplitude and spectral ratio of the three layered attenuative model shown in Figure-4.19 (a) amplitude spectra of the traces recorded at 410m (blue) and 590m (red) depth (b) top: logarithmic spectral ratio of total frequency band width, bottom: logarithmic spectral ratio of frequency band width 0-110Hz . . 54

Figure 4.23 Three layer attenuative model with first layer: $V_p=4500$ m/s, $\rho=2.80$ gm/cm³, $Q=50$, second layer: $V_p=3500$ m/s, $\rho=2.60$ gm/cm³, $Q=5$, and third layer: $V_p=4500$ m/s, $\rho=2.80$ gm/cm³, $Q=50$ (a) layer model and VSP source receiver geometry (b) total wavefield in time domain (c) windowed downgoing direct wavefield in time and frequency domain. 56

Figure 4.24 Amplitude and spectral ratio of the three layered attenuative model shown in Figure-4.23 (a) amplitude spectra of the traces recorded at 90m (blue) and 190m (red) depth (b) top: logarithmic spectral ratio of total frequency band width, bottom: logarithmic spectral ratio of frequency band width 5-90Hz . . 57

Figure 4.25 Amplitude and spectral ratio of the three layered attenuative model shown in Figure-4.23 (a) amplitude spectra of the traces recorded at 210m (blue) and 390m (red) depth (b) top: logarithmic spectral ratio of total frequency band width, bottom: logarithmic spectral ratio of frequency band width 0-100Hz . . 58

Figure 4.26	Amplitude and spectral ratio of the three layered attenuative model shown in Figure-4.23 (a) amplitude spectra of the traces recorded at 410m (blue) and 590m (red) depth (b) top: logarithmic spectral ratio of total frequency band width, bottom: logarithmic spectral ratio of frequency band width 5-90Hz . .	59
Figure 4.27	Q modeling result where shows model value (blue line) and estimated values from SR (red line) and CFD method (orange line) (a) three layered attenuative model shown in Figure-4.19a (b) three layered attenuative model shown in Figure-4.23a . .	60
Figure 5.1	VSP acquisition geometry of Lalmai well-3.	65
Figure 5.2	Bandpass filter (5,10-100,140Hz) in frequency domain.	66
Figure 5.3	Separated total upgoing wavefield (reflected wave) of VSP from Lalmai well-3	68
Figure 5.4	Separated downgoing wavefield (direct arrival) of VSP from Lalmai well-3. Red box indicates the 120ms time window (a) total downgoing wavefield (b) 120ms windowed time section	69
Figure 5.5	Windowed downgoing wavefield (Figure-5.4b) in frequency domain.	70
Figure 5.6	Cartoon of pairing the receivers for interval attenuation estimation.	71

Figure 5.7	Amplitude spectra and spectral ratio of the traces recorded at 2480m (blue line) and 2510m (red line) depth (a) amplitude spectra (b) logarithmic spectral ratio of total frequency band width (c) logarithmic spectral ratio of 5-35Hz frequency band width	72
Figure 5.8	Amplitude spectra and spectral ratio of the traces recorded at 2540m (blue line) and 2570m (red line) depth (a) amplitude spectra (b) logarithmic spectral ratio of total frequency band width (c) logarithmic spectral ratio of 5-35Hz frequency band width	73
Figure 5.9	Showing the interpretation and correlation of VSP and logs data of Lalmai well-3. Left panel: lithologic unit in both time and depth scale, middle panel: upwave VSP event, synthetic seismogram and corridor stack data, right panel: velocity, calibrated acoustic, uncalibrated acoustic, resistivity, gamma ray, newton porosity and caliper log data. The orange lines indicate formation boundaries.	77
Figure 5.10	Display of interval velocity profile of the VSP data from 530m to 2743m depth	79

Figure 5.11 Total Q -depth profile for the VSP data of Lalmai well-3 with 30m interval from SR method (a) Q estimated over 0-35Hz frequency band width (b) Q estimated over 0-100Hz frequency band width.	80
Figure 5.12 Total Q -depth profile for the VSP data of Lalmai well-3 with 30m interval from CFD method (a) Q estimated over 0-100Hz frequency band width (b) centroid frequency-depth profile. . .	81
Figure 5.13 Total Q -depth profile for the VSP data of Lalmai well-3 with 30m interval from CFD method (a) Q estimated over frequency band width 0-108 Hz (b) centroid frequency-depth profile. . .	82
Figure 5.14 Amplitude spectra of the traces recorded at top (2420m, blue line) and bottom (2480m, red line) of the gas bearing zone (2420-2460m)	84
Figure 5.15 Showing the Q -depth profile of each individual formation and apparent Q of the gas bearing zone; SR (blue line) Q estimation is done over 0-35Hz frequency band width and CFD (red line) Q estimation is done over 0-108Hz frequency band width. . . .	85

Figure A.1 Grid tensile for staggered-grid formulation. A unit cell consists of the wavefield variables and media parameters that are defined at a specific node. The model space is then made up of series of repeated unit cells that occupy a 2D space. The indices (i, j) represent values of the spatial coordinates (x, y) and the grid spacing h is defined as the length between the centers of two adjacent grid cells. 92

List of Symbols and Abbreviations

BAPEX	Bangladesh Petroleum Exploration and Production Company Limited
CFD	Centroid Frequency Downshift
DF	Derrick Floor
ESR	Slim Single 3C Gimballed Receiver
FFT	Fast Fourier Transformation
Hz	Hertz
m	Meter
ms	Millisecond
MD	Measured Depth
MMCFD	Million Cubic Feet per Day
Q	Quality Factor
PPL	Pakistan Petroleum Limited
s	Second
SR	Spectral Ratio
TD	Total Depth
TVD	True Vertical Depth
VSP	Vertical Seismic Profile
V_p	P-wave velocity

V_s	S-wave velocity
ρ	Density
α	Attenuation coefficient

Chapter 1

Introduction

1.1 Introduction

Seismic attenuation or loss of energy in a propagating waveform through the earth media is an important parameter of the subsurface, and can provide information about rock layers. It has been long believed that attenuation is important for the characterization of rock and pore fluid properties, e.g. saturation, porosity, permeability and viscosity because amplitude attenuation is more sensitive than velocity (Best et al., 1994). Measurement of both velocity and attenuation provide complementary information about rock properties. Combined use of velocity and attenuation data in seismic analysis provides greater insight into the rock formation and the rock can be described in terms of quality factor Q or attenuation factor Q^{-1} . In practice determination of Q is much harder because the wave amplitude is highly sensitive to noise, scattering, receiver coupling effects or interference from other signals. Attenuation estimation in vertical seismic profile (VSP) is considered to be best suited as it enables sampling of the downgoing wave field at various depth levels. Our focus in this study is on forward Q modeling of field VSP data and establishing the validity of the forward modeling schemes by testing on various synthetic layered models.

There are two main sections in this study: the first section discusses synthetic seismic modeling, VSP data processing, forward Q modeling and a validity check on different synthetic models. The second section discusses the field VSP processing and Q modeling. Near zero-offset VSP data are used for both synthetic and field Q modeling. The downgoing waveform in a zero-offset VSP data set provides direct observation of the changing nature of the wavelet as it propagates through the earth media. The spectral Ratio (SR) method (Tonn, 1991) and Centroid Frequency Down shift (CFD) method (Quan and Harris, 1997) have been used to estimate compressional (P-wave) attenuation from both synthetic model VSP and field VSP. For field VSP Q modeling we used a near zero-offset VSP data set collected from Lalmai Well-3 located in the offshore Bengal Basin, eastern part of Bangladesh (Figure-1.1). Surface seismic and other exploration studies proved that the Lalmai is an anticlinal structure. These studies also highlighted a high attenuative zone of a sand dominated sequence of lower Bokabil and upper Bhuvan formation, which is the main hydrocarbon reservoir in the Bengal Basin.

1.2 Geological Setting

The Lalmai structure is situated in the Comilla district, south eastern part of Bangladesh and the exposures are composed of reddish brown clay. It is an anticlinal structure representing a north-south elongated low hill range that is approximately 16 km long and 2-3 km wide with an average height of 12m that reaches a maximum of about 47m above the mean sea level (Khan, 1991). Tectonically the Lalmai structure is situated

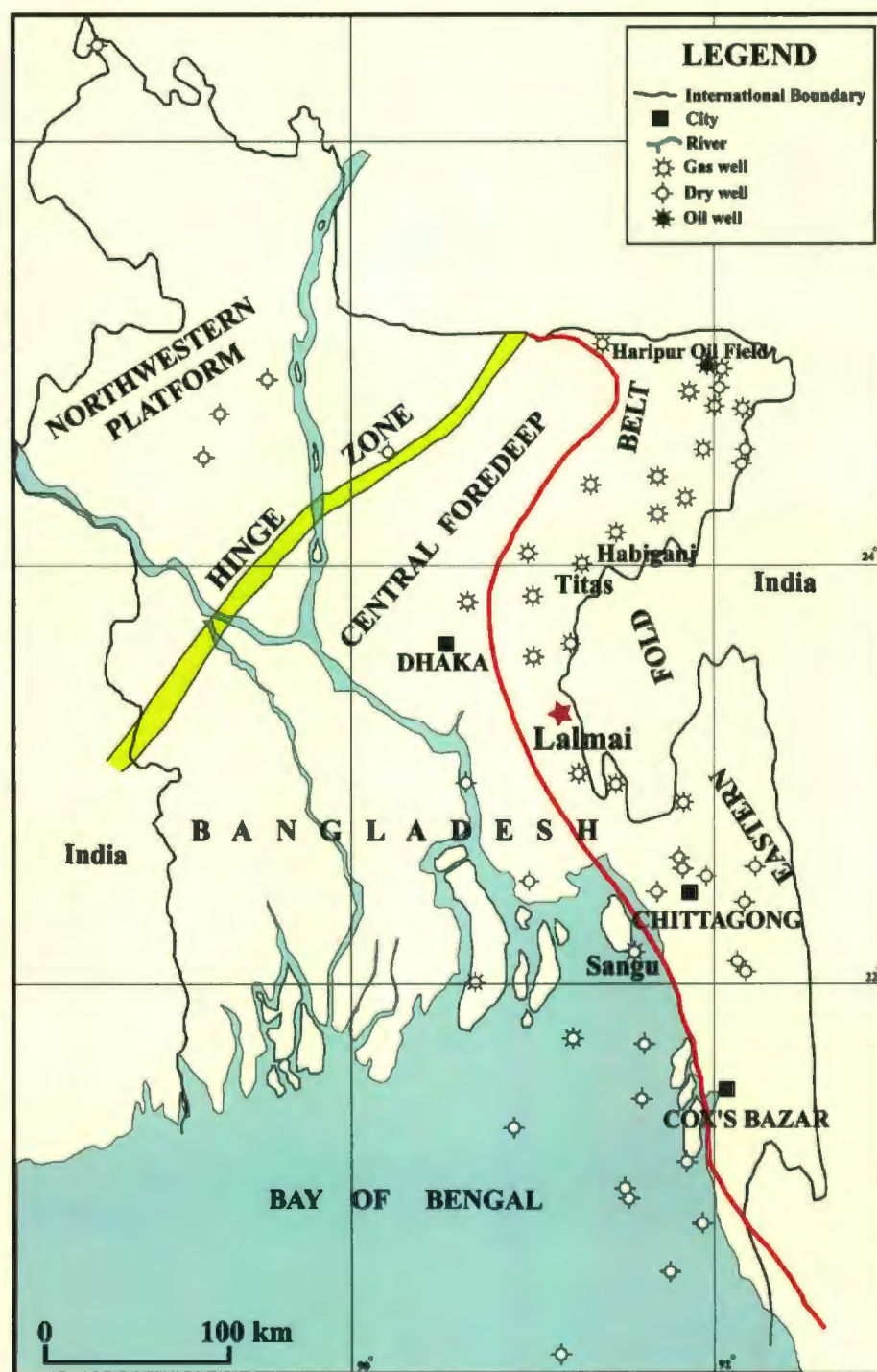


Figure 1.1: Map showing location of major exploration wells in Bangladesh. Lalmái well-3 is indicated by star mark. Source: Petrobangla (Bangladesh Oil Gas and Mineral Corporation)







Age	Group	Formation	Lithology	
Pleistocene		Madhupur Clay	Red Clay	
Plio-Miocene	Tipam	Dupi Tila	Sandstone	
		Girujan Clay	Shale	
		Tipam Sandstone	Sandstone	
Miocene	Surma	Bokabil	Shale, Sandstone	
		Bhuban	Sandstone, Shale	

Figure 1.2: Generalized stratigraphic succession of Lalmai area (After: Khan, 1991)

at the western extremity of the Eastern Folded Belt of Bengal Basin. This folded belt emerged during the last episode of the Himalayan orogene in the Mio-Pliocene age. The surface rocks of this area are covered by a thin mantle of recent alluvium. The dominant exposed rocks are the Madhupur clay and the Dupi Tila sandstone. A generalized stratigraphic section of the Lalmai region is illustrated in the Figure-1.2. The total drilled section of Lalmai structure is comprised of Madhupur clay, Dupi Tila sandstone, Girujan clay, Tipam sandstone, Bokabil and Bhuban formation of Plio-Miocene age. Dupi Tila formation is constituted of coarse to medium grain sandstone, Girujan clay is a thick marine shale and Tipam is deltaic sandstone with minor shale. Bokabil formation constitutes of marine to deltaic shale with alteration of sandstone and Bhuban is sandstone dominated formation with shale alteration. The sandstone of both the Bokabil and Bhuban formations are the main hydrocarbon reservoir of the Bengal Basin.

1.3 Previous Study and Exploration Activities

The Lalmai structure has attracted hydrocarbon explorers since 1950. Different companies acquired seismic surveys and drilled three wells in this structure. The first well was drilled in 1958 by PPL (Pakistan Petroleum Limited) down to 2993m to the Upper Bhuban; the well was dry. In 1960 PPL drilled Lalmai Well-2 down to 4117m; this well was also a dry hole (Imam and Hussain, 2002). In the 1990-1991 field session BAPEX (Bangladesh Petroleum Exploration and Production Company Limited) acquired a 12-fold 2D seismic survey over the Lalmai Structure. Later in the 2001-2002 session BAPEX acquired a 60-fold 2D seismic survey for Lalmai-Chandpur prospect identification, a joint venture project with Tullow Bangladesh Ltd. Following this seismic survey Tullow Bangladesh Ltd. drilled the Lalmai Well-3 to evaluate the potential of the large anticlinal structure. The well reached a total depth of 2800m on May 25, 2004. The well flowed dry gas at rates of up to 8.6 MMCFD from the zone at 2420-2460m. Testing was carried out over a nine-day period and no reservoir depletion was identified. The wireline logs identified potential gas-bearing sands in a number of zones between 2,200 and 2,800m depth. Production test results were encouraging (Tullow Oil plc, 2004). Then a complete logging program was designed and acquired density, velocity, acoustic, gamma ray, neutron porosity, caliper, resistivity, acoustic impedance logs for the depth range 1000 to 2743m. Near zero-offset VSP data was recorded for a depth range of 35.9 to 2743m.

Chapter 2

Vertical Seismic Profiling

2.1 Vertical Seismic Profiling

Vertical seismic profiling (VSP) is a powerful seismic measurement technique to investigate the borehole, where the receivers are placed at various depth levels attached to the wall of the borehole. The basic difference between surface seismic and the VSP is that with VSP the receivers are placed down the borehole. The VSP data recording system responds to both upgoing and downgoing seismic events. One can observe a seismic waveform that is incident upon a horizon of interest and also the resultant reflected and transmitted waveform. Because the geophones are placed far from the surface and the seismic profiles are vertical, one can observe the seismic waveform directly propagating through the earth media. The VSP technique has played an important role when used in conjunction with surface seismic for a long time and it has become widely popular to the geoscientist. VSP technique measures the one way waves and travel times rather than two way waves and travel times like surface seismic. VSP can give insight into some of the fundamental properties of propagating seismic wavelets and assist in understanding of reflection and transmission processes

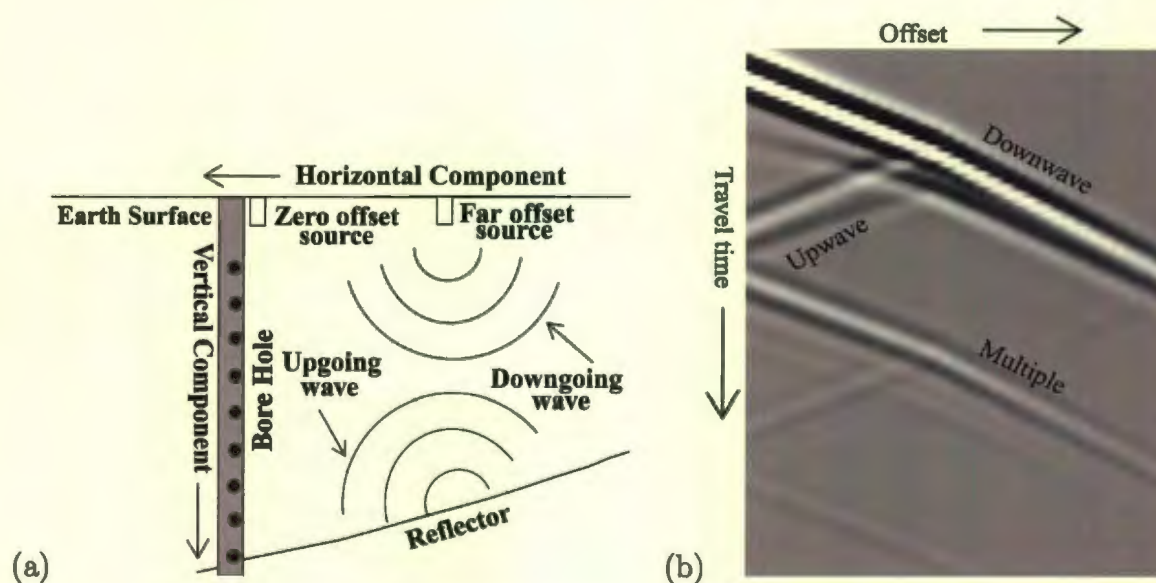


Figure 2.1: Vertical seismic profiling schema illustrating (a) acquisition set up geometry (b) record of upgoing and downgoing wavefield.

in the earth media. It can be used with the surface seismic data to improve the structural, stratigraphic and lithologic interpretation. Other uses of VSP data include the estimation of reflector dip, correlation of P-wave and S-wave reflections, location of fault planes, determination of lithologic and pore fluid effects on the propagating wavelet, identification of different order of multiples and measurement of S and P-wave velocities with their converted modes within the earth media. Before using VSP data extensive data processing is required. Most of the processing steps applied to surface seismic data can be used for VSP processing, with some minor changes. For our scheme of attenuation analysis it is very important to separate the upgoing and downgoing wave modes.

2.1.1 VSP Survey

Vertical seismic profiles are either zero-offset or far-offset depending on the type of study. The sources used in VSP studies can be explosives, air guns, or vibrators, but air guns are most widely used in VSP recording. In zero-offset VSP recording the source is placed very near to the well head and in the far-offset VSP it is placed at offset distances. The slice view of VSP survey geometry is shown in the Figure-2.1 with its recording of different modes of wave propagation.

2.1.2 VSP Data Processing

Extensive data processing is required to achieve the maximum utilization of VSP data. Shooting recording geometry, source type, seismic energy condition are the parameters that vary considerably from well to well. Each different survey requires different processing techniques. Like surface seismic data VSP data processing procedures are series of steps. Details of the processing steps necessarily vary according to the specific data set. A generalized VSP data processing flow chart is shown in the Figure-2.2. Some times additional steps are required, and in specific cases some of the steps are omitted to process data. However, typical VSP data processing steps involve editing, stacking, static correction, frequency and velocity filtering, wavelet shaping, amplitude analysis, deconvolution, transfer function calculation and impedance estimation etc.

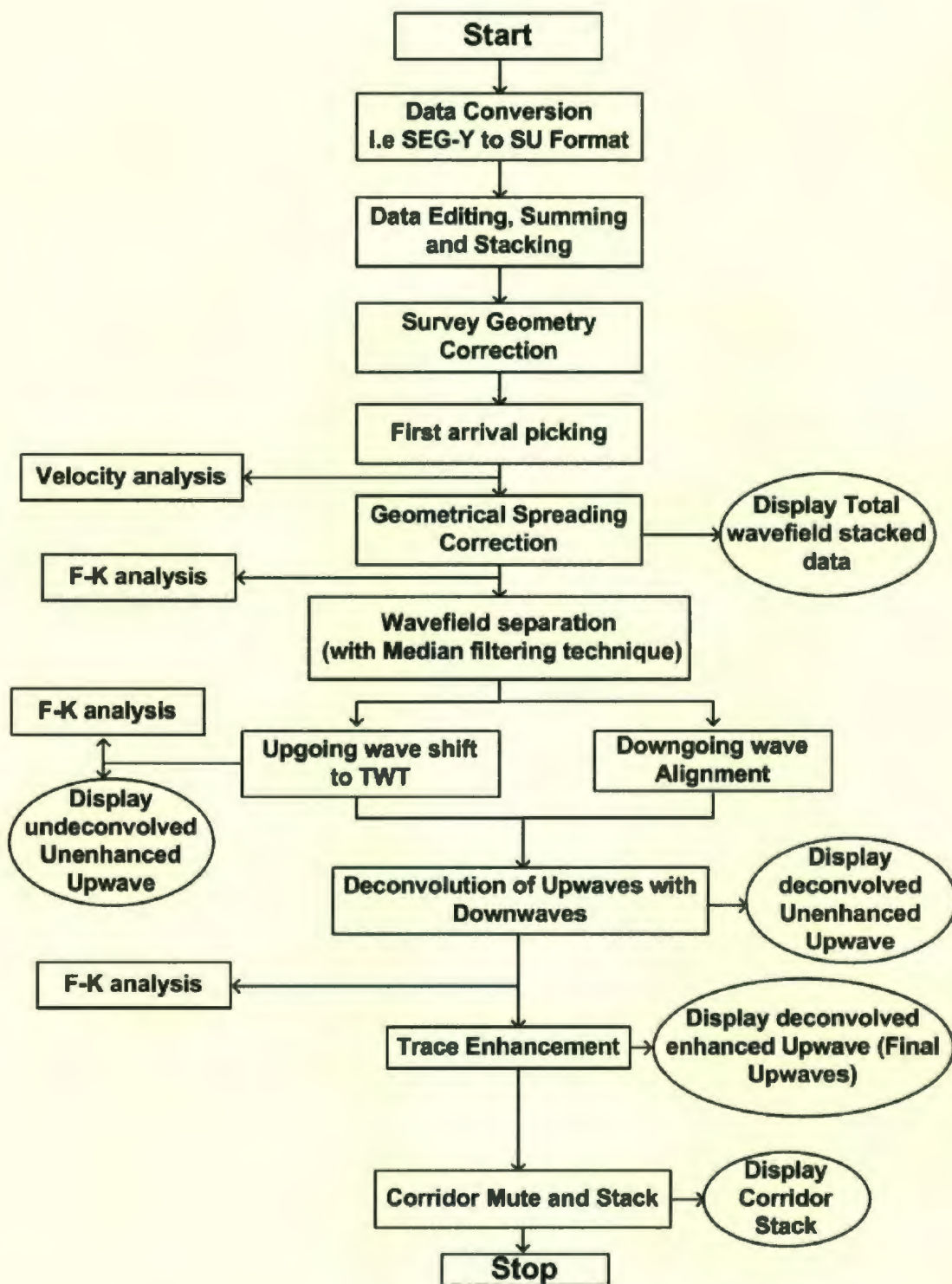


Figure 2.2: Generalized VSP data processing flow chart

2.1.3 Zero-offset VSP

Zero-offset VSP is the most common type of VSP survey. The zero-offset or near-offset VSP is defined as a VSP survey where the energy source is placed as close as possible to the well bore in an effort to focus downgoing energy in and around the bore hole from near surface to total depth (TD) and beyond. The zero-offset geometry favors the recording of reflected and direct arrivals to the borehole receivers around the well bore as well as reflected from the several thousand meters below the TD of the well. The zero-offset survey is usually done for to obtain velocity correction to allow surface seismic time-depth conversion, produce processed seismic image around the bore hole as a corridor stack and to get the shortest path of direct downgoing event. Zero-offset survey is either run alone or in conjunction with some other type of offset VSP survey. Zero-offset source VSP provides information about the subsurface only within the Fresnel zone centered at the well. On the other hand, offsetting centered the source location moves the reflection zones away from the well thus providing lateral coverage and introduces scattering in the seismic signal. So it is more reliable to estimate time and velocity in zero-offset VSP.

2.2 Wave Mode Separation

VSP data contains both up and downgoing wave modes which overlay each other in varying degrees of complexity. Separation of up and downgoing signal is one of the essential processing steps in the vertical seismic profiling. For attenuation estimation

of VSP data, wave mode separation (i.e. up and downgoing event) is one of the important and fundamental processing steps. The attenuation computation of VSP data is more reliable on its downgoing event because the downgoing event is less complicated and stronger in amplitude than the upgoing event. There are different data processing techniques that separates the upgoing and downgoing event like f-k filtering, median filtering, tau-p filtering (Solana and Schmitt, 2004). The first approach, f-k filtering, involves the design of velocity filters in frequency-wavenumber space. The tau-p filter separates coherent events in the transformed domain and allows for effective isolation of wave modes. The third approach, the median filtering technique can be used to estimate the wave mode which is to be eliminated, and this estimated mode is then subtracted from each VSP trace. Median filtering is superior to others in wave mode separation of VSP data. The median filtering technique is not widely use in surface seismic data processing but it is commonly used to separate the wave mode in VSP data. Median filter is a statistical smoothing technique explained in the Figure-2.3. The median filter operates at constant time (zero-moveout) across the data set. The filter length N refers to the number of consecutive traces over which the filter will be applied. At each time sample, the array of N samples is averaged in order of increasing amplitude. The median values occupies the $(N + 1)/2$ position of the array. An N point median filter will generate one output trace by taking the median value from N samples at each time array point. The output trace will be assigned to the position occupied by the center trace of the filter. Median filter rejects noise spikes and passes step function without altering the VSP signal. The useful

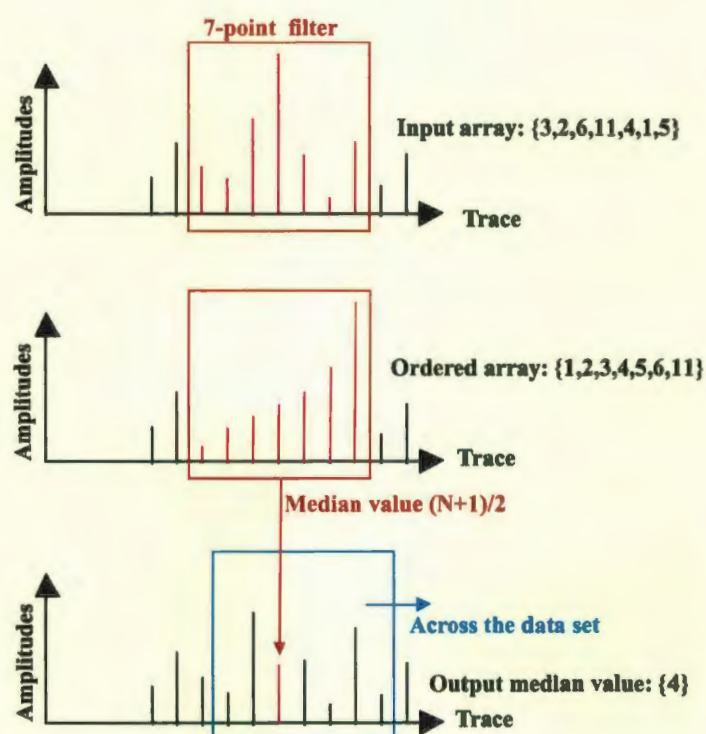


Figure 2.3: Schematic diagram of principle of median filtering operation.

properties of the median filter includes its glitch rejection (automatic rejection) and its ability to pass the step function (not smear edges). The median filter behaves similar in same ways, to a low-pass filter. If there are a few very large glitches on the traces, the median algorithm would reject them entirely while the f-k filter would spread the energy in the glitch over numerous traces. In this instance, the median filter performs better than the f-k filter. The smoothing property of the median filter constitutes an inconvenience. Hence the filter length necessary for wavefield separation must be carefully chosen and it is data dependent. The wavefield separation by median filtering is performed by as follows: the downgoing wave form is aligned by shifting each trace by the negative of the first arrival time and a median filter applied to passes downgoing waves. The estimated signal is the downgoing wave field. Upon

estimation, the downgoing wavefield is then subtracted from the input total wave field to yield the up coming wave field along with a residual noise component. The noise component can be rejected with a short median filter applied after the upwaves have been time aligned to two-way travel time. This is done by adding the first break time. The downgoing events have been separated for both synthetic zero-offset VSP and field VSP data for attenuation modeling. For downgoing wave field separation, the downgoing events were flattened by using the first arrival times. Each trace was cross correlated with a selected reference trace using a time window around the first arrival and the first arrival times were subsequently shifted to ensure maximum coherency of downgoing waves. An 11 point median filter was applied to the total wavefield to pass the flattened downgoing waves of field VSP.

2.3 Seismic Attenuation of VSP

Attenuation is the energy loss or amplitude decay of a seismic wave as it propagates through the earth media. The attenuation estimation of a seismic wave with a borehole seismic imaging technique such as VSP is more efficient than with surface seismic data. This is because VSP energy travels short paths (i.e. travel only one-way) through the earth's media, such that high frequency components of the VSP signal are attenuated less than those of the surface seismic signal. VSP data usually contains high frequency and have better signal to noise ratio at higher frequencies than do surface seismic data at a depth where the difference in the length of travel paths are

significant. The VSP techniques are widely used to determine the attenuation coefficient, anisotropy and lithology. The propagating seismic waves from source point to receiver positions are affected by different changes in amplitude, phase or frequency as a function of propagating medium. Seismic attenuation of propagating wave energy through the heterogeneous earth media varies with its different layer properties such as pore geometry, mineralogical composition, the pore fluid content and its responses to rocks. So the seismic attenuation is recognized as a potentially important measure in reservoir characterization. The attenuated zones within a sequence may contribute to apparent differences in velocity and density. The amplitude attenuation of vertical seismic events depend upon multiple factors. Geometrical spreading of seismic energy propagating from a seismic energy source is usually the major factor causing a time dependent attenuation factor. The seismic energy spreads out from the source along the surface of a sphere, which enlarges as the travel path increases. As a result, the propagating wave becomes weaker in time as we get farther from the source, but the total energy in the wave front does not change. If the media is homogeneous, the amplitude attenuation is inversely proportional to the travel distance (Sheriff and Geldart, 1995). As seismic energy propagates through the earth media, some portion of the energy reflects back and some portion is transmitted below at each impedance contrast. The reverberation of reflected events generates different sorts of multiple events from the upper layer interfaces. The multiples carry energy downward and they also produce a broadening of the downward wavelet. As well as when seismic wave hits an interface, some of its energy is reflected and some of its transmitted through

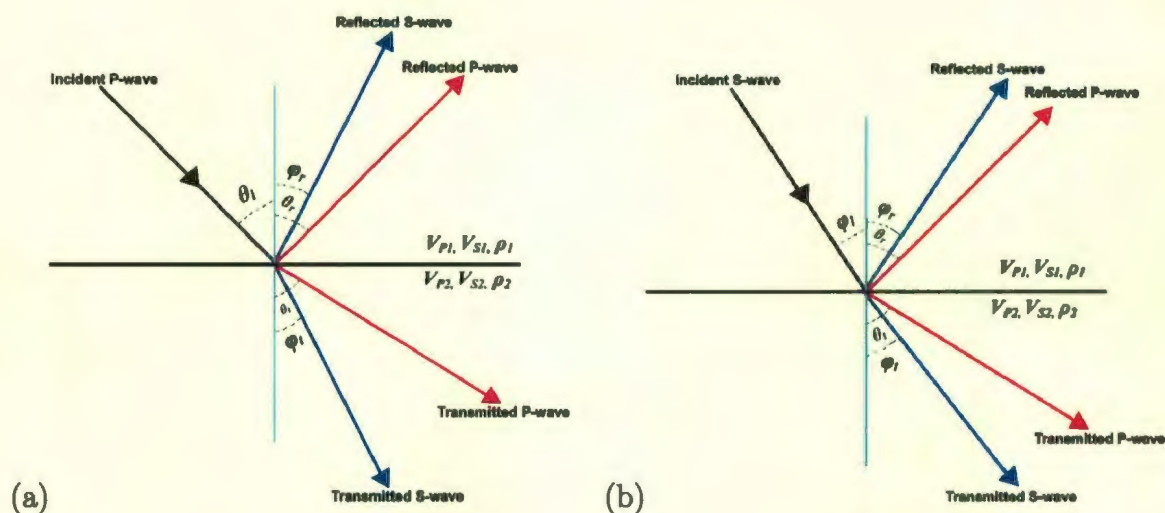


Figure 2.4: Snell's law and mode conversion between the elastic homogeneous half-space for (a) an incident P-wave and (b) an incident S-wave

the media below, and some of its will convert to a different wave mode such as P-wave and S-wave (Figure-2.4). This mode conversion effect also results in amplitude decrease of the wave energy. Scattering or diffraction occurs at irregular geometric structure such as fault-lines, pinch outs, or any other discontinuous geologic bodies. If the volume of the irregular bodies in subsurface stratigraphic unit is limited in extent, i.e. smaller than a first order Fresnel zone and have impedances that are different from their surroundings, then surface anomalies are created to scattering energy and/or diffractions of the seismic wave front. The scattering effect tends to remove the higher frequency component of the propagating wavelet and creates an overall decrease in seismic wavelet amplitude. All the effects mentioned above need to be kept in consideration for a proper attenuation measurement. The amplitude and shape of the seismic wave is not only affected by the above mentioned factors but also affected by the intrinsic attenuation due to the physical properties of rock itself

i.e. rock type, and its pore fluid properties. Absorption is the intrinsic attenuation process which removes energy from a propagating seismic wave front by means of frictional losses between oscillating rock particles, and/or pore fluid movement inside the vibrating rock pore system (Hardage, 2000). Like others factors, absorption removes higher frequency components from the wave front and reduces the amplitude. The energy loss caused due to the physical processes of rock is generally called "attenuation". This attenuation is directly related to the physical properties of rock, pore fluid content, pore structure, connectivity of pore, fracture etc. Therefore, study of seismic wave attenuation gives information about the rock and pore fluids and helps us to characterize lithologic units and their parameters and gives us some idea about overall seismic behavior. Attenuation analysis of elastic waves in VSP data has been widely used in seismic studies. The elastic absorption which depends on pore fluid type, its degree of saturation, confining pressure, connectivity and porosity has been demonstrated in the laboratory (Toksoz et al., 1979, Winkler and Nur, 1979).

Chapter 3

Seismic Attenuation Measurement

3.1 Seismic Attenuation

Wave propagation through a media implies a variation of motion (i.e. changes in energy or amplitude) in space and time. Amplitude is a measure of energy carried by a wave within a seismic signal as a high energy signal is characterized by a high amplitude; and a low energy signal is characterized by a low amplitude. The basic definition of the phenomena seismic amplitude of a plane wave propagating through a isotropic media is a function of time can be written as follows:

$$A(t) = A_0 e^{i(\omega t - kz)}. \quad (3.1)$$

where, A_0 is the initial or source amplitude spectra of the wave, $A(t)$ is the amplitude spectra of the wave after travel z distance, ω and t are angular frequency and travel time respectively. The equation (3.1) is the simplest form of seismic amplitude spectra; as it is not affected by any other factors during propagation of wave. It assumes that the seismic wave propagates through a homogeneous media where there is no energy loss. As propagating seismic wave amplitude attenuation results from different factors like geometrical spreading, transmission, scattering, reflection,

source and receiver coupling etc. Another important factor that affects amplitude of a seismic signal is the energy loss due to anelastic process or internal friction during wave propagation. So all the factors that cause energy loss in the seismic wave add up to the equation (3.1) to give the complete representation of the total energy of seismic wave. The equation can be rewrite as follows:

$$A(t) = a_0 * s(t) * r(t) * g(t) * tr(t) * e^{-(\alpha z)} e^{i(\omega t - kz)}. \quad (3.2)$$

The amplitude of a harmonic wave can be written as a product of real exponential decreasing the amplitude due to intrinsic attenuation and the imaginary exponential decreasing the oscillations. Assuming that the offset VSP source is negligible compared to the target depth and the earth is laterally homogeneous around the well bore, the amplitude spectrum, $A(z, f)$ of the windowed zero-offset VSP trace at depth z can be written as:

$$A(z, f) = S(z, f) * R(z, f) * G(z, f) * M(z, f) * T(z, f) * e^{-\pi\alpha(f)}. \quad (3.3)$$

where $S(z, f)$, $R(z, f)$, $G(z, f)$, $M(z, f)$, $T(z, f)$ are source and receiver coupling, recording system transfer function, geometrical spreading, short period multiple effect and, transmission effect respectively. The exponential term $e^{-\pi\alpha(f)}$ represents the intrinsic attenuation which is expressed as:

$$\alpha(f) = \pi f / QV. \quad (3.4)$$

The strength of intrinsic attenuation is given by a dimensionless quantity Q in term of frictional energy loss per cycle as (Aki and Richards, 1980):

$$Q(\omega) = -\frac{2\pi E}{\Delta E}. \quad (3.5)$$

where, E is the peak strain energy, and $-\Delta E$ is the energy dissipation per cycle. The term Q is sometimes called the quality factor borrowed from engineering literature. The quality factor Q , is inversely related to the attenuation coefficient α .

$$\alpha = \frac{1}{Q}. \quad (3.6)$$

3.2 Attenuation Measurement of VSP Data

Vertical seismic profiles are ideal for attenuation estimation of seismic wave because of it's favorable source-receiver geometry (Stainsby and Worthington, 1985, Dasgupta and Clark, 1998). Quality factor Q estimation can be done more efficiently on it than on surface seismic data because the surface reflection seismic data is more vulnerable to contaminate by noise. There are a broad variety of techniques available for attenuation measurement, but a few techniques are worked well in estimating anelastic attenuation measurement of VSP: the spectral-ratio method, the amplitude decay method, wavelet modeling, pulse broadening method (Tonn, 1991), centroid frequency down shift method (Quan and Harris, 1997). The spectral ratio method is the best known method for Q estimation of VSP data. In this technique the computation is done by estimating amplitude spectra at two references depths. In the amplitude decay method amplitudes are corrected for the effect of geometrical spreading and

source-receiver coupling. The remaining amplitude decay with distance is attributed to the attenuation. The pulse broadening approach measures how the width of pulse of a signal changes with distance and is unaffected by geometric spreading. This type of pulse broadening measurement can give a reliable result in separate rocks. Our scheme of attenuation estimation is focused on near zero-offset field VSP data and numerically generated zero-offset VSP data in synthetic geologic models by using SR and CFD methods.

3.2.1 Spectral-ratio (SR) Method

Spectral-ratio method is the best known technique for Q computation is described by Bath(1994), and Tonn(1991). This method is based on the assumption that the ratio of seismic amplitude spectra at two different depth levels as a function of frequency. So in SR method it is required to transform the seismic energy (or amplitude) from time domain to frequency domain. The time domain equation (3.3) has to be transformed the seismic amplitude as in frequency domain by applying Fast Fourier Transformation (FFT) to VSP data. As a result, reconstruction of equation(3.3) as function of frequency can be rewritten as:

$$A(z, \omega) = S(z, \omega) * R(z, \omega) * G(z, \omega) * M(z, \omega) * T(z, \omega) * e^{-\pi\alpha(\omega)}. \quad (3.7)$$

Here in the equation (3.7) all the parameters are same as equation (3.3) but the parameters are in as function of frequency and possesses all the factors that cause

amplitude damping or energy loss. Source and receiver $S(z, \omega)$ coupling can be omitted from equation (3.7) if in the data there is no source and receiver coupling effect or the data has been corrected for it. The geometrical spreading $G(z, \omega)$ is a function of distance, reflection $R(z, \omega)$ and transmission $T(z, \omega)$ losses are as function of incident angle and velocity. So all of these factors are not a function of frequency. For this reason, the frequency independent effects can be treated as a constant value. If the reference wavelet travel from z_1 depth to z_2 , the amplitude spectrum of this wavelet can be written as:

$$A_2(\omega, z_2) = A_1(\omega, z_1)GTRe^{-z\alpha(\omega)} \quad (3.8)$$

or

$$A_2(f, z_2) = A_1(f, z_1)GTRe^{-z\alpha(f)}. \quad (3.9)$$

where, A_1 and A_2 is the amplitude spectra of seismic signal at z_1 and z_2 depth levels; $\omega = 2\pi f$ is the angular frequency. The attenuation coefficient α is related to the inverse of quality factor Q as:

$$\alpha = Q^{-1} \frac{\pi f}{V}. \quad (3.10)$$

Therefore, the attenuation term,

$$-z\alpha = -\frac{\pi f z}{QV} = -\frac{\pi f}{Q} \left(\frac{z_2}{V} - \frac{z_1}{V} \right) = \frac{\pi f \Delta t}{Q}. \quad (3.11)$$

where, V is the phase velocity, Δt travel time from z_1 to z_2 position. By substituting the equation (3.11) into equation (3.9) and combining the geometrical spreading function (G), transmission (T) and reflection function (R) together as a constant C

we rewrite the equation (3.9) as:

$$\frac{A_2(f, z_2)}{A_1(f, z_1)} = e^{-\frac{\pi f \Delta t}{Q}} C. \quad (3.12)$$

Now taking the logarithm of both sides of equation (3.12), we get the explanation of spectral ratio method as:

$$\ln \left| \frac{A_2(f, z_2)}{A_1(f, z_1)} \right| = -\frac{\pi f \Delta t}{Q} + C. \quad (3.13)$$

The equation (3.13) states that logarithmic ratio of amplitude at two different depth levels is a linear function of frequency and the equation (3.13) can be rewritten as:

$$Y = C + (m)f. \quad (3.14)$$

A linear regression of the left hand side of equation (3.14) versus frequency therefore yields a slope, m that is equal to $-\frac{\pi \Delta t}{Q}$, and C is a single constant value. The slope m of the linear equation (3.14) yields the quality factor, Q as:

$$Q = -\frac{\pi \Delta t}{m}. \quad (3.15)$$

The equation (3.15) applied to the windowed direct arrivals of vertical component of the downgoing events of VSP for estimate Q .

3.2.2 Centroid Frequency Down Shift (CFD) Method

Centroid frequency down shift method (Quan and Harris, 1997) calculates Q from the decrease in centroid frequency of a spectrum of seismic wave traveling through an attenuative media. In comparison to some other methods of attenuation estimation,

the frequency down shift method is relatively insensitive to geometrical spreading, reflection and transmission effects, source and receiver coupling, radiation pattern and instrumental responses. Seismic attenuation includes intrinsic attenuation and scattering attenuation. Both of them can cause wave dispersion. In the frequency shift method, wave dispersion is used as the observed signal for attenuation estimation. In most natural material, the high frequency component of seismic signal attenuates more rapidly than the low frequency component as the wave propagates. As a result, the centroid frequency of the signal's spectrum experiences a down shift during propagation. The frequency shift method is applicable to any seismic survey geometry where signal bandwidth is broad enough and the attenuation is high enough to cause noticeable losses of high frequency during propagation. In the spectral ratio method the computation of attenuation based on individual frequencies is not robust because of poor signal to noise ratio. Amplitude averaging over a range of frequency can be improve the signal to noise ratio (White, 1992). As considering that the process of wave propagation can be described by linear system theory, if the amplitude spectrum of an incident wave is $S(f)$, and medium and instrument response is $G(f).H(f)$. The receiver power spectrum $R(f)$, can be express as

$$R(f) = S(f).G(f).H(f) \quad (3.16)$$

where, $G(f)$ is the factor that lumps together geometric spreading, source receiver coupling, radiation, reflection and transmission coefficients and the phase accumulation due to wave propagation and $H(f)$ describes the attenuation effect. The factor

G includes many complicated process and it is very difficult to determine. To minimize these difficulties, a statistical method is used to estimate attenuation from the spectral centroid down shift over a range of frequency (Quan and Harris, 1997). The centroid frequency of input or source signal $S(f)$ and received signal $R(f)$ are defined by integral equations as:

$$f_S = \frac{\int_0^\infty f S(f) df}{\int_0^\infty S(f) df} \quad (3.17)$$

and

$$f_R = \frac{\int_0^\infty f R(f) df}{\int_0^\infty R(f) df}. \quad (3.18)$$

The variances of the source and received signals are defined as follows:

$$\sigma_S^2 = \frac{\int_0^\infty (f - f_S)^2 S(f) df}{\int_0^\infty S(f) df} \quad (3.19)$$

and

$$\sigma_R^2 = \frac{\int_0^\infty (f - f_R)^2 S(f) df}{\int_0^\infty R(f) df}. \quad (3.20)$$

Where, $R(f)$ is given by equation (3.16). If G is independent of frequency f , then f_R and σ_R^2 will be independent of G . This is the major advantage of using spectral centroid and variance rather than actual amplitude. Therefore, the centroid frequency shift f_C , of source and received signals can be written as:

$$f_C = f_S - f_R. \quad (3.21)$$

The centroid frequency shift and variance of first arrival wavelet is used to calculate attenuation. The Q estimation of zero-offset VSP data is done by the following

equation (Quan and Harris, 1997).

$$Q_s = \frac{\pi \sigma_s^2 \Delta t}{f_c}. \quad (3.22)$$

where, f_c is the centroid frequency difference between source and received signal and Δt is the travel time from source to receiver and σ_s^2 is the variance of the source signal. If two consecutive receivers i and $(i + 1)$ are placed in two different depth levels, the Q between those depth levels is defined according to the equation (3.22) as:

$$Q_i = \frac{\pi \sigma_i^2 \Delta t_i}{f_i}. \quad (3.23)$$

Where, $\Delta f_i = f_i - f_{(i+1)}$ is the centroid frequency difference between two depth levels, $\Delta t_i = t_i - t_{(i+1)}$ is the travel time difference between $(i + 1)$ and i th receiver, and σ_i^2 is the variance of the spectrum at i th receiver. The equation (3.23) has been applied to the windowed direct arrival event of the vertical component of VSP data. The downgoing arrivals of the receivers at different depth intervals were computed in a continuously sliding window of total depth.

3.3 Factors Affecting Attenuation Measurement

In seismic exploration most of the intrinsic attenuation estimation comes from the vertical seismic profile data. In intrinsic attenuation one of the most important factor is absorption which can affect the seismic amplitude but there are some other factors that severely affects the amplitude and shape of the signal. Most of the factors affecting attenuation measurement are related to the wave propagation, instrumental

set up, data acquisition and processing. Although it is hard to eliminate all the effects from the data set but we must be taken account for all sort of affecting factors such as geometrical spreading, transmission loss, intrabed multiple effect, interference from other signals, source receiver coupling etc. to have an accurate computation of intrinsic attenuation. Geometrical spreading of seismic energy propagating from a seismic energy source is the dominant physical process that reduces wavelet amplitude at subsurface receiver points. Geometrical spreading of spherical waves cause decrease energy density and intensity inversely as square of distance from the source (Newman, 1973). So, it is necessary to estimate this factor to get accurate intrinsic attenuation. Generally, the layered earth media complicates the estimation of attenuation coefficient (absorption) because the measurement contains not only the anelastic dissipation but also some other factors. Several works (Schoenberger and Levin, 1974, 1978) have demonstrated that the short period multiples generated in finely layered medium are very important in seismic energy transmission. The accumulative energy caused by intrabed multiples reduce the downgoing wave energy. The downgoing source pulse is superimposed on unwanted reverberations generated in the vicinity of the geophone location which produces its broadening. The effect of the intrabed multiples is similar to that due to the intrinsic attenuation (absorption). Therefore, it is very difficult to separate them. Estimation of the intrinsic attenuation enables removal of intrabed multiple's contribution from the total effective attenuation. The transmission coefficient is related to the acoustic impedance. When the acoustic impedance increases, the downgoing arrival amplitude decreases. On

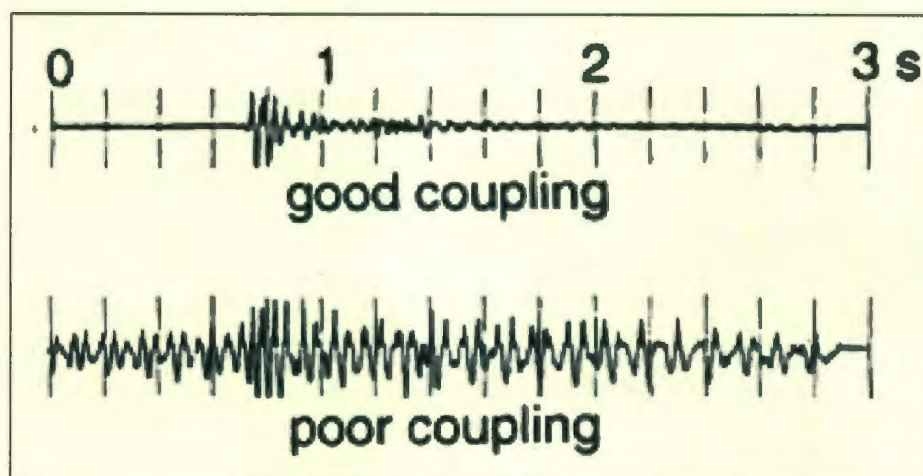


Figure 3.1: Effect of geophone-formation coupling on seismic signal (Hardage, 2000).

the contrary, if the acoustic impedance decreases the amplitude increases. Reflectors below the downhole geophone generate reflected P-wave and mode converted S-wave. Interference of these upward waves with the first arrival causes drastical changes in the shape and amplitude of the downgoing wavelet. These upgoing events can be easily identified in the VSP records, that have opposite slope sign to the downgoing first arrival. Relocating the source during data acquisition and changes in source coupling with the earth produce changes in the shape and amplitude of the source signature. If the downhole geophone coupling to the wall of the borehole is poor, the attenuation measurements are sensitively affected. In the Figure-3.1, it is illustrated the coupling effect on a seismic signal.

Chapter 4

Synthetic VSP and Attenuation Model

4.1 Introduction

The zero-offset VSP seismograms generated on simple flat layered earth models by using finite difference modeling of isotropic elastic wave equation. Simple layered models were built by a finite difference model building technique. The VSP seismograms are generated on both non-attenuative and attenuative media. All the data processing, analysis and visualization was performed by Seismic Unix (supported by the Center for Wave Phenomena, Gas Research Institute and Society of Exploration Geophysicist Foundation), a free software package developed by Colorado School of Mines. The finite difference model building, seismic modeling, advanced data analysis and attenuation computations were performed in Fortran programming environment especially Fortran 77, owing to its greater flexibility. Absorbing boundary condition was implemented at the bottom and side walls of the grid frame and a free surface was used at top of the models. The main purpose of generation of model seismograms in this study is to test and validates how the different attenuation measurement techniques works on these model seismograms.

4.2 Synthetic Earth Models

Achieving virtually identical VSP seismograms is necessary to investigate the attenuation effect on the geologic model. Several simple flat layered earth models were built and on which zero-offset VSP seismograms were generated for model base attenuation analysis. For flat layer synthetic geometric modeling of P-wave and S-wave, density and Q factor, we used finite difference numerical modeling technique. This study focused on attenuation analysis of propagating compressional wave (P-wave) through the elastic earth media. Near zero S-wave velocities have been used in all the model based studies to limit the generation of S-wave and S-wave's interference i.e. mode conversion, S-wave reflection, transmission, reverbration etc. on P-wave recording in VSP data. Seismic modeling takes one of the two forms, physical and numerical modeling. Numerical modeling involves the creation of a seismic model in computer and such models can be precisely defined with as many layers as desired.

4.2.1 Model Boundary Condition and Source Function

The artificial reflections introduced by the edges or boundaries of the computational model is one of the persistent problem in numerical simulation of propagating wave phenomenon. These reflections from the edge of the computational domain eventually propagate inward and contaminate and mask the trace solution. So it is prior important to have a better computational result in seismic modeling. In this study we applied three ways absorption boundary condition in all the layered models. The

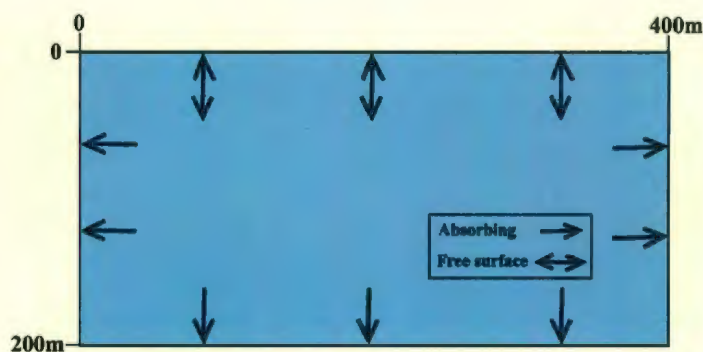


Figure 4.1: Model boundary condition. The model space is made up of unit cells in 2D space. The upper boundary is free surface and the both side walls and bottom interface having absorbing boundary condition.

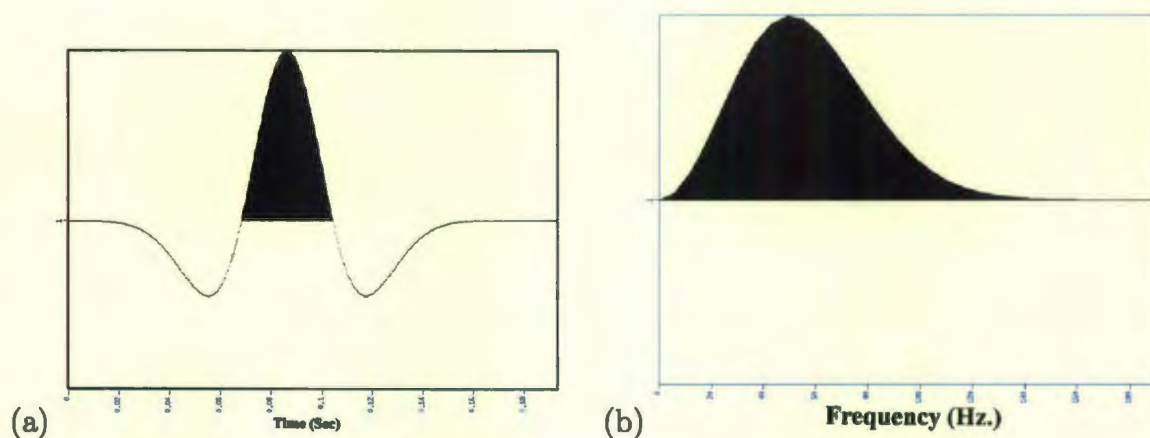


Figure 4.2: Source function, single ricker wavelet with 50Hz dominant frequency is used in seismic modeling (a) in time domain (b) in frequency domain

reflecting free surface boundary condition is imposed to the top edge of the models and the remaining boundaries i.e. both of the side walls and bottom edges are absorbing boundaries (Figure-4.1). The finite difference method used 2nd-order finite differences in time and 2nd-order in space (Appendix-A, Seismic Modeling and Finite Difference Formulation). The source signature is shown in the Figure-4.2, is a single ricker wavelet with 50Hz dominant frequency has been used in seismic model building. The computation of all of the 2D seismic models in this study typically involves

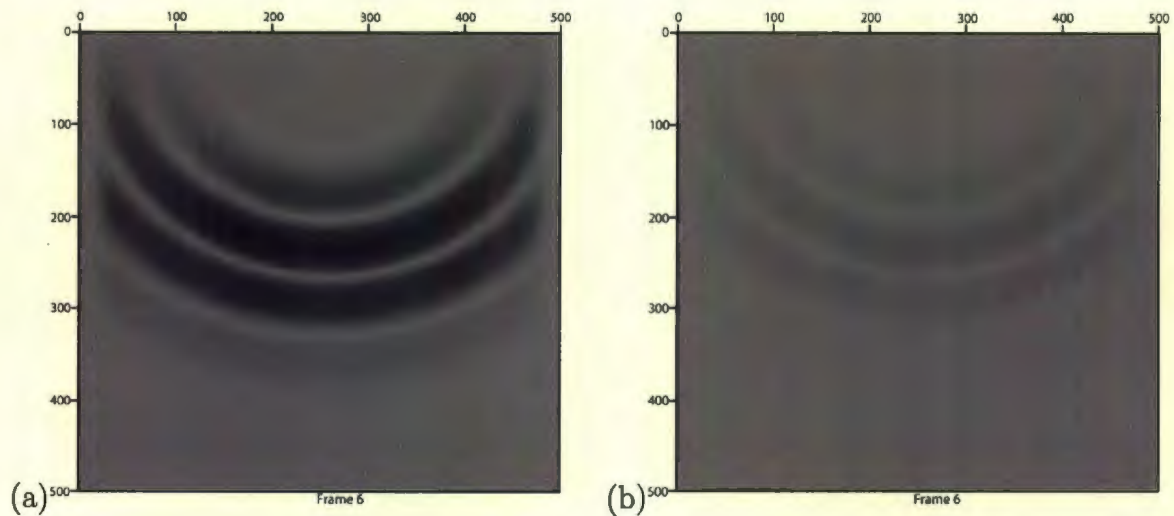


Figure 4.3: A snapshot of movie frame of wavefield within the numerical model with $V_p=3500$ m/s, $\rho=2.60$ gm/cm³ (a) non-attenuative media (b) attenuative media ($Q=5$)

the use of a point source.

4.3 Single Layered Model

We started to investigate the effect of attenuation on VSP seismograms with a simple single layered isotropic model. Using such a simple model is a good idea to understand the behavior of propagating seismic waveform (Figure-4.3). This simple model will not produce any reflected and transmitted events since it is a single homogeneous solid. The VSP seismograms are generated on this model for with attenuation and without attenuation. In both cases, models are computed with the same geometry and model parameters, i.e. length, width, velocity (V_p , V_s) density (ρ) and quality factor (Q). The source and receiver were placed as like a typical zero-offset VSP array (Figure-4.4a). The source was placed at the surface, 2m away from the center of the model and 2m below the ground. The first receiver is placed at 50m depth and the

receiver spacing is 10m.

4.4 Non Attenuative Model

The VSP seismograms for a single layer model was computed for zero-offset VSP without attenuation. Figure-4.4 and Figure-4.5, illustrated the signals in the time domain, frequency domain and logarithmic spectral ratio plot of two consecutive traces. The seismogram of this model avoid interferences of reflection, scattering, transmission or intrinsic absorption. So the decay of seismic energy or amplitude attenuation is happening only due to geometrical spreading effect. Since there is no intrinsic attenuation in this model, the linear plot of frequency-logarithmic spectral ratio has to be flat i.e. the slope of the linear plot has to be zero where the Q is ∞ .

4.5 Attenuative Model

The 2D finite difference attenuative models have been constructed for the single layered isotropic media and multi-layered models with high and low attenuative state. The reliable estimation of attenuation is much easier for a single layered isotropic model than for a multi-layered model because of its simple model configuration. Multi layering adds transmission, reflection loss, mode conversion of wave that caused loss of energy from data and noise can be added to the data from any kind of sources other than seismic sources as to record the VSP survey. So the accuracy of the attenuation estimation must be tested on different multi layered conditions by different techniques.

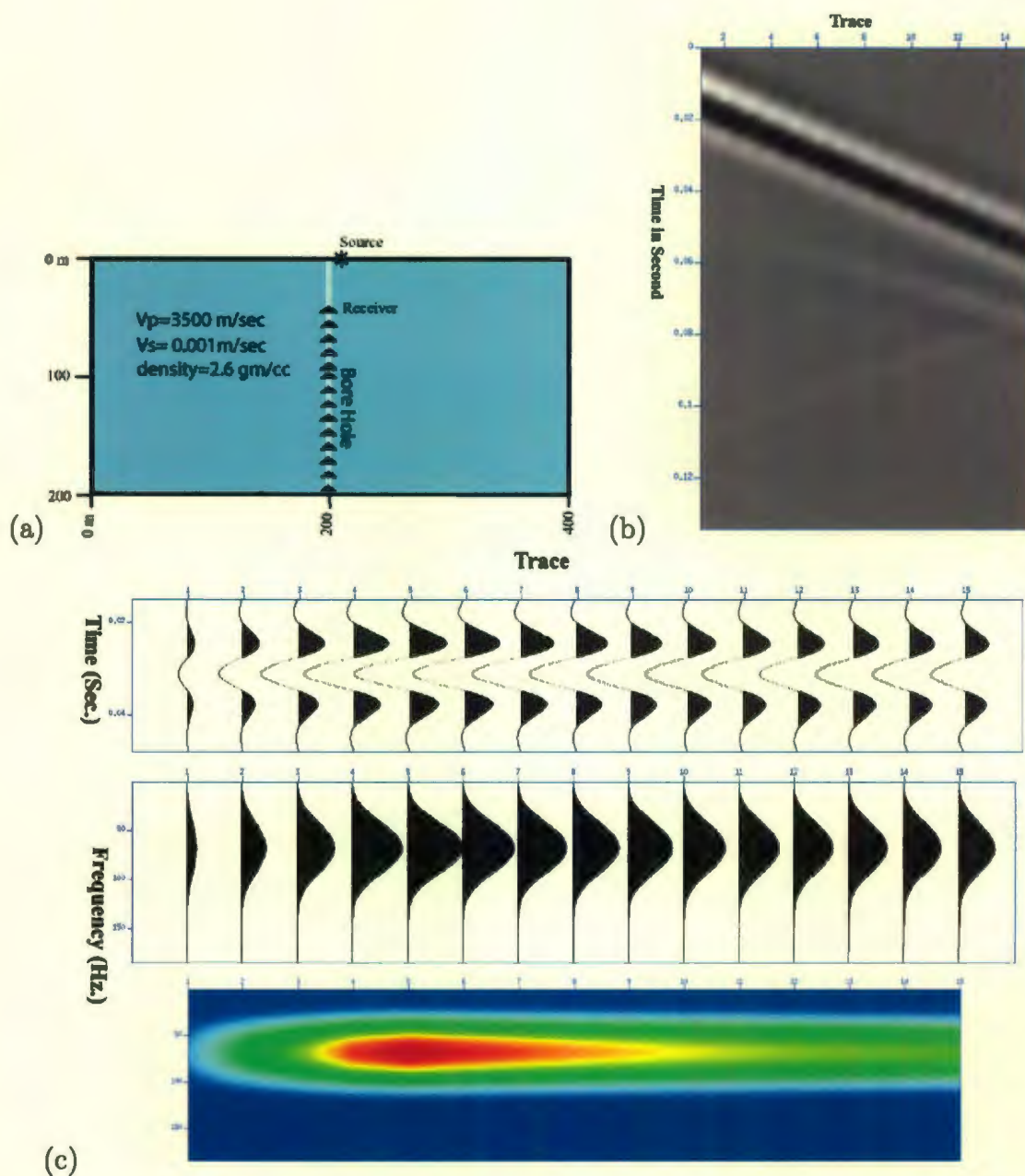


Figure 4.4: Non-attenuative model with $V_p=3500$ m/s, $\rho=2.60$ gm/cm³ (a) single layer model and VSP source receiver geometry (b) total wavefield in time domain (c) windowed downgoing direct wavefield in time and frequency domain

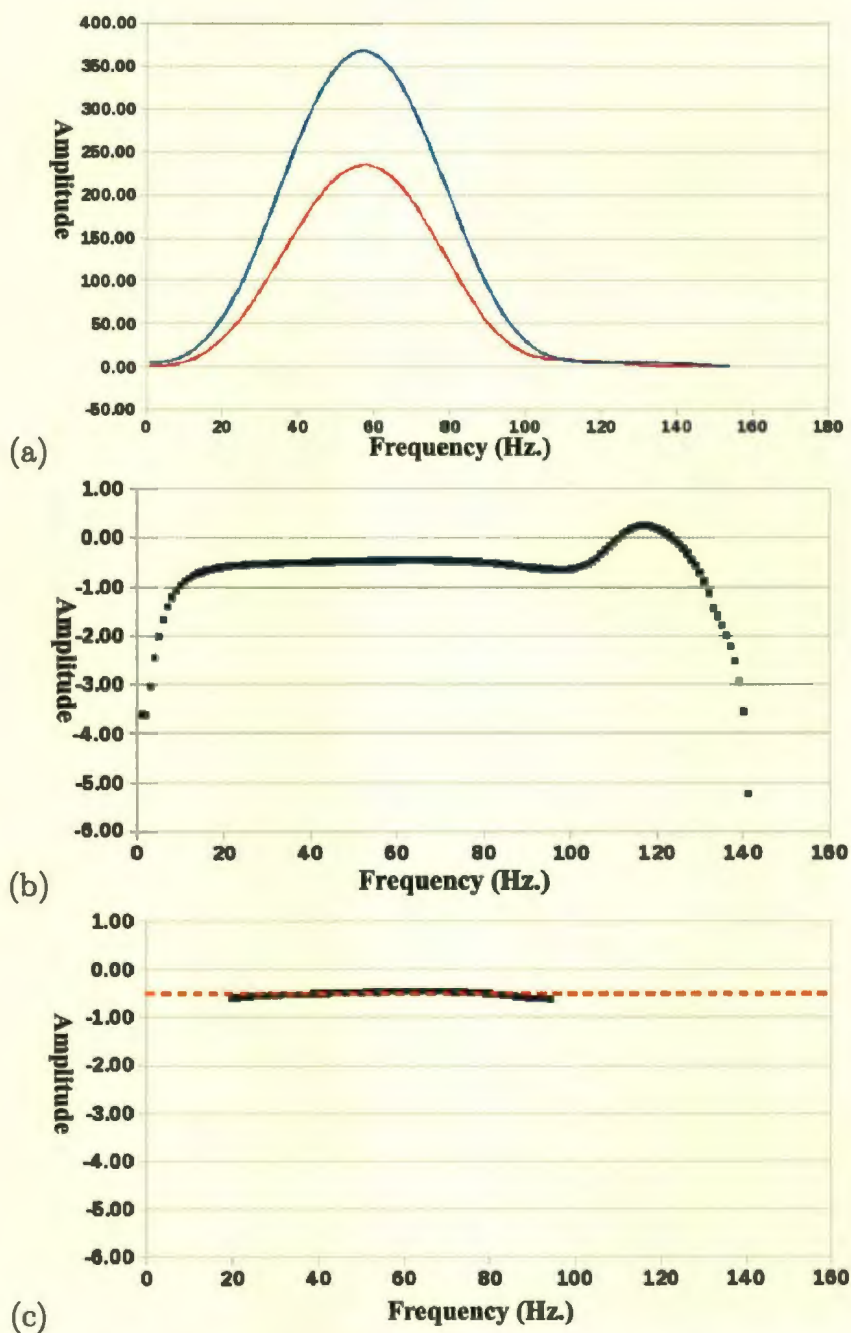


Figure 4.5: Non-attenuative model with $V_p=3500$ m/s, $\rho=2.60$ gm/cm³ (a) amplitude spectra of the traces recorded at 90m (blue) and 190m (red) depth (b) logarithmic spectral ratio of total frequency band width (c) logarithmic spectral ratio of frequency band width 20-100Hz

4.5.1 Single Layered Isotropic Model

The single layered isotropic attenuative models have been constructed with the same model parameters and geometric configuration as non-attenuative model for a low $Q(5)$ and high $Q(50)$ values shown in the Figure-4.6 and Figure-4.8. The spectral analysis of direct arrival event of those models is shown in the Figure-4.7 and Figure-4.9. The Figure-4.7a and Figure-4.9a shows the amplitude spectra in frequency domain for the traces at 90 and 190m depth levels. The logarithmic spectral ratio plot of those traces for the frequency band 0-100Hz is shown in the Figure-4.7b and Figure-4.9b. The gradient of this ratio plot for each trace pair is determined by a least-square linear-regression for Q computation by SR method. Figure-4.10 gives an illustration of centroid frequency down shift of amplitude spectra at 90 and 190m depth levels. We get the Q by using the values of the frequency down shift Δf_c and variances σ^2 mentioned in the equation (3.23).

Result of Q Computation

The amplitude spectra or energy of the seismic signal drops from 260 to 54 in the high attenuative media and 460 to 250 in the low attenuative media at depth level 90 to 190m, is shown in the Figure-4.7a and Figure-4.9a. It is also noted that seismic signals are broadened with time. The amplitude spectra in high attenuative media is relatively narrow frequency band up to 120Hz which explains that the high frequencies are more vulnerable to attenuation than the low frequencies. The estimated Q

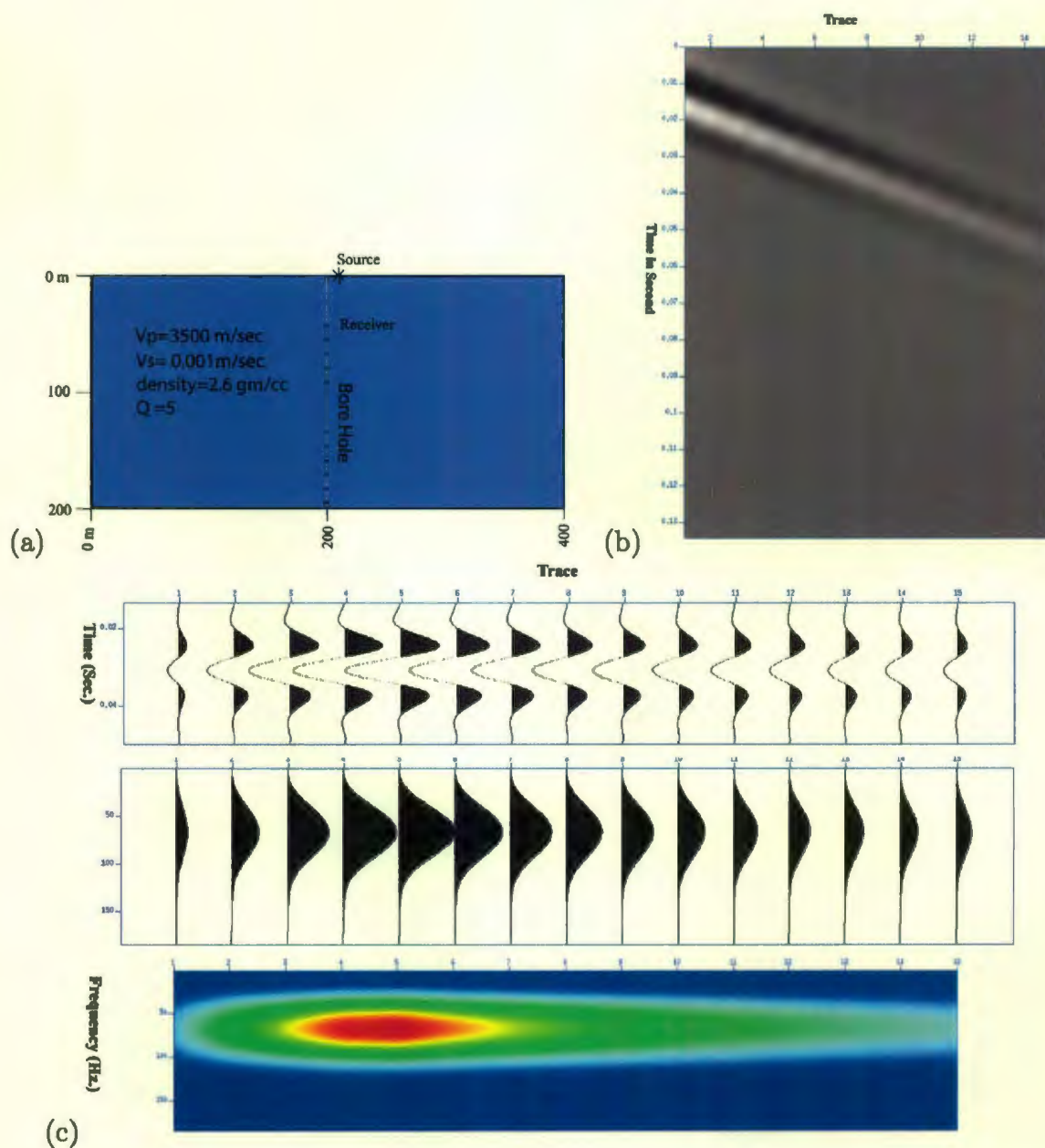


Figure 4.6: Attenuative model with $V_p = 3500$ m/s, $\rho = 2.60$ gm/cm³, $Q = 5$ (a) single layer model and VSP source receiver geometry (b) total wavefield in time domain (c) windowed downgoing direct wavefield in time and frequency domain

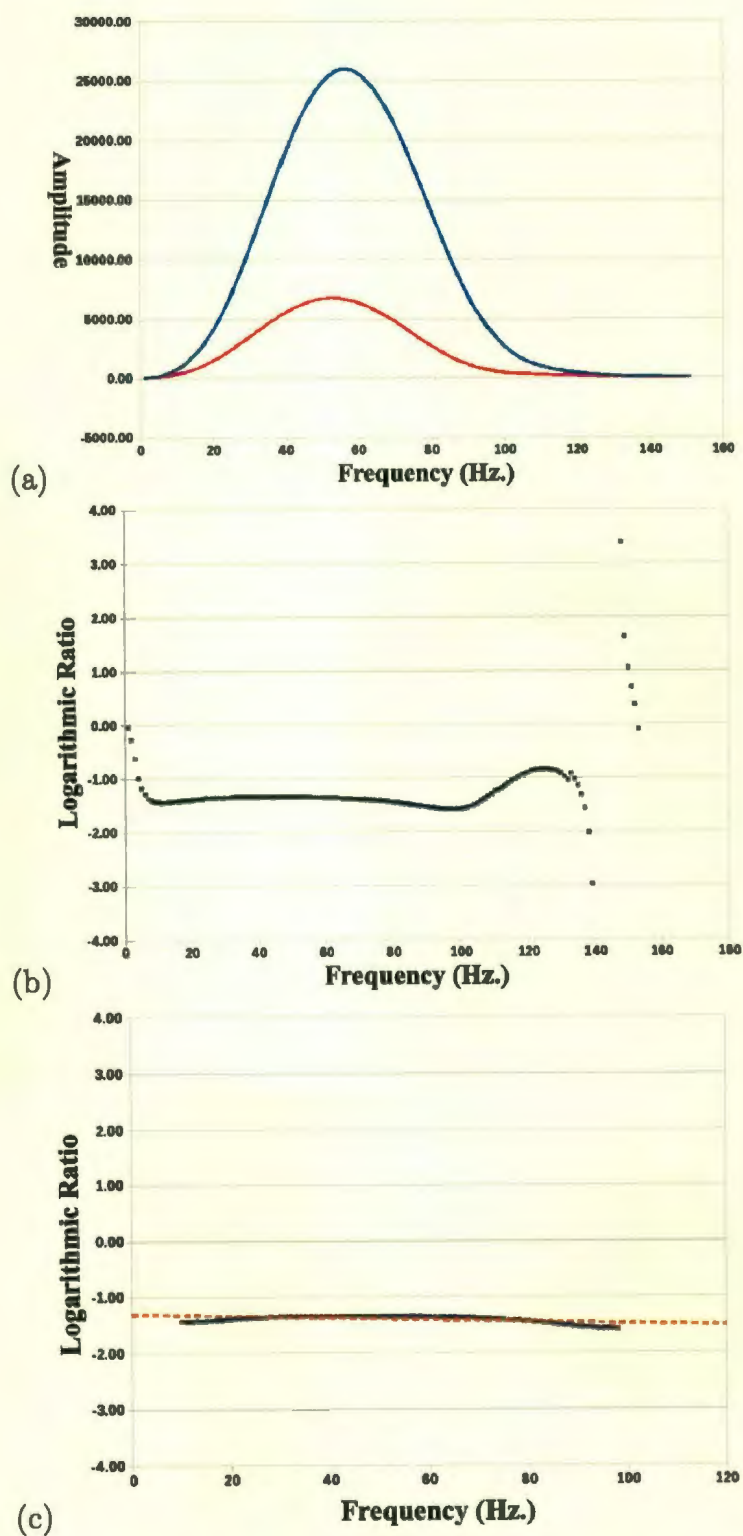


Figure 4.7: Attenuative model with $V_p=3500$ m/s, $\rho=2.60$ gm/cm³, $Q=5$ (a) amplitude spectra of the traces recorded at 90m (blue) and 190m (red) depth (b) logarithmic spectral ratio of total frequency band width (c) logarithmic spectral ratio of frequency band width 20-100Hz.

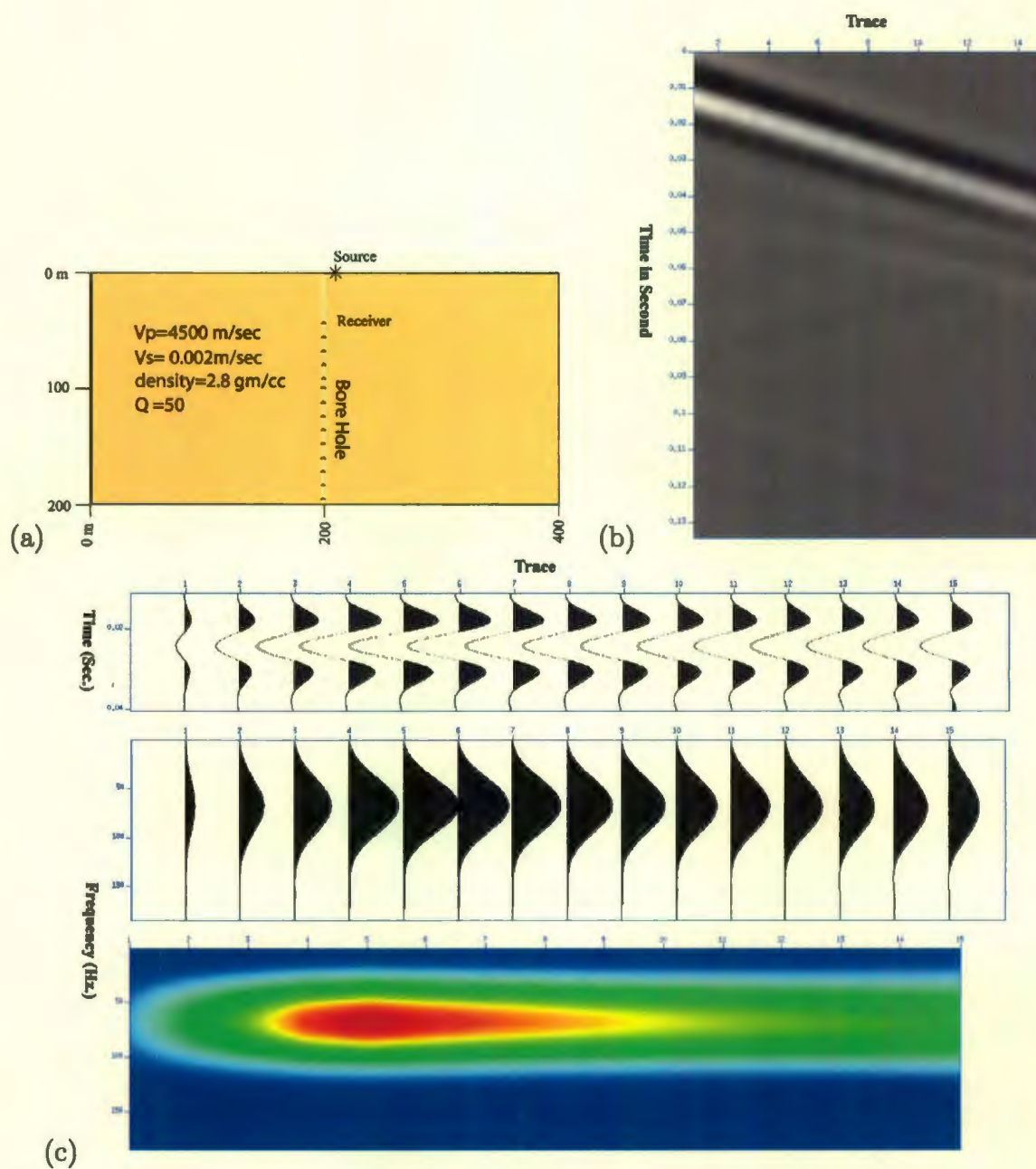


Figure 4.8: Attenuative model with $V_p = 4500$ m/s, $\rho = 2.80$ gm/cm³, $Q = 50$ (a) single layer model and VSP source receiver geometry (b) total wavefield in time domain (c) windowed downgoing direct wavefield in time and frequency domain

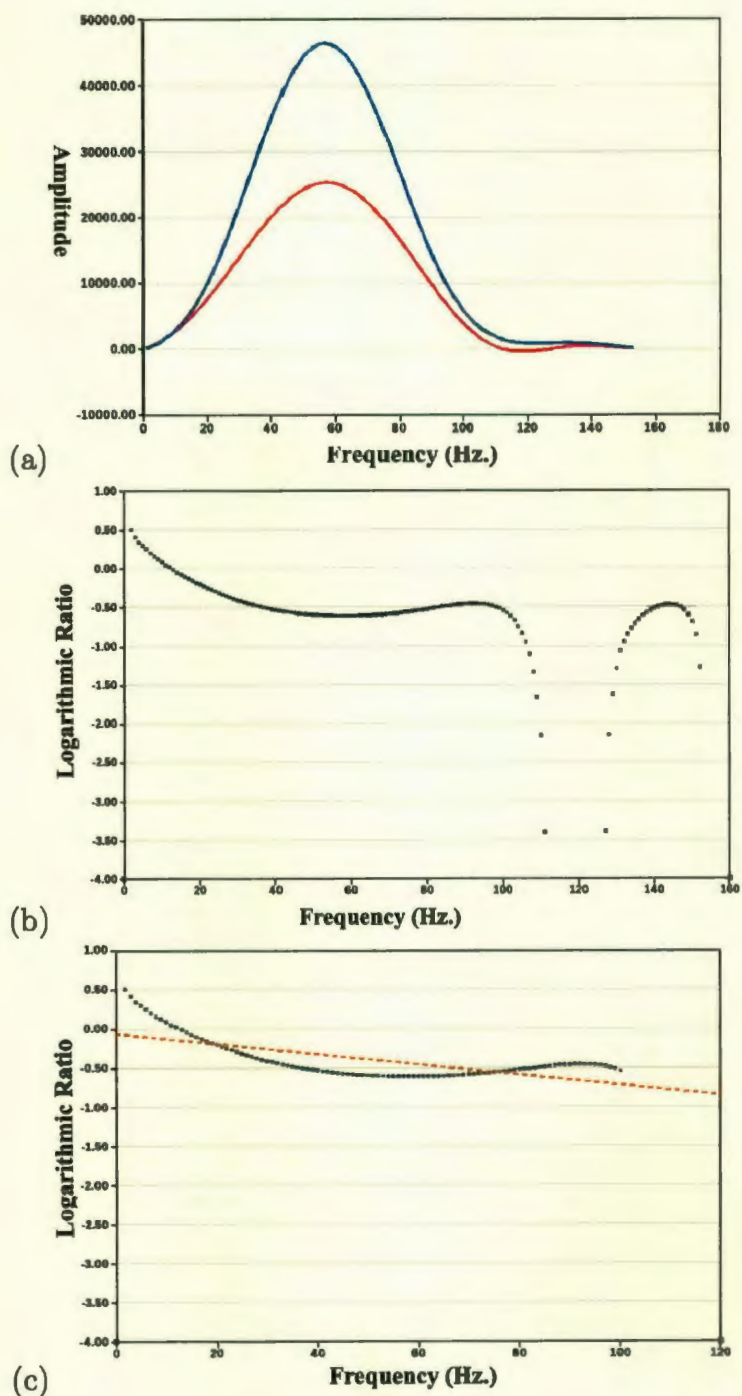


Figure 4.9: Attenuative model with $V_p=4500$ m/s, $\rho=2.80$ gm/cm³, $Q=50$ (a) amplitude spectra of the traces recorded at 90m (blue) and 190m (red) depth (b) logarithmic spectral ratio of total frequency band width (c) logarithmic spectral ratio of frequency band width 20-100Hz.

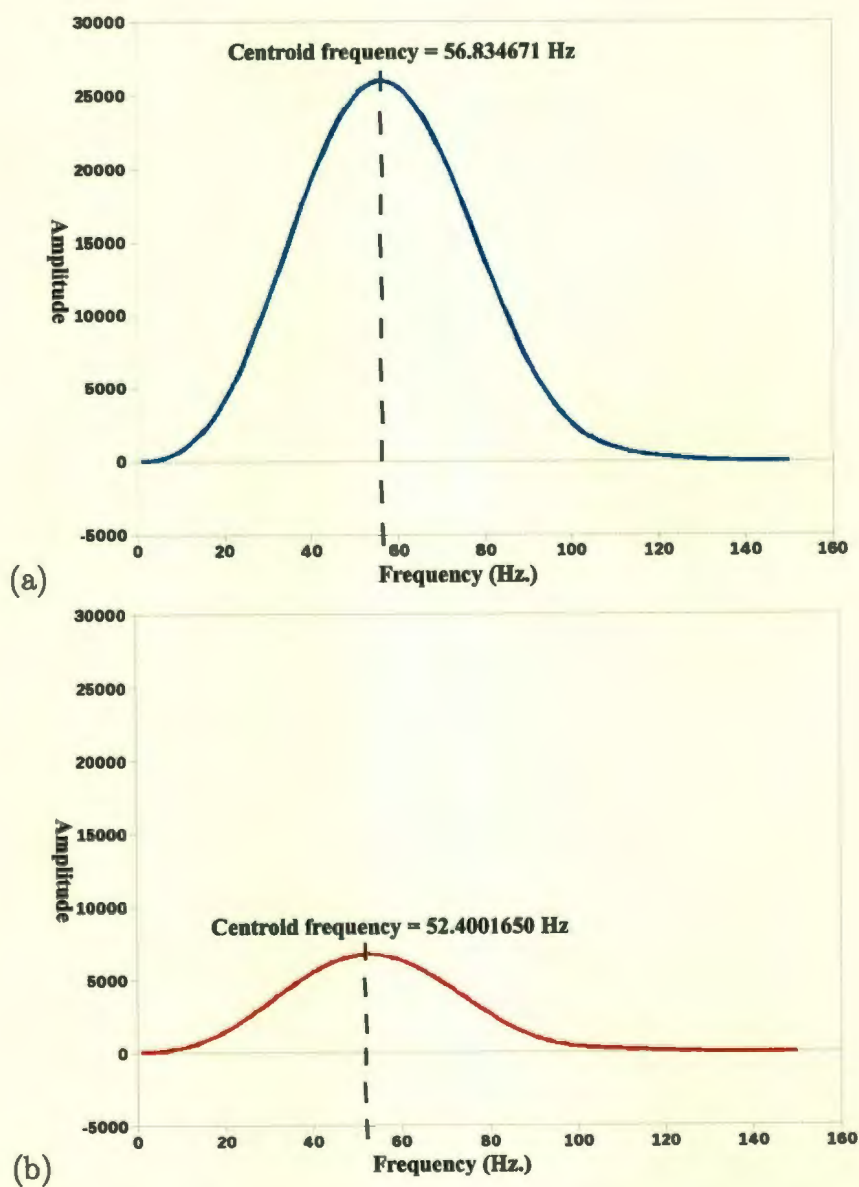


Figure 4.10: Illustration of centroid frequency shift of attenuative model with $V_p=3500$ m/s, $\rho=2.60$ gm/cm³, $Q=5$ (a) gaussian shaped amplitude spectrum of trace recorded at 90m depth where centroid frequency is 56.834671Hz (b) gaussian shaped amplitude spectrum of trace recorded at 190m depth where centroid frequency is 52.400165Hz.

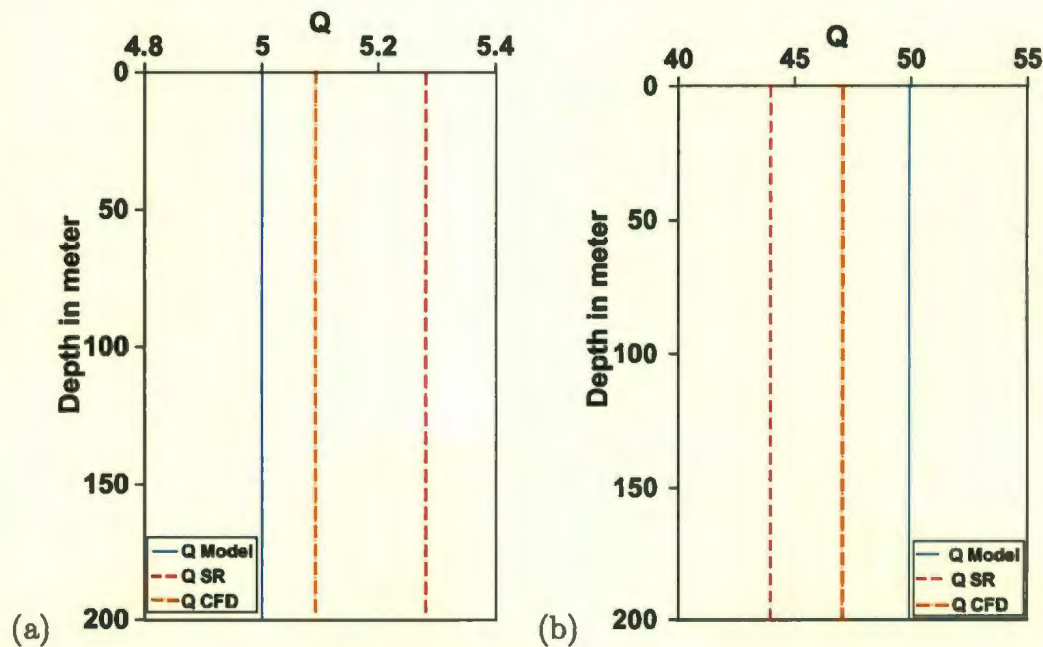


Figure 4.11: Q modeling result where shows model value (blue line) and estimated values from SR method (red line) and CFD method (orange line) (a) attenuative model with $V_p=3500$ m/s, $\rho=2.60$ gm/cm³, $Q=5$ (b) attenuative model with $V_p=4500$ m/s, $\rho=2.80$ gm/cm³, $Q=50$

by spectral ratio method for high and low attenuative media is 5.28 and 43.78 respectively. On the other hand Q estimated by centroid frequency downshift method is 5.09 and 47.32 respectively. The result of Q estimation computed by both SR and CFD method is illustrated in the Figure-4.11 with model Q values.

4.5.2 Double Layered Model

These experiments have been done for attenuation analysis of double layered model. Here we used two layered model adding another layer to the previous single layered model. This model is 400m×400m in dimension. Source was placed at the surface, 2m away from the center of the model. The first receiver placed at 50m depth and

total 35 receivers were used for VSP recording with 10m receiver spacing. The first model shown in the Figure-4.12 where the first layer is high attenuative with $V_p=3500$ m/s, $V_s=0.001$ m/s, $\rho=2.6$ gm/cm³, $Q=5$ and the second layer is low attenuative with $V_p=4500$ m/s, $V_s=0.002$ m/s, $\rho=2.8$ gm/cm³, $Q=50$. The second model shown in the Figure-4.15, where the first layer considered as low attenuative and the second layer as high attenuative media possessing the same layer properties (V_p, V_s, ρ) as the first model. The seismograms of these models are not as simple as the seismograms of the single layered model. Adding another layer to this model introduces reflection, refraction of seismic energy at the layer interface and reduces the seismic energy. Another factor that reduces the amount of energy which is mode conversion of propagating wave field. In this study we did not keep in account the wave mode conversion effect. Figure-4.13a, Figure-4.14a and Figure-4.16a, Figure-4.17a, illustrated the amplitude spectra of traces at 90, 190 and 210, 390m depth levels of both models in the frequency domain. The logarithmic spectral ratio plot of amplitude spectra of each trace pair for frequency band 0-100Hz is shown in the Figure-4.13b, Figure-4.14b and Figure-4.16b, Figure-4.17b, where the trend is linear. A linear regression technique has been used to get the best straight line of frequency-logarithmic ratio plot and compute the slope for Q estimation by spectral ratio method. The linear regression was taken over a frequency band width 0-100Hz and the Q has been calculated layer by layer. Centroid frequency estimation of the spectra has been done over the amplitude spectra for all of the traces keep in account for Q computation. Centroid frequency down shift of amplitude spectra of seismograms have been calculated as described in

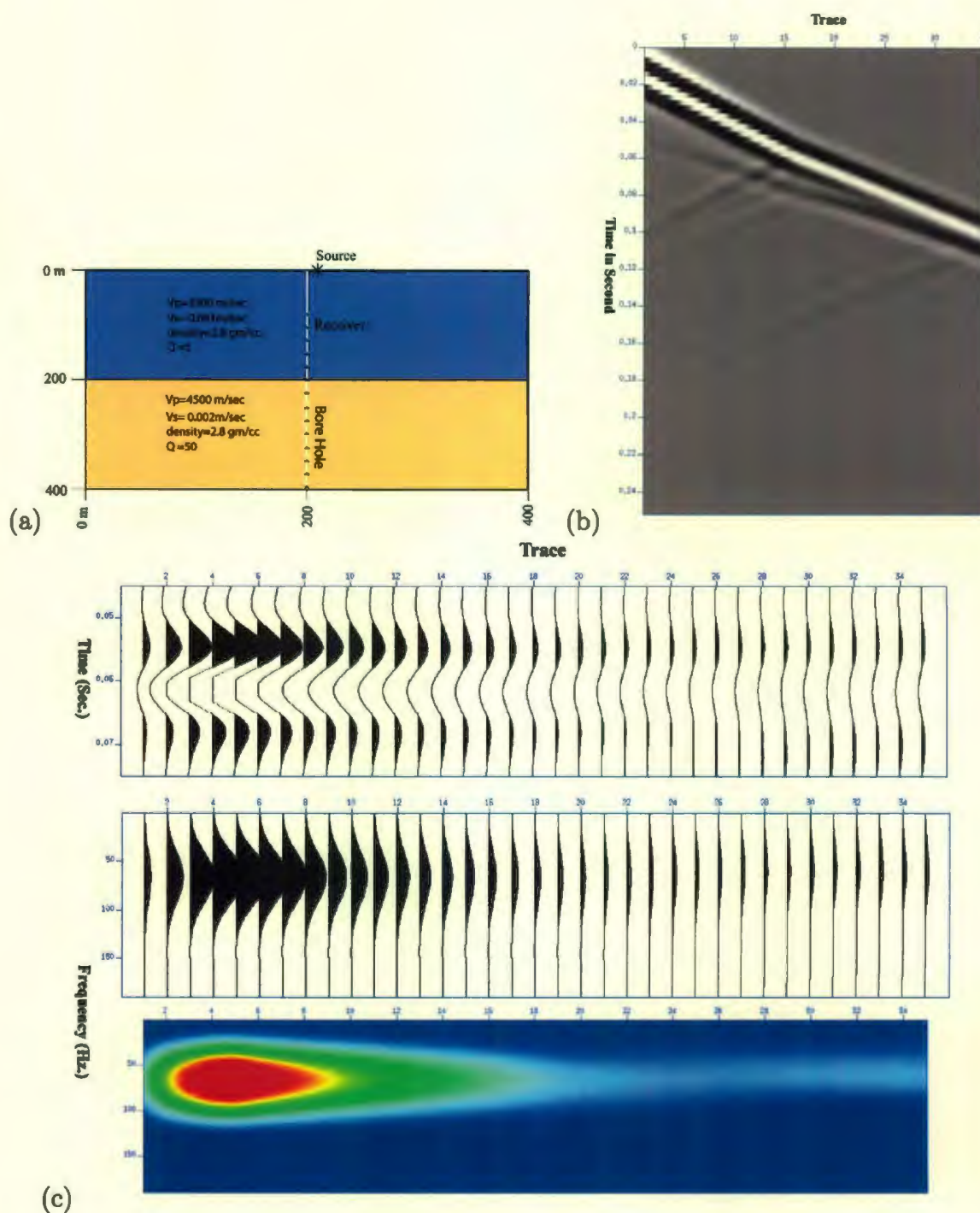


Figure 4.12: Double layered attenuative model with first layer: $V_p=3500$ m/s, $\rho=2.60$ gm/cm³, $Q=5$, and second layer: $V_p=4500$ m/s, $\rho=2.80$ gm/cm³, $Q=50$ (a) layer model and VSP source receiver geometry (b) total wavefield in time domain (c) windowed downgoing direct wavefield in time and frequency domain

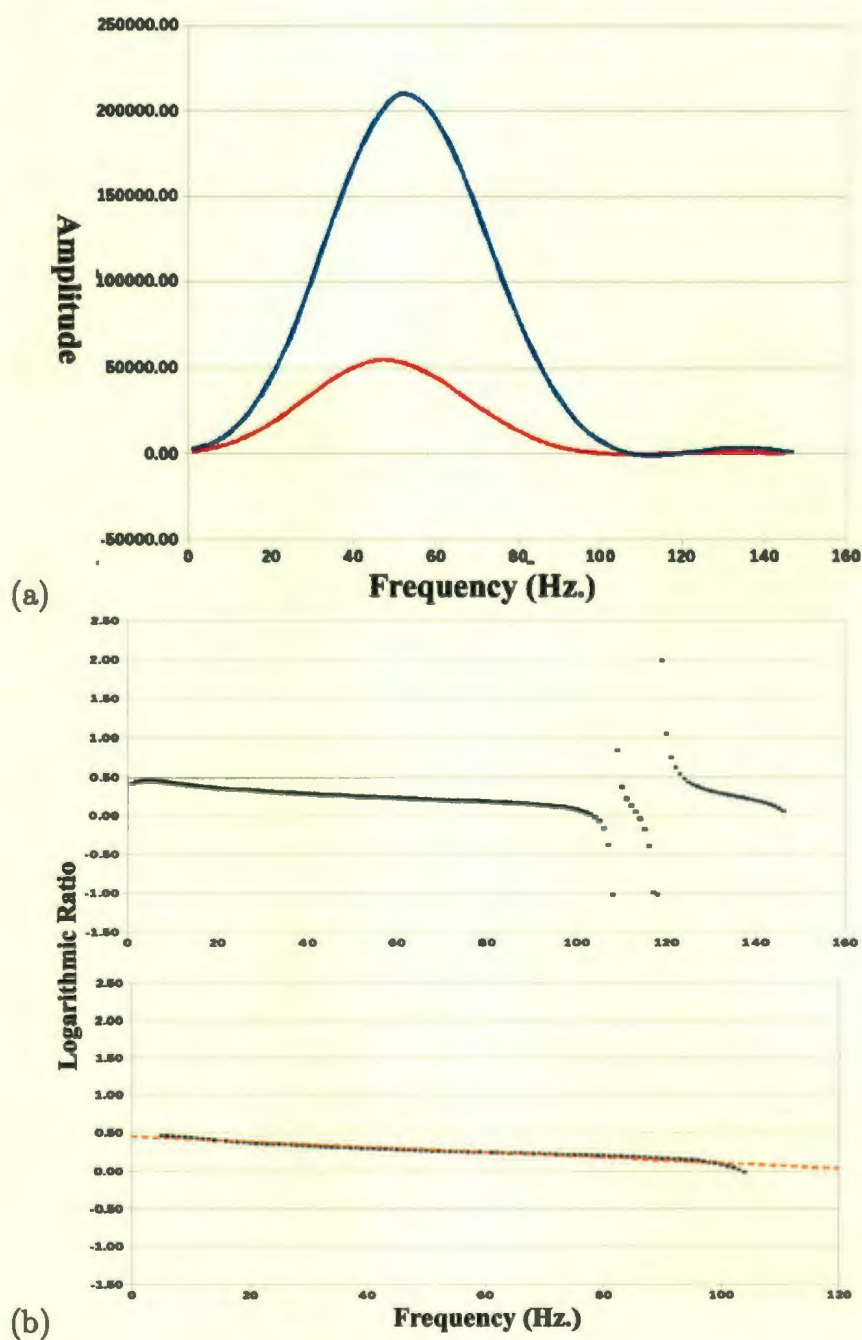


Figure 4.13: Double layer attenuative model is shown in the Figure-4.12 (a) amplitude spectra of the traces recorded at 90m (blue) and 190m (red) depth (b) top: logarithmic spectral ratio of total frequency band width, bottom: logarithmic spectral ratio of frequency band width 5-105Hz

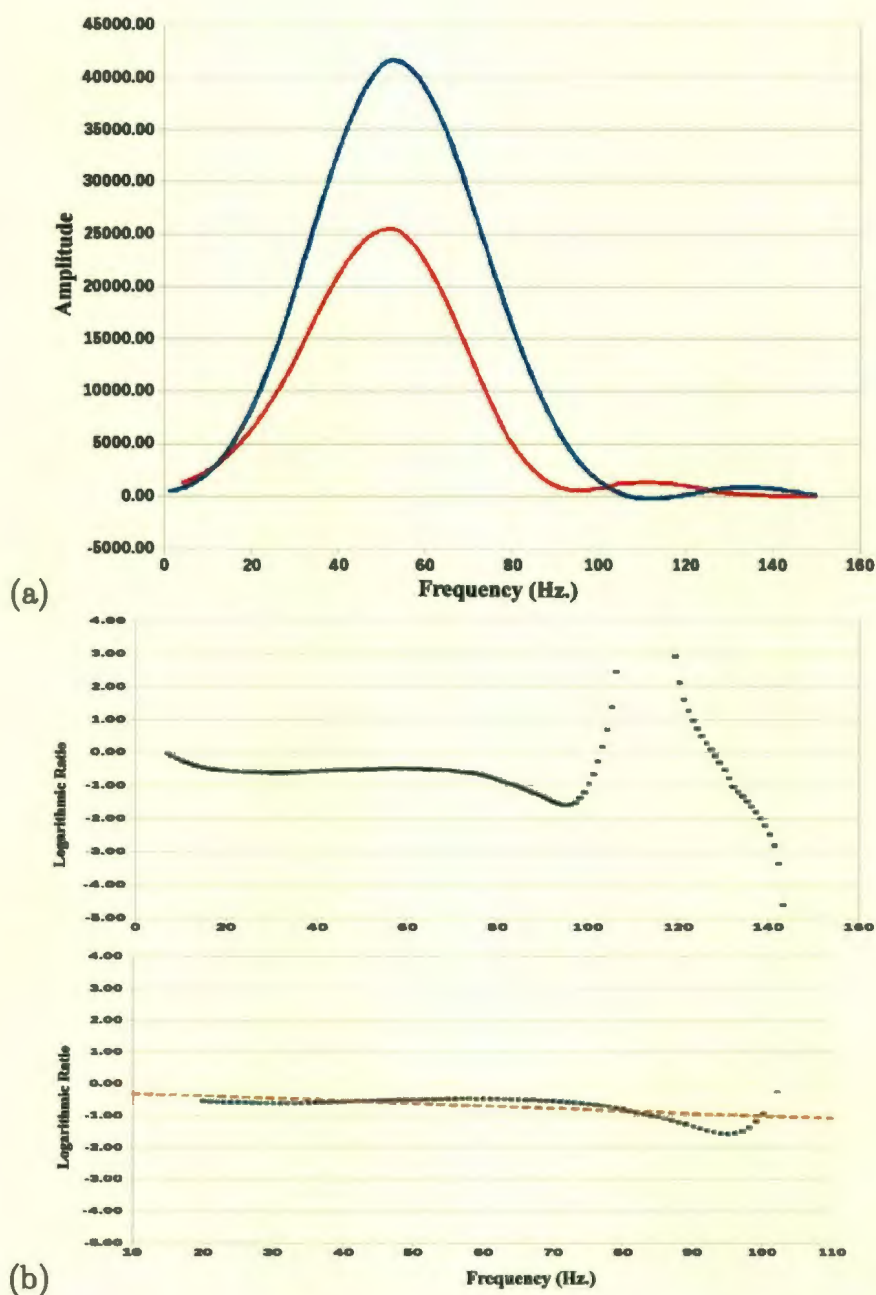


Figure 4.14: Double layer attenuative model is shown in the Figure-4.12 (a) amplitude spectra of the traces recorded at 210m (blue) and 390m (red) depth (b) top: logarithmic spectral ratio of total frequency band width, bottom: logarithmic spectral ratio of frequency band width 20-100Hz

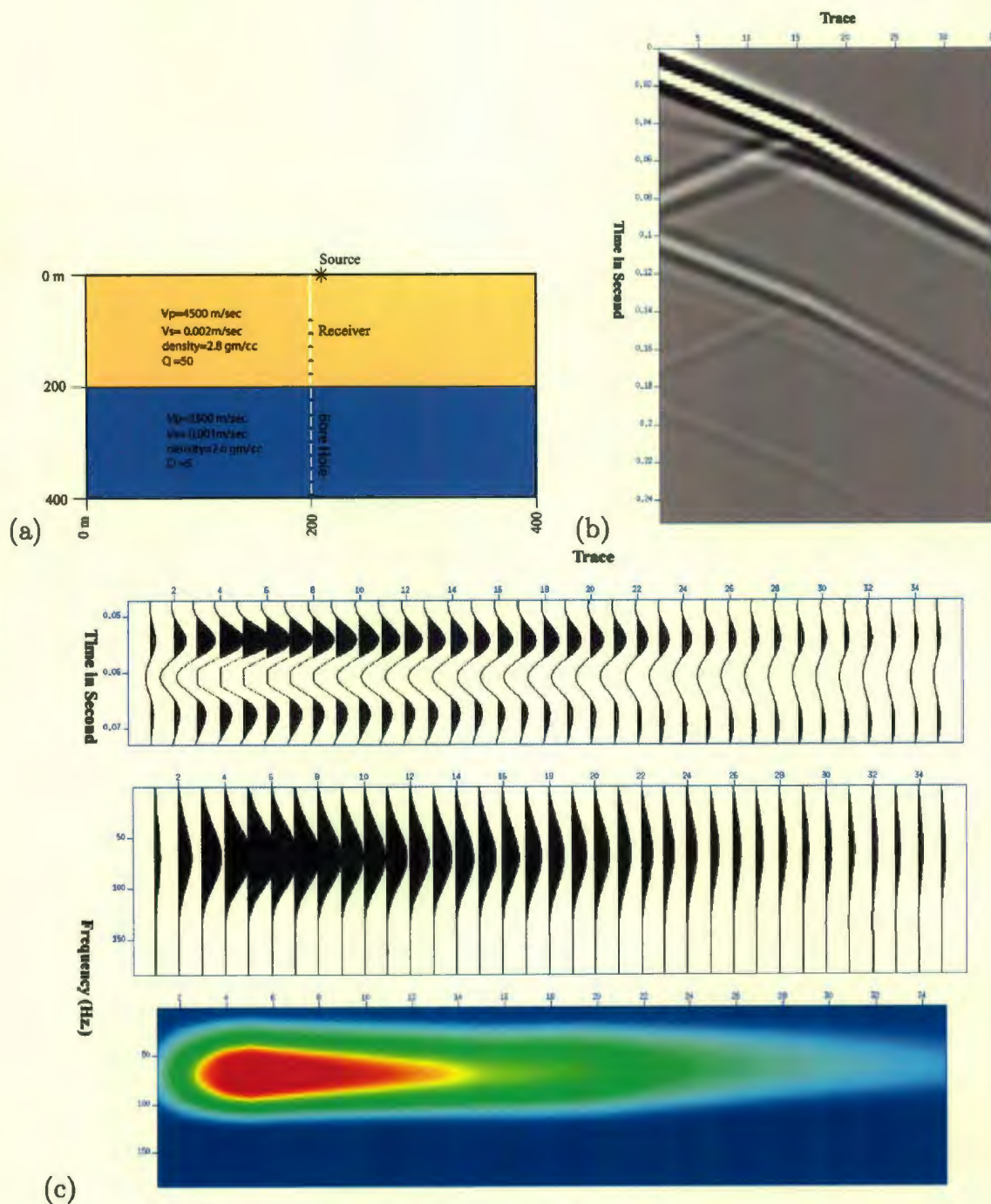


Figure 4.15: Double layered attenuative model with first layer: $V_p=4500$ m/s, $\rho=2.80$ gm/cm³, $Q=50$, and second layer: $V_p=3500$ m/s, $\rho=2.60$ gm/cm³, $Q=5$ (a) layer model and VSP source receiver geometry (b) total wavefield in time domain (c) windowed downgoing direct wavefield in time and frequency domain

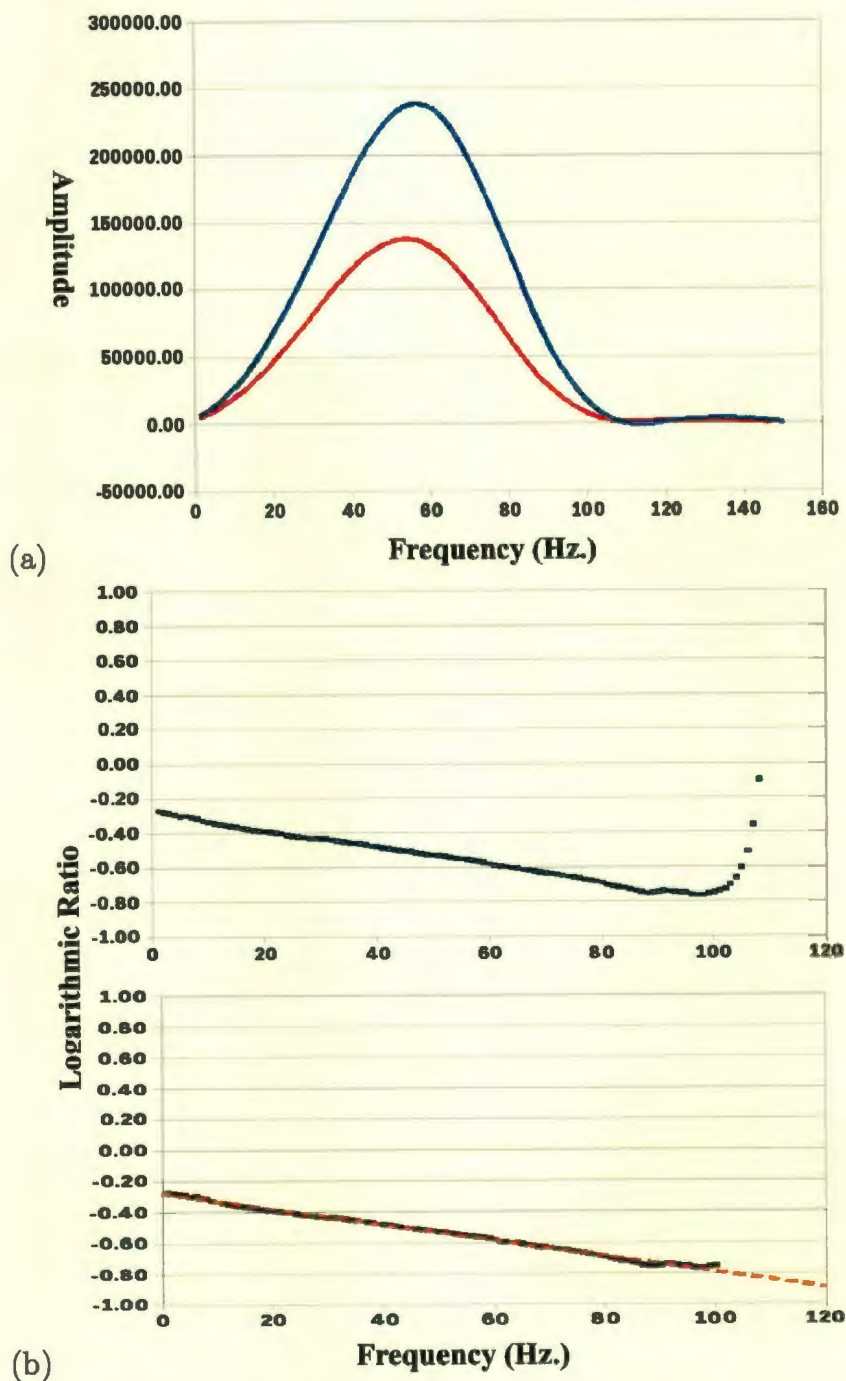


Figure 4.16: Double layer attenuative model is shown in the Figure-4.15 (a) amplitude spectra of the traces recorded at 90m (blue) and 190m (red) depth (b) top: logarithmic spectral ratio of total frequency band width, bottom: logarithmic spectral ratio of frequency band width 0-100Hz.

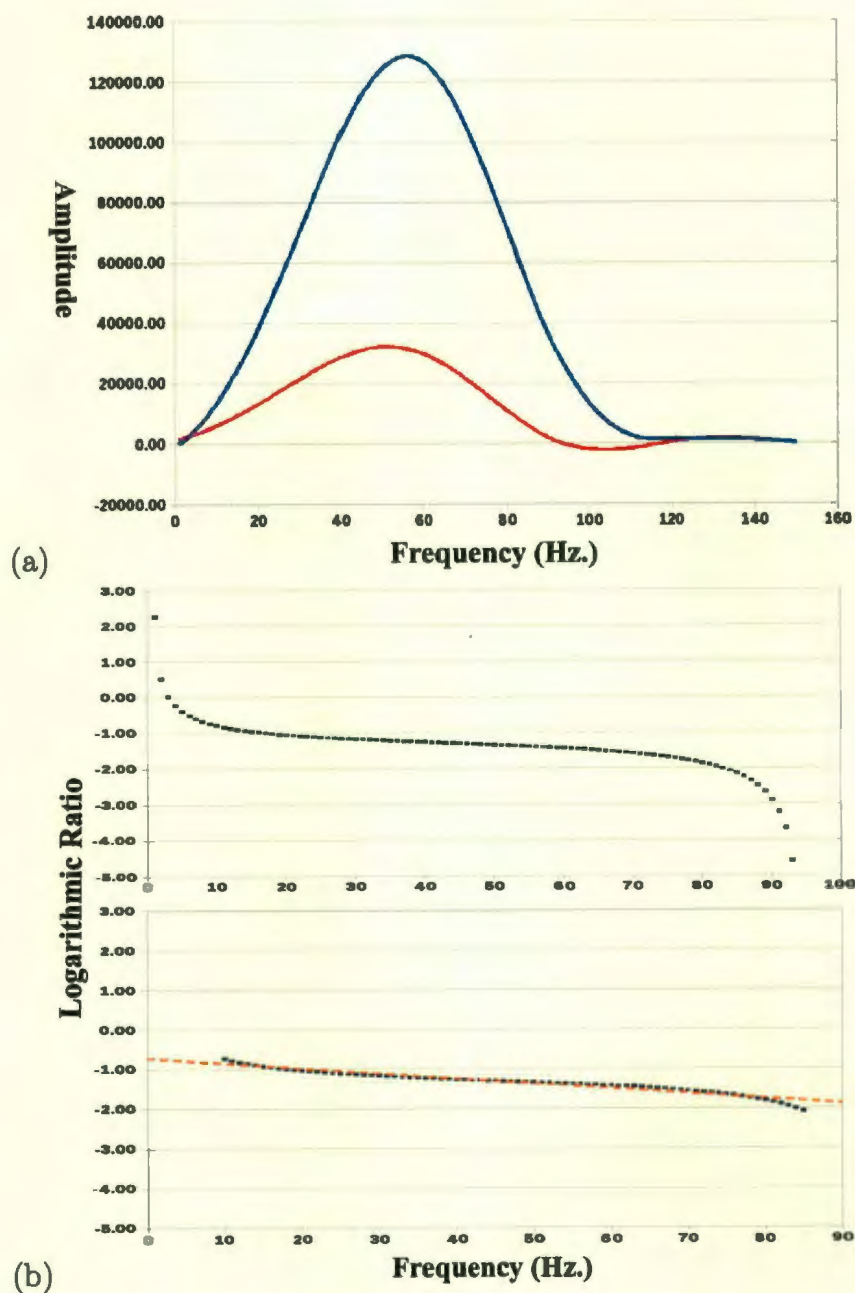


Figure 4.17: Double layer attenuative model is shown in the Figure-4.15 (a) amplitude spectra of the traces recorded at 210m (blue) and 390m (red) depth (b) top: logarithmic spectral ratio of total frequency band width, bottom: logarithmic spectral ratio of frequency band width 10-85Hz.

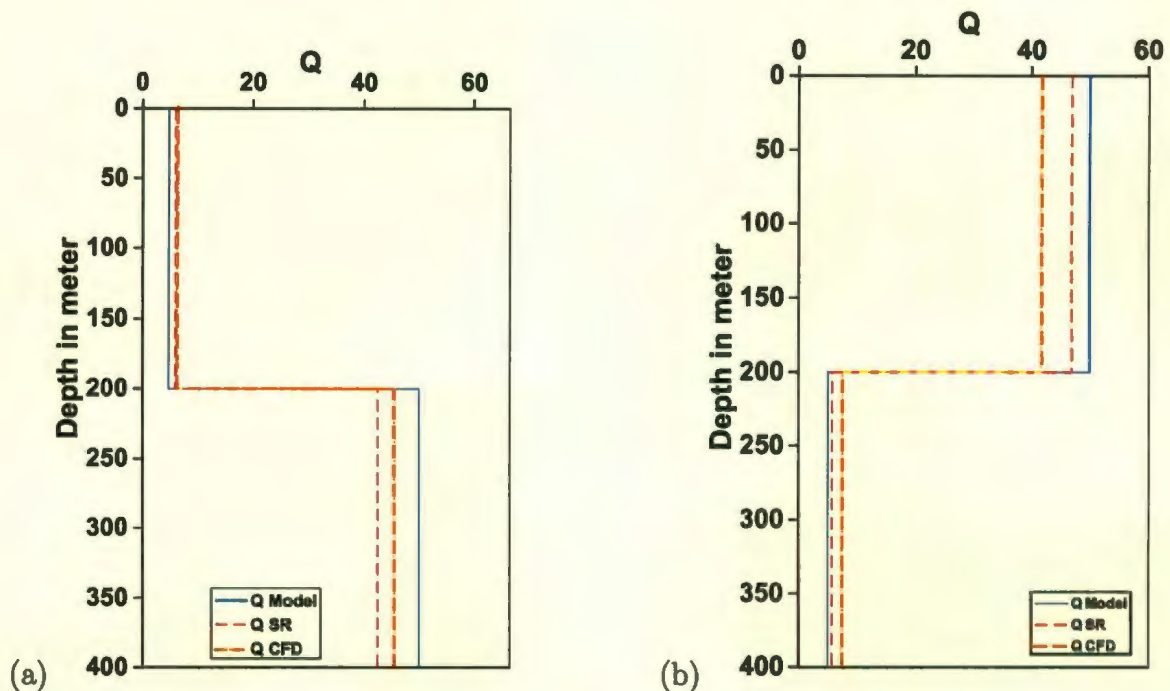


Figure 4.18: Q modeling result where shows model value (blue line) and estimated values from SR method (red line) and CFD method (orange line) (a) double layered attenuative model shown in the Figure-4.12a (b) double layered attenuative model shown in the Figure-4.15a

the Figure-4.10. The frequency downshift Δf_c and variance σ^2 substitute in equation (3.23) for Q calculation.

Result of Q Computation

Figure-4.13, Figure-4.14 and Figure-4.16, Figure-4.17, shows amplitude spectra and logarithmic ratio of the processed traces at depth 90, 190, 210, and 390m depth levels in both high and low attenuative models. The reduction in peak amplitude level and changing the nature of wavelet become broader and more asymmetric with depth which is expected behavior in the attenuative media. The best straight line of logarithmic spectral ratio (A_{n+1}/A_n) versus frequency plot of these seismograms

is indicated by dash line. The quality factor, Q has been calculated as 5.93 and 42.6 for first model (Figure-4.12a) and 46.88 and 5.83 for second model (Figure-4.15a) by using SR method. On the other hand Q estimated by centroid frequency downshift method is 6.23 and 45.40 for first model and 41.82 and 7.65 for the second model. The result of Q estimation computed by both SR and CFD method is illustrated in the Figure-4.18 with model Q values.

4.5.3 Three Layered Model

Three layered model experiment has been conducted to study the effect of high attenuative media within the low attenuative media and vice versa. These models have been constructed by using the same model geometric configuration with adding an additional layer of 200m in thickness to the double layered model. These models are 400m×600m in dimension with 200m layer thickness. The source position is on the surface and 2m away from the center of the model. The first receiver position is at 50m depth level and total 55 receivers were used for VSP recoding with 10m receiver spacing. The first model is shown in the Figure-4.19, where the low attenuative layer is sandwiched in between high attenuative layers. The layer parameters of the high and low attenuative layers is considered as $V_p=3500$ m/s, $V_s=0.001$ m/s, $\rho=2.6$ gm/cm³, $Q=5$ and $V_p=4500$ m/s, $V_s=0.002$ m/s, $\rho=2.8$ gm/cm³, $Q=50$ respectively. As mentioned in the previous section the multi layered model produces reflection, refraction and transmission and mode conversion of propagating wave that caused the amplitude reduction in the seismic signals. Moreover, the multi layering introduced different order

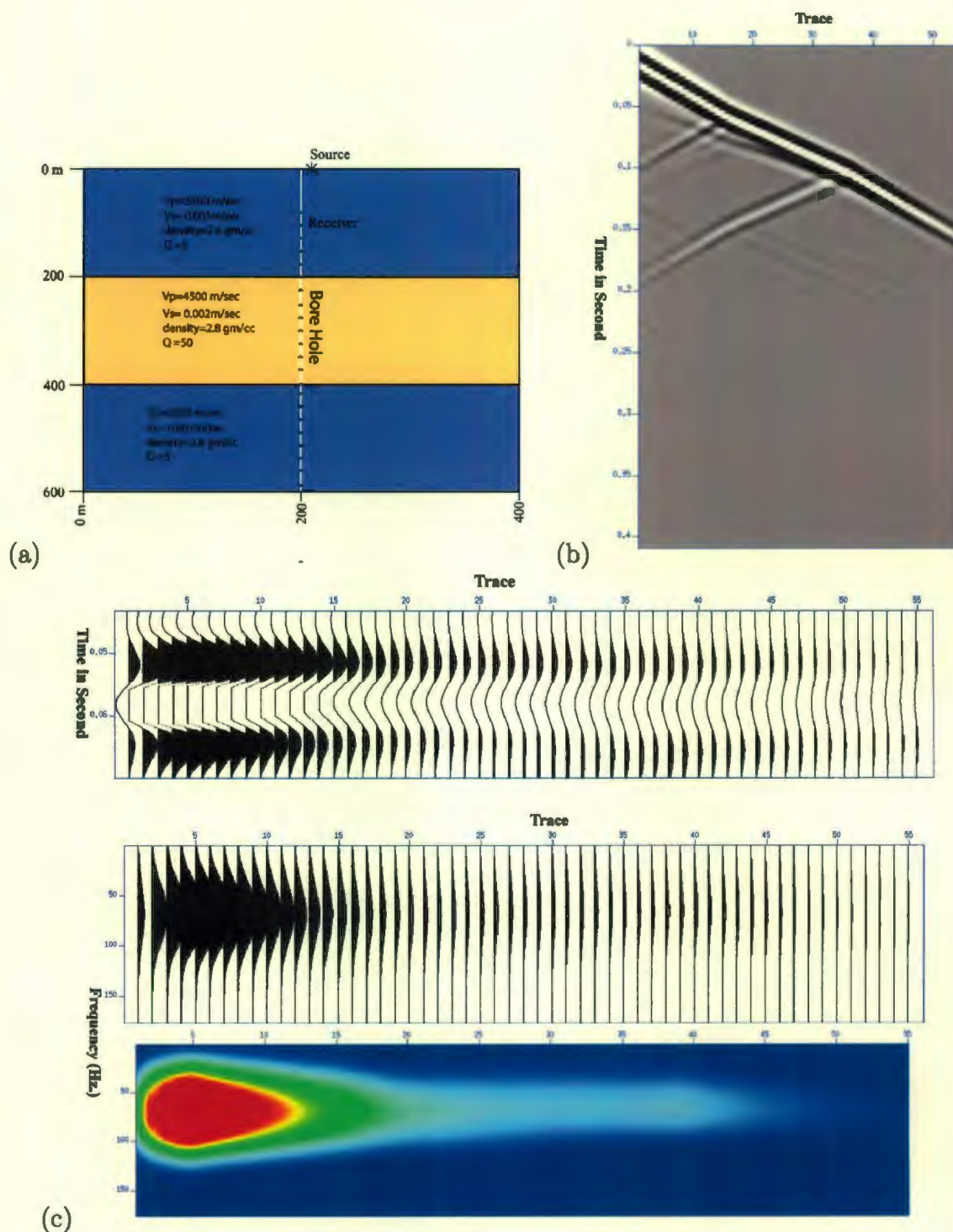


Figure 4.19: Three layer attenuative model with first layer: $V_p=3500$ m/s, $\rho=2.60$ gm/cm³, $Q=5$, second layer: $V_p=4500$ m/s, $\rho=2.80$ gm/cm³, $Q=50$, and third layer: $V_p=3500$ m/s, $\rho=2.60$ gm/cm³, $Q=5$ (a) layer model and VSP source receiver geometry (b) total wavefield in time domain (c) windowed downgoing direct wavefield in time and frequency domain.

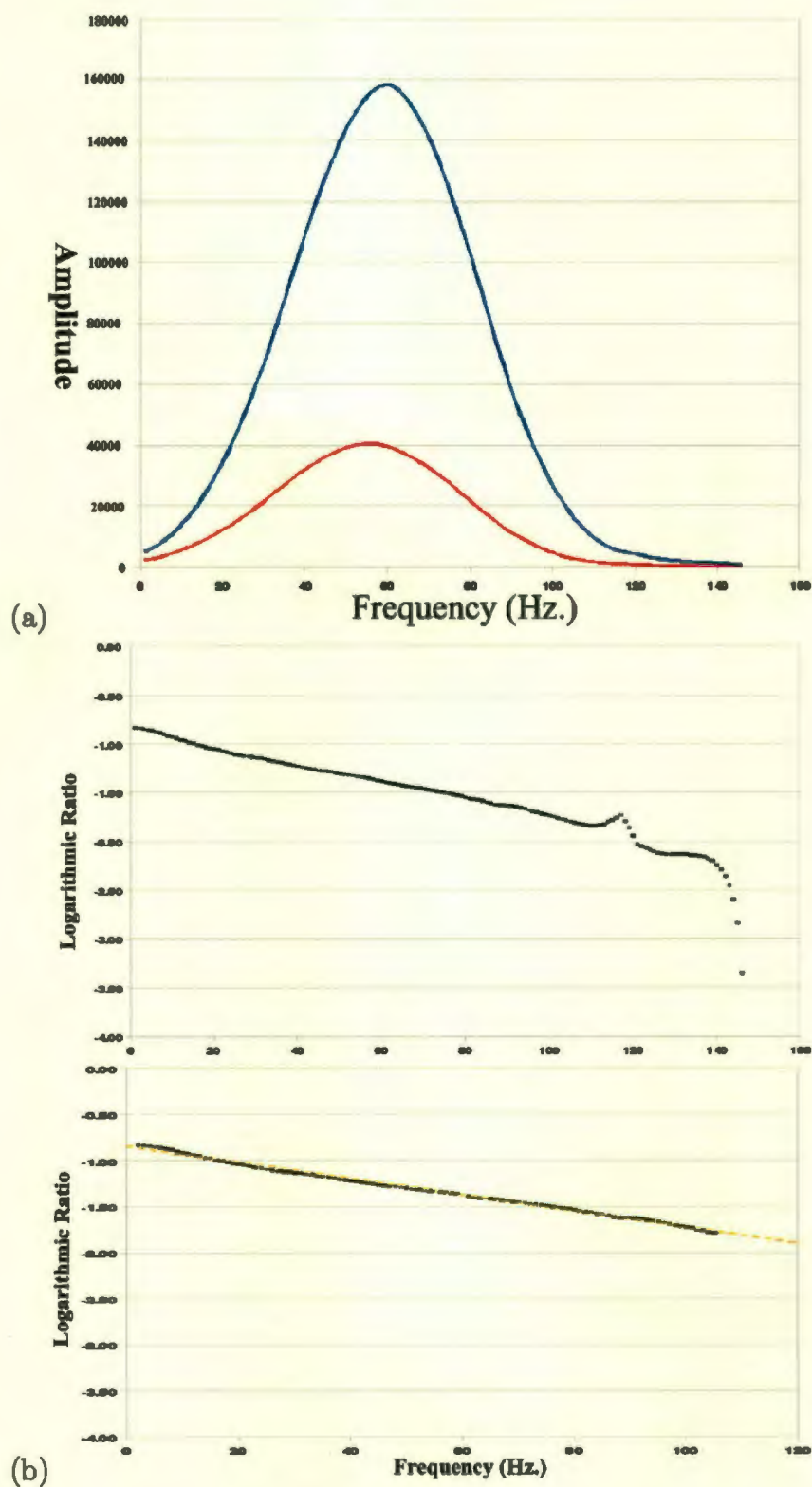


Figure 4.20: Amplitude and spectral ratio of the three layered attenuative model shown in Figure-4.19 (a) amplitude spectra of the traces recorded at 90m (blue) and 190m (red) depth (b) top: logarithmic spectral ratio of total frequency band width, bottom: logarithmic spectral ratio of frequency band width 0-110Hz

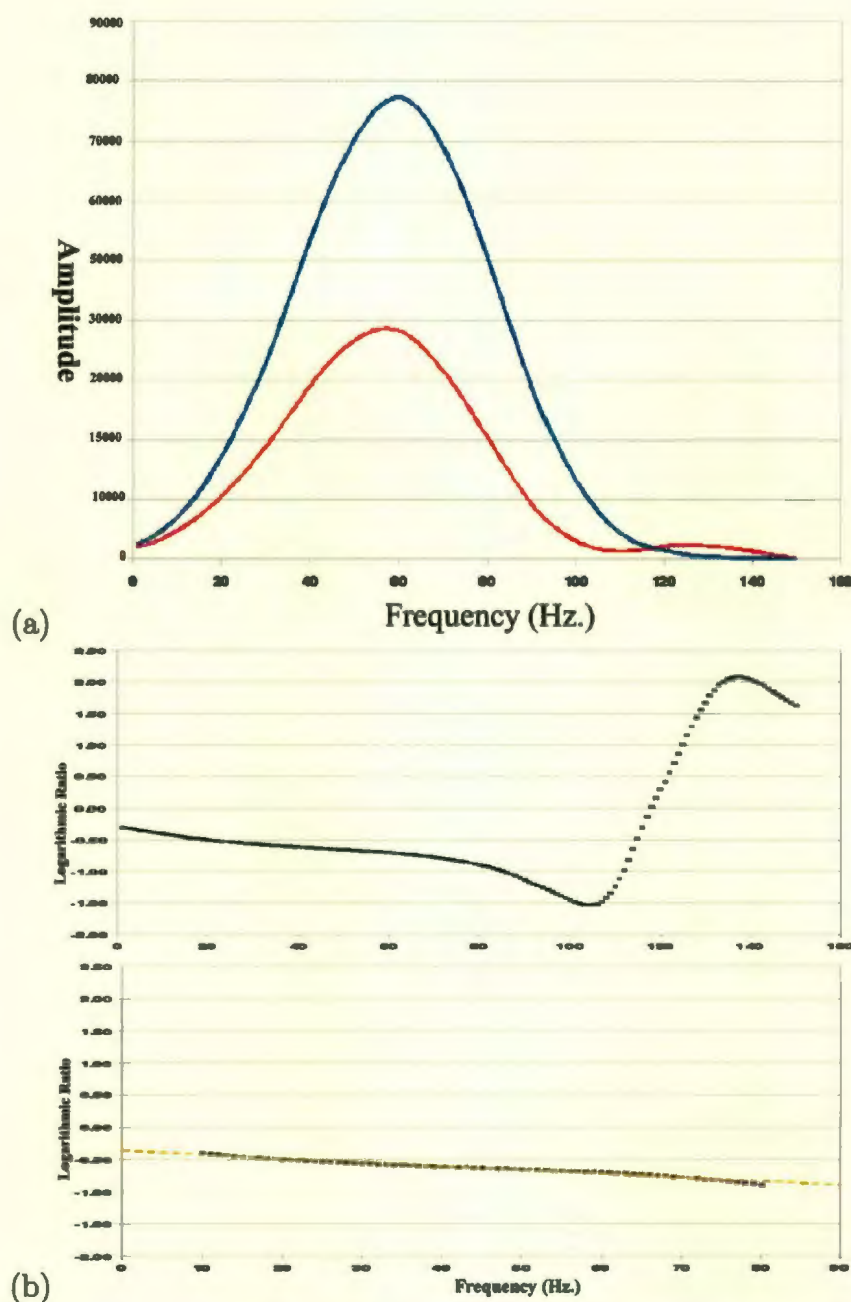


Figure 4.21: Amplitude and spectral ratio of the three layered attenuative model shown in Figure-4.19 (a) amplitude spectra of the traces recorded at 210m (blue) and 390m (red) depth (b) top: logarithmic spectral ratio of total frequency band width, bottom: logarithmic spectral ratio of frequency band width 10-100Hz

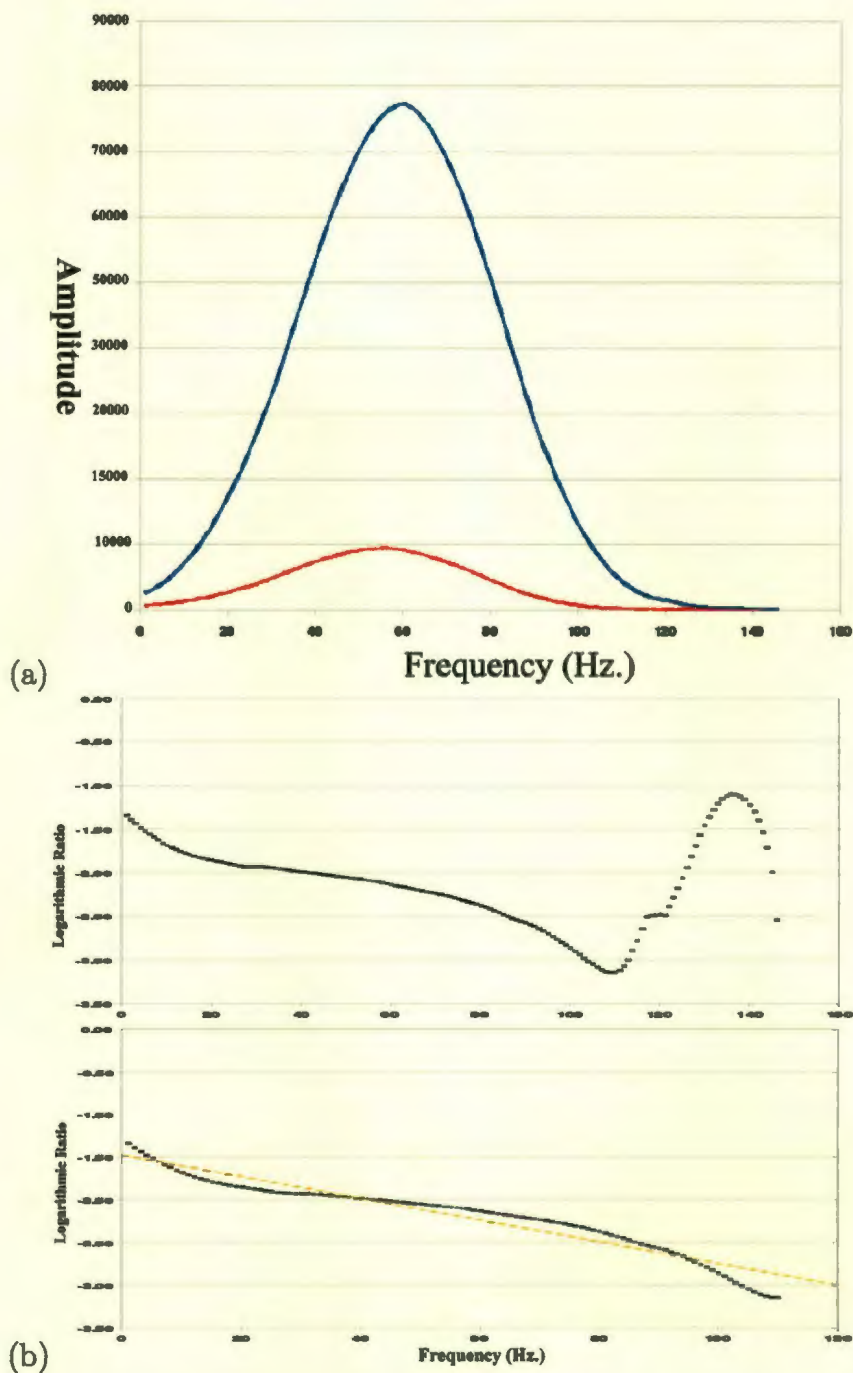


Figure 4.22: Amplitude and spectral ratio of the three layered attenuative model shown in Figure-4.19 (a) amplitude spectra of the traces recorded at 410m (blue) and 590m (red) depth (b) top: logarithmic spectral ratio of total frequency band width, bottom: logarithmic spectral ratio of frequency band width 0-110Hz

of multiples in the seismogram by trapping the reflected energy in between top and bottom interface of the layer. So the multi layered model synthetic seismograms have noise content which is one of the main constrain in reliable attenuation estimation. In this study we used a 7 point median filter and 0,1-100,150Hz bandpass filter to separate downgoing event and removing the subsequent noise content from the seismograms. The Figure-4.20 to Figure-4.22, and Figure-4.24 to Figure-4.26, illustrated the amplitude spectra and logarithmic spectral ratio of traces at 90, 190 and 210, 390 and 410, 590m depth levels of both models. The linear regression was taken over a frequency band width 0-100Hz and the Q has been calculated layer by layer. Centroid frequency estimation of the spectra has been done over the amplitude spectra for all of these traces keep in account for Q computation. The frequency downshift Δf_c and variance σ^2 has substituted in the equation (3.23) for Q calculation.

Result of Q computation

Figure-4.20 to Figure-4.22 and Figure-4.24 to Figure-4.26, shows amplitude spectra and logarithmic ratio of the processed traces at depth 90, 190, 210, 390, 410 and 590m depth levels in both high and low attenuative models. In the first model (Figure-4.19) reduction in peak amplitude level is high and changing the nature of wavelet for first and bottom layer is similar. The reduction in peak amplitude level the middle layer is low and changing the nature of wavelet become broader and more asymmetric. In the second model (Figure-4.23) reduction in peak amplitude level is comparatively low and changing the nature of wavelet for the first and bottom layer is similar.

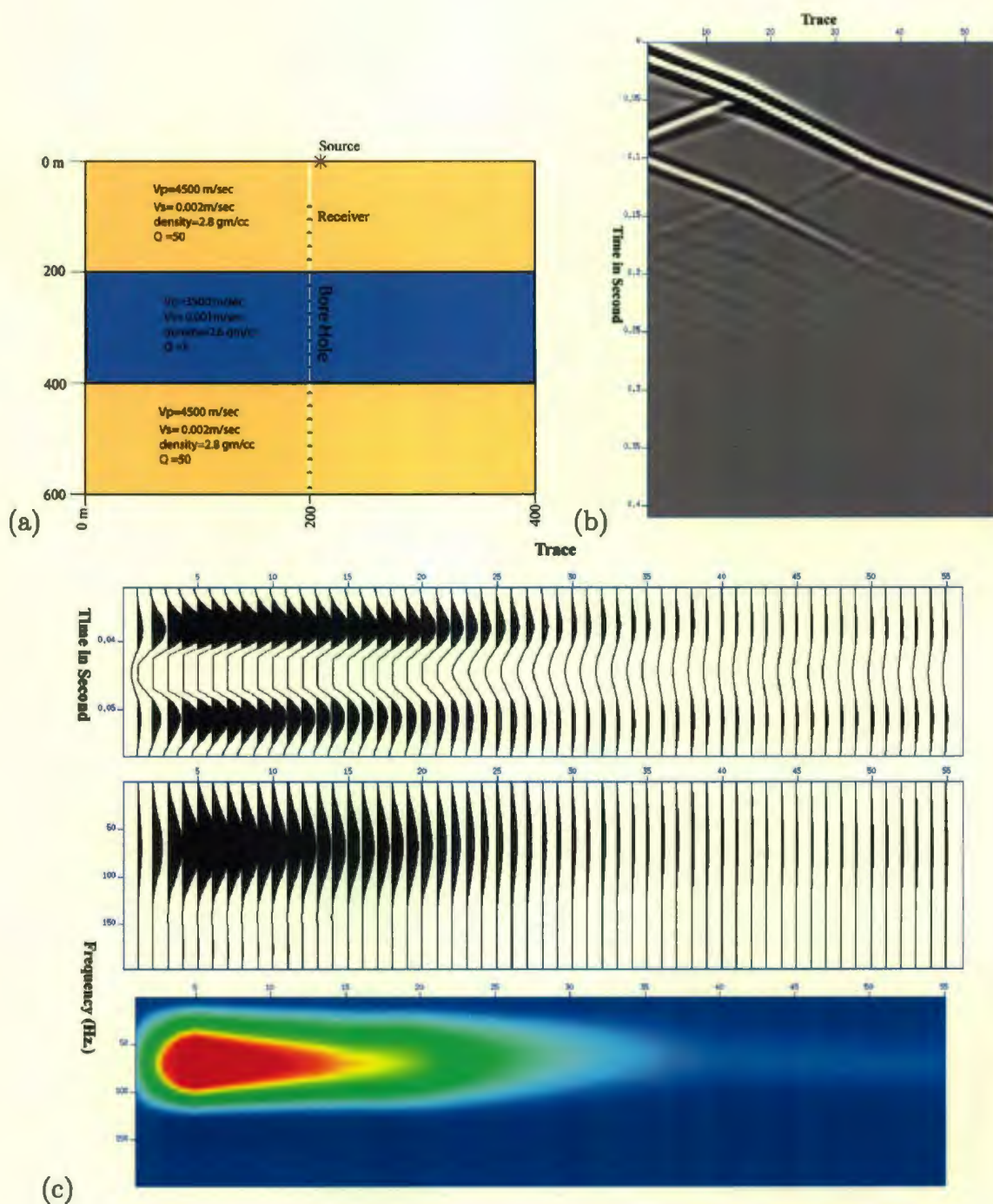


Figure 4.23: Three layer attenuative model with first layer: $V_p=4500$ m/s, $\rho=2.80$ gm/cm³, $Q=50$, second layer: $V_p=3500$ m/s, $\rho=2.60$ gm/cm³, $Q=5$, and third layer: $V_p=4500$ m/s, $\rho=2.80$ gm/cm³, $Q=50$ (a) layer model and VSP source receiver geometry (b) total wavefield in time domain (c) windowed downgoing direct wavefield in time and frequency domain.

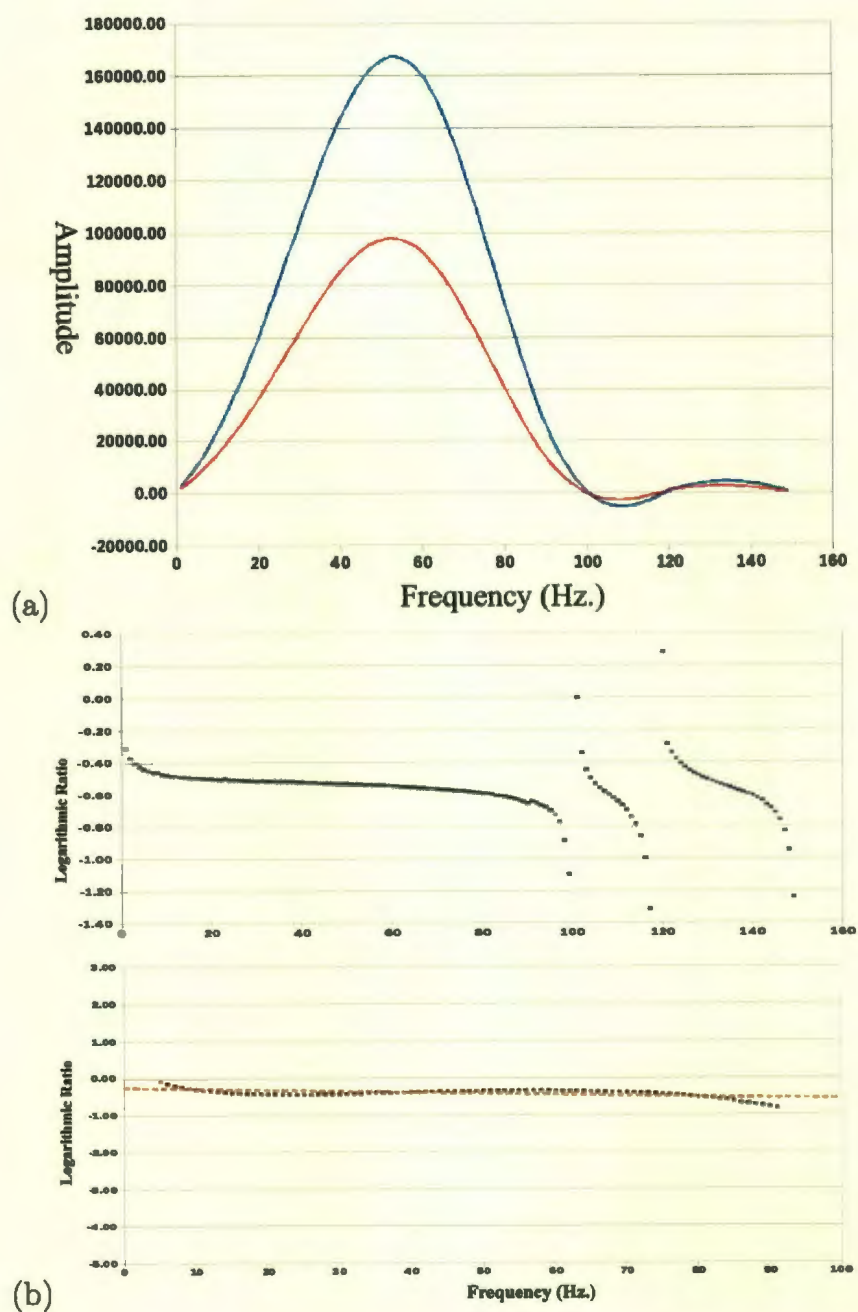


Figure 4.24: Amplitude and spectral ratio of the three layered attenuative model shown in Figure-4.23 (a) amplitude spectra of the traces recorded at 90m (blue) and 190m (red) depth (b) top: logarithmic spectral ratio of total frequency band width, bottom: logarithmic spectral ratio of frequency band width 5-90Hz

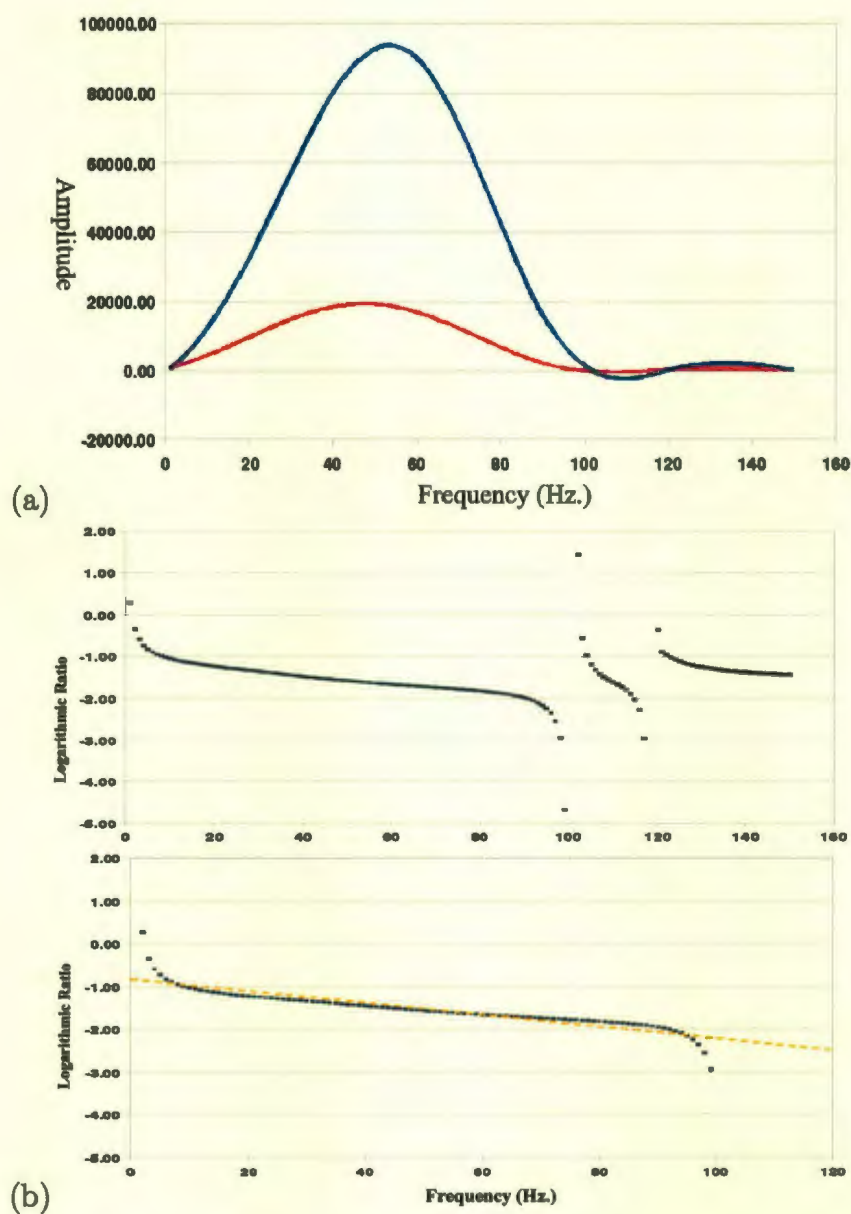


Figure 4.25: Amplitude and spectral ratio of the three layered attenuative model shown in Figure-4.23 (a) amplitude spectra of the traces recorded at 210m (blue) and 390m (red) depth (b) top: logarithmic spectral ratio of total frequency band width, bottom: logarithmic spectral ratio of frequency band width 0-100Hz

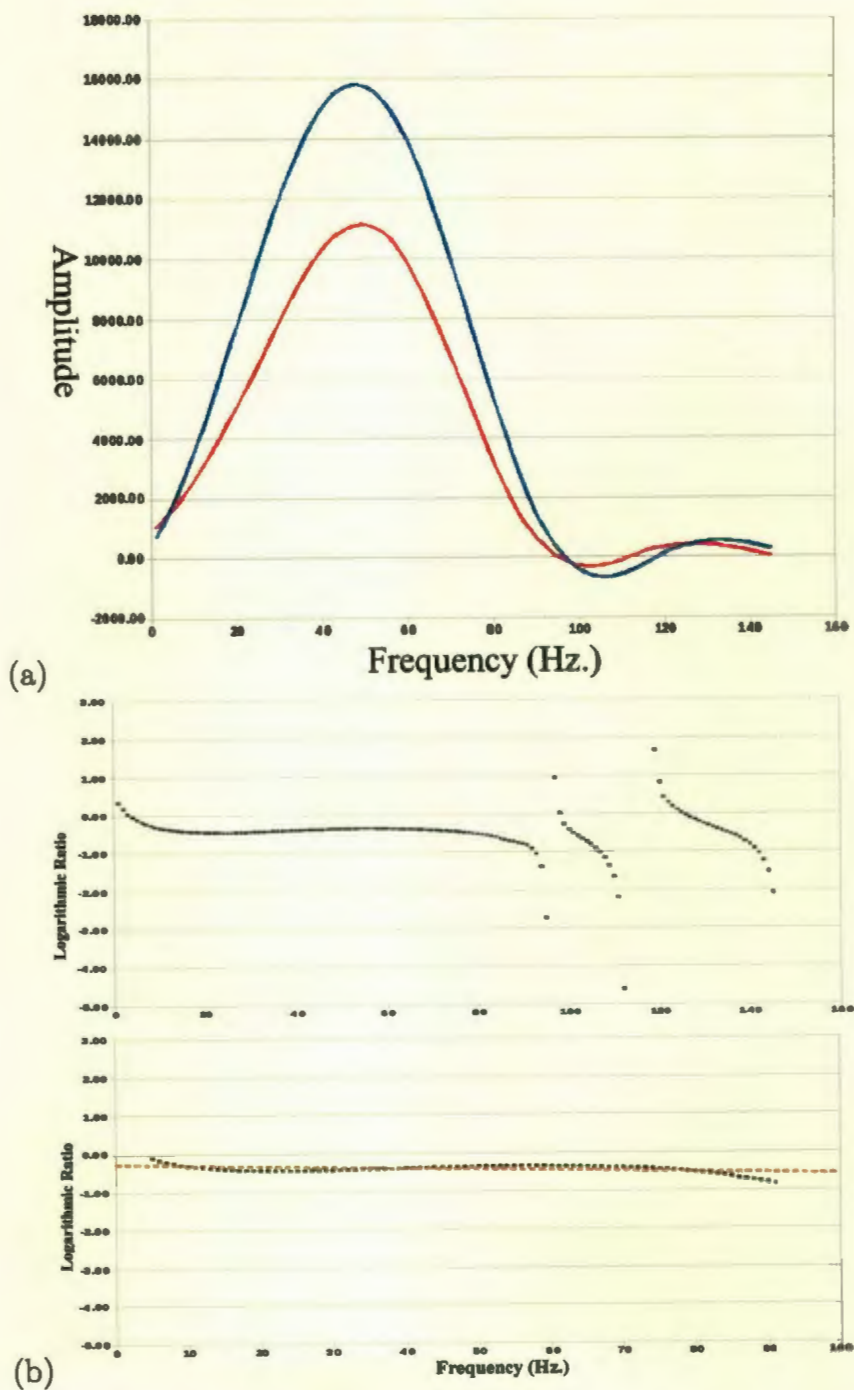


Figure 4.26: Amplitude and spectral ratio of the three layered attenuative model shown in Figure-4.23 (a) amplitude spectra of the traces recorded at 410m (blue) and 590m (red) depth (b) top: logarithmic spectral ratio of total frequency band width, bottom: logarithmic spectral ratio of frequency band width 5-90Hz

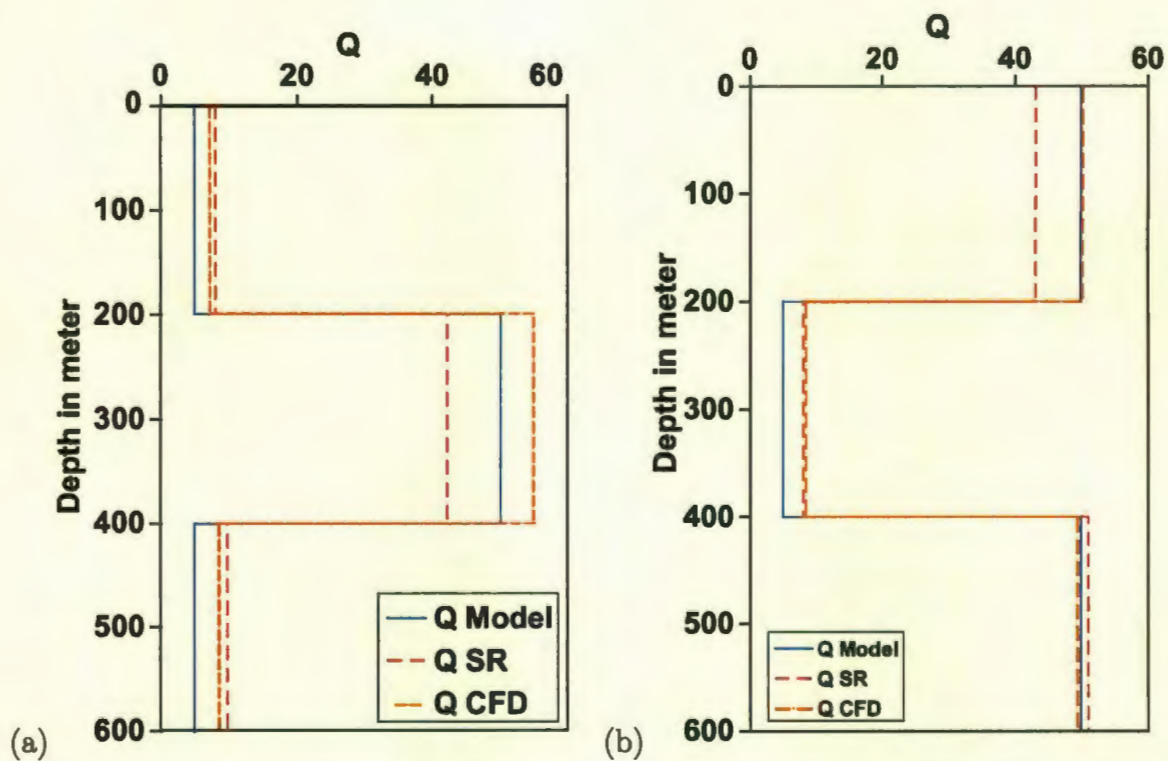


Figure 4.27: Q modeling result where shows model value (blue line) and estimated values from SR (red line) and CFD method (orange line) (a) three layered attenuative model shown in Figure-4.19a (b) three layered attenuative model shown in Figure-4.23a

The reduction in peak amplitude level of the middle layer is high and changing the nature of wavelet become broader and more asymmetric. The best straight line of logarithmic spectral ratio (A_{n+1}/A_n) versus frequency plot of these seismograms is indicated by a dashed line. Layer wise quality factor, Q of the first model is 8.11, 42.17 and 9.88, and 43.16, 8.04 and 51.15 for the second model estimated by using SR method. On the other hand Q estimated by CFD method is 7.2, 55.12, and 8.71 for the first model and 50.32, 8.42 and 49.46 for the second model. The result of Q estimation computed by both SR and CFD method is illustrated in the Figure-4.27 with model Q values.

4.6 Conclusion

A broad variety of methods is available for attenuation estimation of seismic data. In this study we applied SR and CFD method to estimate attenuation factor of numerically generated zero-offset VSP data in homogeneous layered media. The attenuation analysis at different depth intervals and for different frequency ranges is also examined to validate the stability of attenuation estimation on different models. In this model dependent experiments, it showed that the attenuation measurement techniques play better role in simple model than complex model. Model complexity introduces reflection, transmission, scattering effect in seismogram that influence the Q computation. The Q estimation by spectral ratio method of closely spaced receiver pair is more erroneous than that of the receiver pair spaced comparatively larger depth; because the scattering effect tends to influence the amplitude spectra more when the receivers

are close enough. Our result suggests that it is reasonable to draw a conclusion about seismic attenuation at maximum frequency band width of 0-150Hz. The over all estimated Q values of different models is high 50 ± 6 and low 5 ± 3 respectively. Despite of the uncertainty in wave field separation, widowing, first break time picking, selection of right frequency band width, multiple suppression etc. the main conclusion drawn from this study is that it has been successful in Q estimation of different layered earth media.

Chapter 5

Forward Q Modeling of Field VSP

5.1 Introduction

The data set analyzed in this study is the VSP survey data of the Lalmai well-3, located in the Lalmai structure, onshore Bangladesh. This survey includes a suit of zero-offset 2D VSP, depth ranges from 35.9 to 2743m. This case study is focused on the estimation of compressional wave attenuation and characterize the prospective gas reservoirs. Two different methods, spectral ratio and centroid frequency downshift method has been used and that provides an opportunity to validate the accuracy of attenuation measurements. The sensitivity of attenuation analysis of different depth intervals on different frequency band width and borehole irregularities were also examined to validate the stability of attenuation estimation.

5.2 Description of VSP data

The Baker Atlas Downhole Service recorded the VSP data for Tullow Bangladesh Limited on May 19, 2004 at the Lalmai well-3. All the equipment was tested prior to the VSP survey. Baker Atlas employed standered techniques for the zero offset VSP survey. The drilling and logging program of this well was designed to acquire a

complete suite of borehole logs including caliper, gamma ray, density, neutron porosity, resistivity, sonic and VSP (zero-offset). This VSP survey was carried out over a depth range of 35.9 to 2743m with 30m recording interval. The acoustic log was recorded over 1043 to 2776m MD (Measured Depth) below DF (Derrick Floor). The TVD (True Vertical Depth) corrected acoustic (sonic) log was then calibrated by using the VSP data on the above depth interval and then this calibrated acoustic log used to generate synthetic seismigram.

5.3 VSP Data Acquisition

The energy source used for this survey was 2×200 cubic inch Bolt Air gun. The source location for the survey was 66m, 280° north from the wellhead and the source depth was 4.0m below ground level (Figure-5.1). A reference hydrophone positioned at 0.7 metre above the source, was used for timing and source energy monitoring purposes. The VSP survey was conducted in well inside the tubing of 4 inch size using a single ESR receiver (a slim hole downhole geophone tool) with three components geophone. The VSP data consisted of 76 records between the depth level 35.9 and 2743m below DF. The data was recorded at 35.9, 530, 560m depth and continuously with 30m spacing from 560 to 2743m. At the beginning of VSP survey the wireline depth survey was zeroed at the DF elevation and the single level receiver string consisting of one downhole receiver with three components geophone was lowered in the well. During the down trip the geophone receiver was stopped to check the equipment performance and check shot data was recorded at depth 2010 and 2520m. Then the geophone

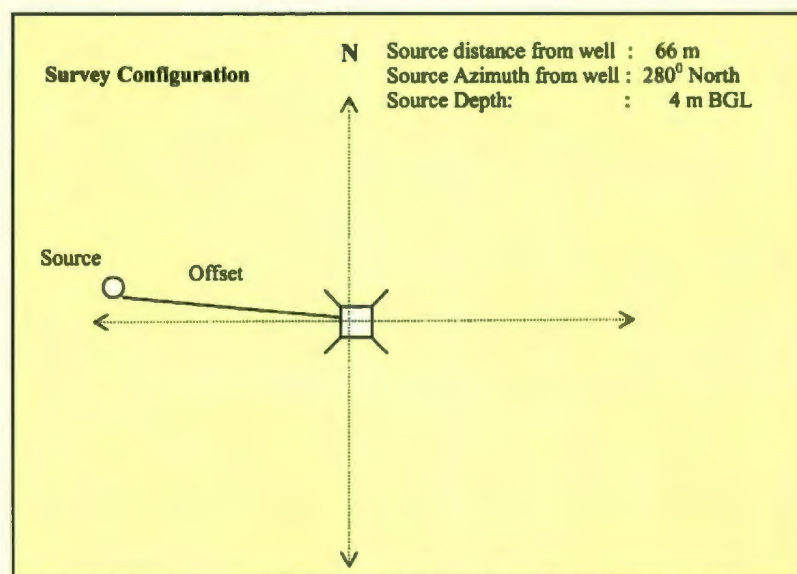


Figure 5.1: VSP acquisition geometry of Lalmai well-3.

receiver lowered to the TD (2743m) and recording proceeded as the geophone pulled up to the 35.9m depth level. During recording at each downhole station the wireline cable was stopped and the geophone string clamped to the borehole wall by means of a remote control locking arm to the tool. Using of this locking arm tool in the slim hole VSP recording, enhanced the coupling condition VSP as much as possible. The over all coupling condition of the field VSP data used in this study is good except a few records in the shally sequence of Bokabil formation.

5.4 VSP Data Processing

A total of 73 VSP records between 590 and 2743m measured depth below DF have been used in the VSP data processing. Due to excessive noise the VSP records at 35.9m, 530m and 560m were not kept in VSP processing, the rest of the VSP traces are plotted in trace normalized form. Different types of events can be identified in these

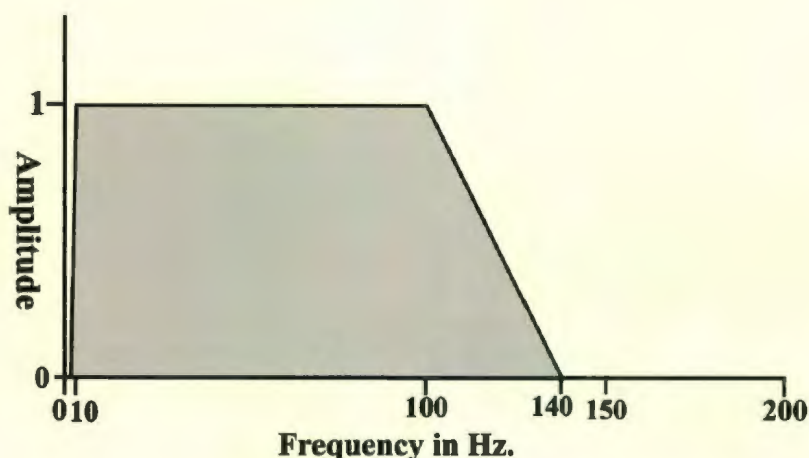


Figure 5.2: Bandpass filter (5,10-100,140Hz) in frequency domain.

data set such as the upgoing event, down going events, different order of multiples etc. The data set is affected by the presence of random noise. Before starting processing of VSP data, the first break time of downgoing direct arrival is picked on raw vertical component of the VSP records. The first break picking was performed manually over 73 records before starting VSP processing. After first break time picking the random noises were subtracted with a zero phase bandpass filter (5,10-100,140Hz) shown in the Figure-5.2. Then the vertical geophone component of traces were edited and stacked. A compensation for amplitude decay due to the spherical divergence effect was applied to the data set using an exponential gain function, before starting the separation of downgoing and upgoing wavefield. The downgoing first arrival was flattened by using the first arrival time. Each trace was cross-correlated with a selected reference trace using a time window around the first arrival, and the first arrival time was subsequently shifted to ensure maximum coherency of downgoing wave. An 11

point median filter was applied over the total wavefield to pass the flattened downgoing waves. Following the median filtering a zero phase bandpass filter (5,10-70,110Hz) was used to remove the ambient noise. The flattened downgoing event was subtracted from the total wavefield to get the upgoing reflected wave and then shifted to convert two-way time below the datum as an undeconvolved unenhanced up wave shown in the Figure-5.3. This was followed by a zero phase frequency bandpass (5,10,70,110Hz) filter. This display describe the primary, and multiple reflector response of the subsurface at the borehole location within and below the total depth of the VSP. The separated downgoing wavefield and it's 0.18s to 0.30s (120ms) time windowed section is shown in the Figure-5.4. This time window frame isolates the downgoing direct arrival event from the total downgoing event. The FFT (Fast Fourier Transformation) operation was applied on this 120ms time windowed section to transform from the time domain to the frequency domain. The amplitude spectra of frequency domain section is shown in the Figure-5.5 has been used for Q computation.

5.5 Data Preparation for Q estimation

As we described in previous chapter, accurate estimation of intrinsic attenuation is a difficult task and it is highly sensitive to different attenuation factors. The choosing of receiver pairs and frequency band width can be manipulated the Q computation of VSP data acquired at different depth levels within a given subsurface interval. A reliable Q estimation is obtained when the slope of the spectral ratio plot is large compare to its variability. Thus to have a larger slope one needs to maximized

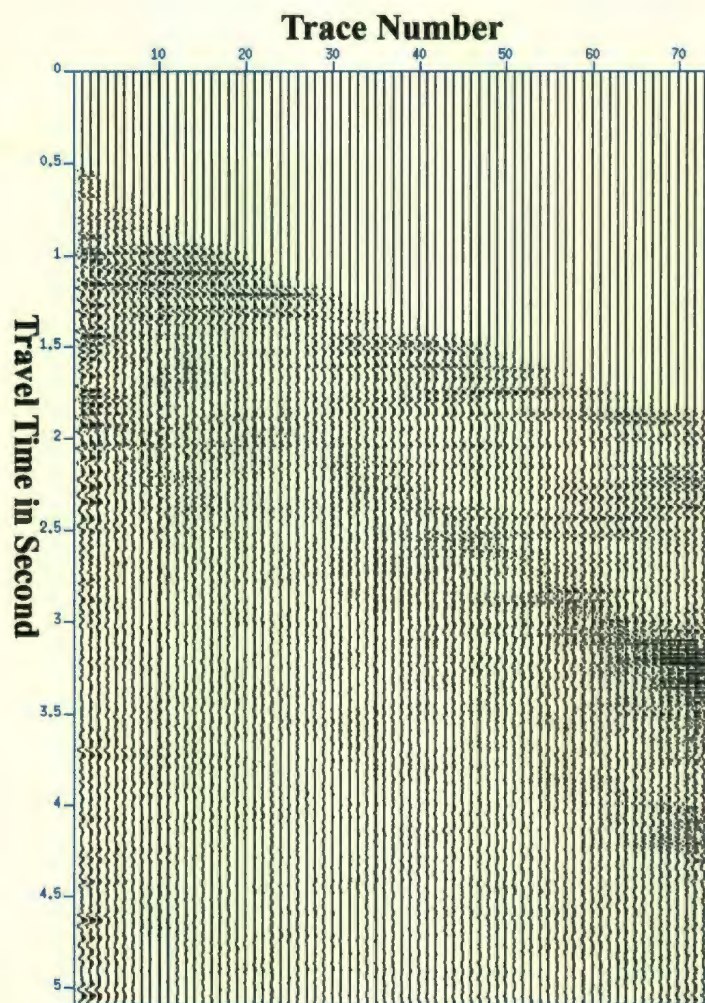


Figure 5.3: Separated total upgoing wavefield (reflected wave) of VSP from Lalmai well-3

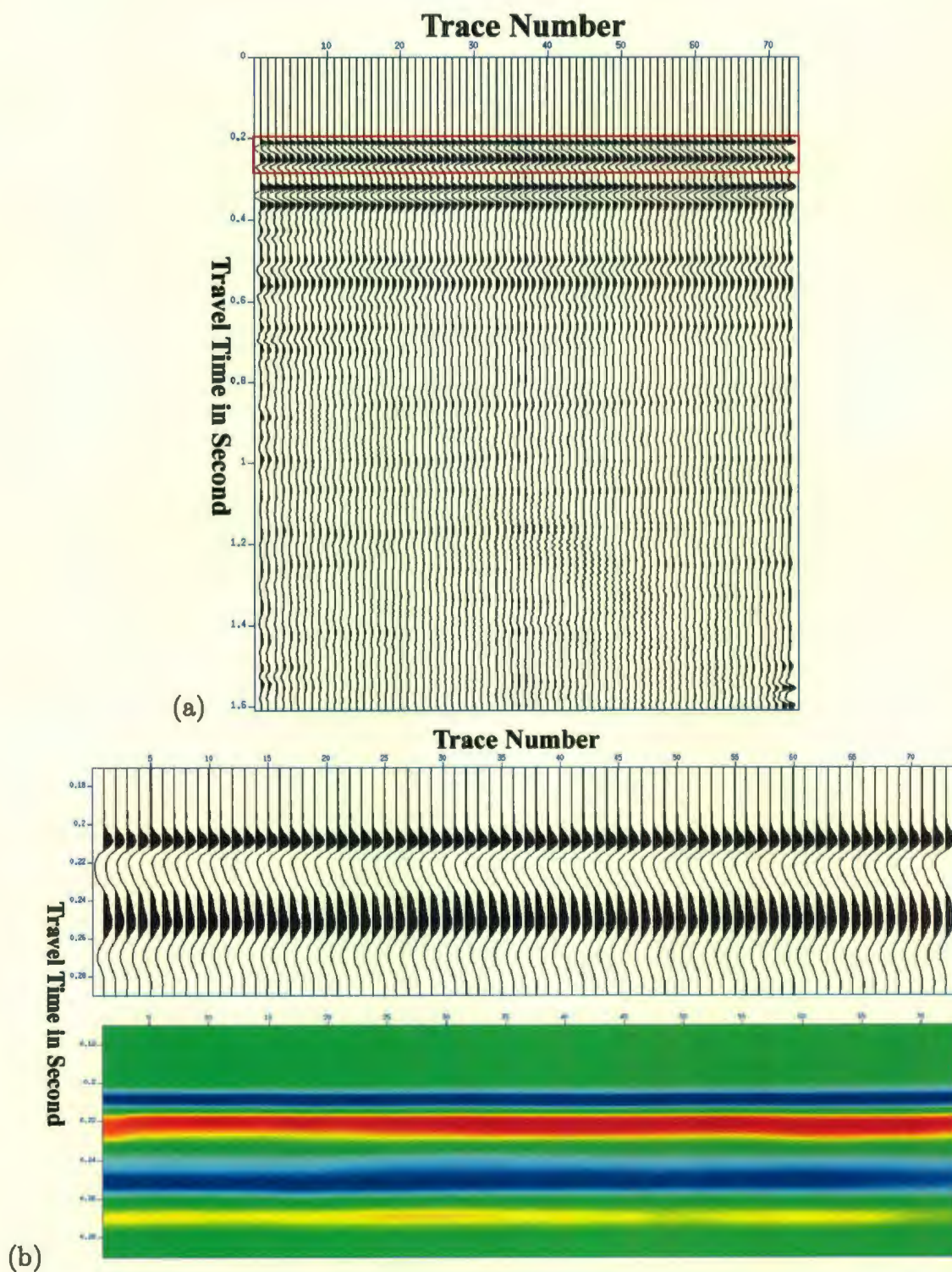


Figure 5.4: Separated downgoing wavefield (direct arrival) of VSP from Lalmai well-3. Red box indicates the 120ms time window (a) total downgoing wavefield (b) 120ms windowed time section

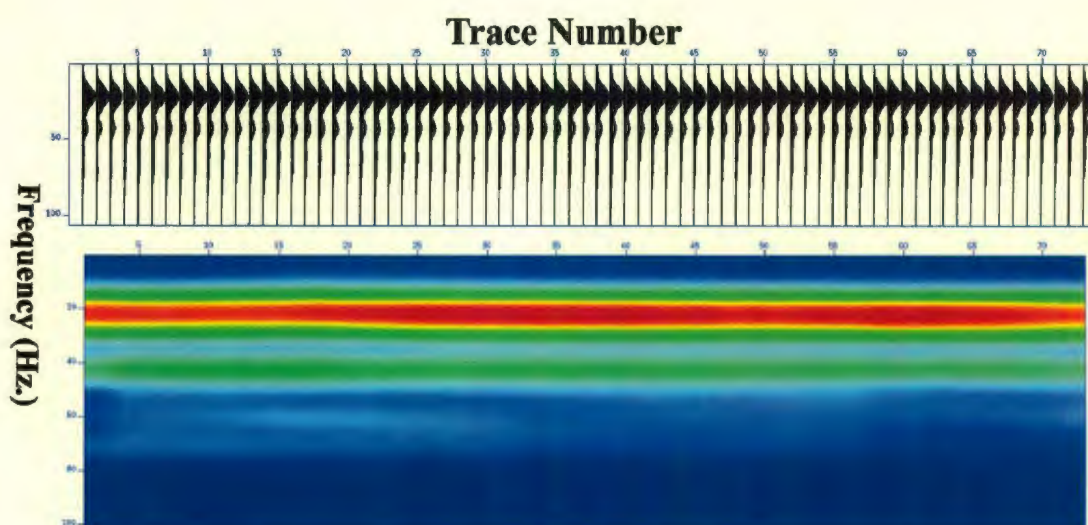


Figure 5.5: Windowed downgoing wavefield (Figure-5.4b) in frequency domain.

the receiver separation. In this study we checked all the 73 traces and chose each consecutive trace pairs to get the amplitude spectral ratio and calculate the average attenuation between two receivers distance (Figure-5.6). To get accurate Q estimation it is important to identify the right frequency band width over the whole frequency range, because the amplitude spectra do not always have the information within the whole frequency band width. This is because the source signal may not carry all the frequencies itself or even it has the information on some of these frequencies and might be either interfered by noise or attenuated during propagation. The key thing is to determine which part of the signal carry the source signature or which part of the amplitude spectra contains useful information. Sometimes it is contaminated by noise and/or by other signal's interference. To have a correct attenuation we have to eliminate the ambient noise and all kinds of interference of other signal from the data set. The convention of frequency band width selection is explained in the Figure-5.7

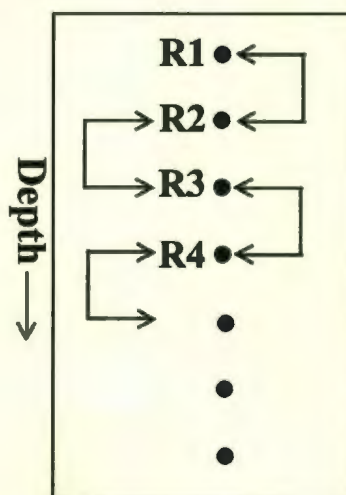


Figure 5.6: Cartoon of pairing the receivers for interval attenuation estimation.

and Figure-5.8. The Figure-5.7a shows the amplitude spectra of receiver pair at 2480 and 2510m depth level. It is the general phenomena that in the vertical propagating wavefield, amplitude spectra or energy is decreased downward. Finding the low and high limits of the frequency band width help to resolve the interference of other spectra or noise. Generally the amplitude spectra of a trace at shallower depth is higher than that of a trace at deeper depth. The low end of the frequency of both trace is zero but they do not intersect with each other. On the other hand in the high end of the deeper trace intersects with shallower trace at 100Hz frequency and it becomes equal or higher after the 36Hz frequency. In the Figure-5.7c it shows the logarithmic spectral ratio of the traces at 2480 and 2510m depth that represents a negative slope for the frequency band width 5-35Hz which has given a reasonable Q estimation by both SR method ($Q=41.46$) and $Q=49.81$ is estimated by CFD method for frequency band 0-108Hz. Figure-5.8 shows the amplitude spectra of the trace pair at 2540 and 2570m depth levels, where the above rule did not work. The amplitude spectral

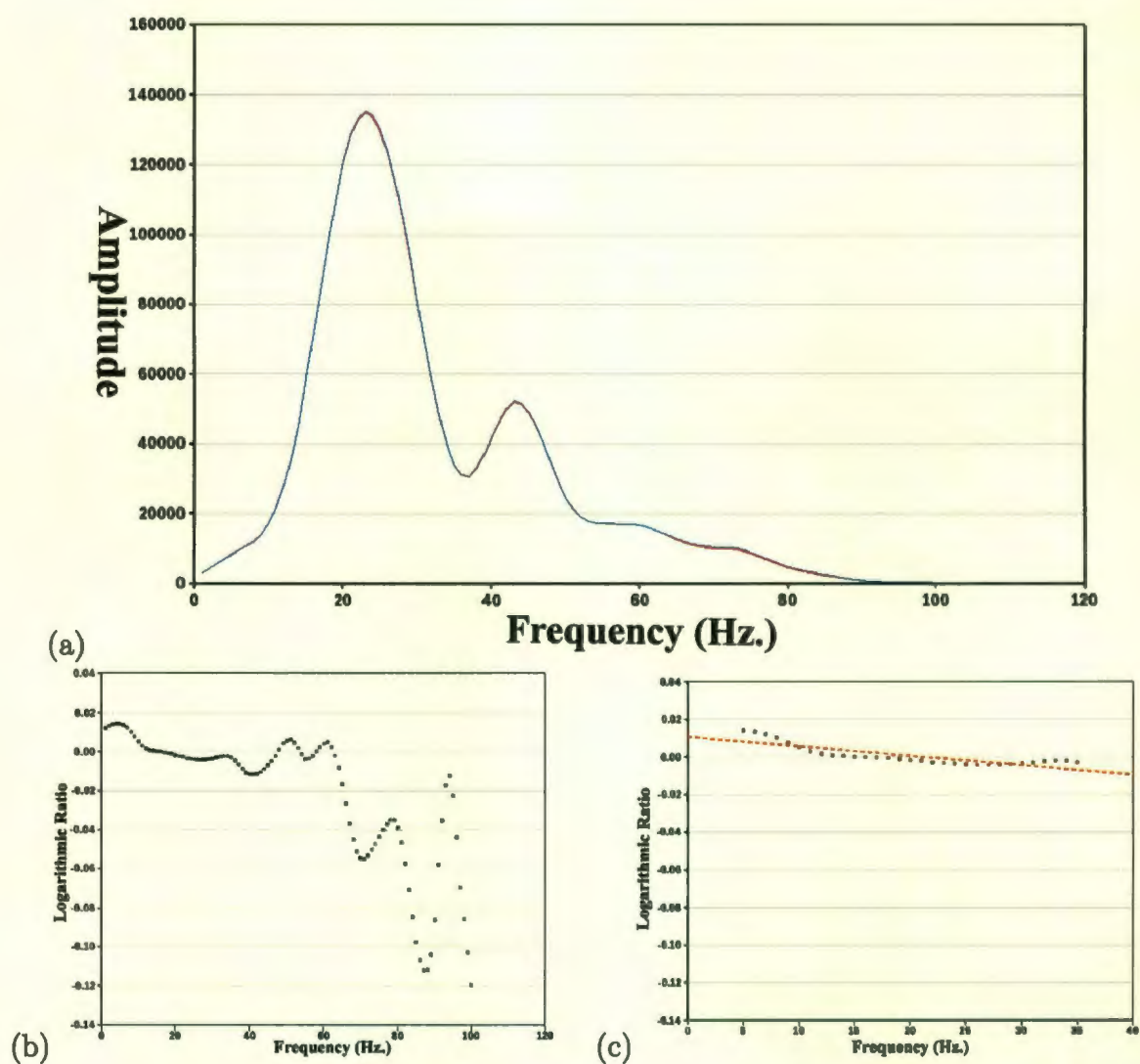


Figure 5.7: Amplitude spectra and spectral ratio of the traces recorded at 2480m (blue line) and 2510m (red line) depth (a) amplitude spectra (b) logarithmic spectral ratio of total frequency band width (c) logarithmic spectral ratio of 5-35Hz frequency band width

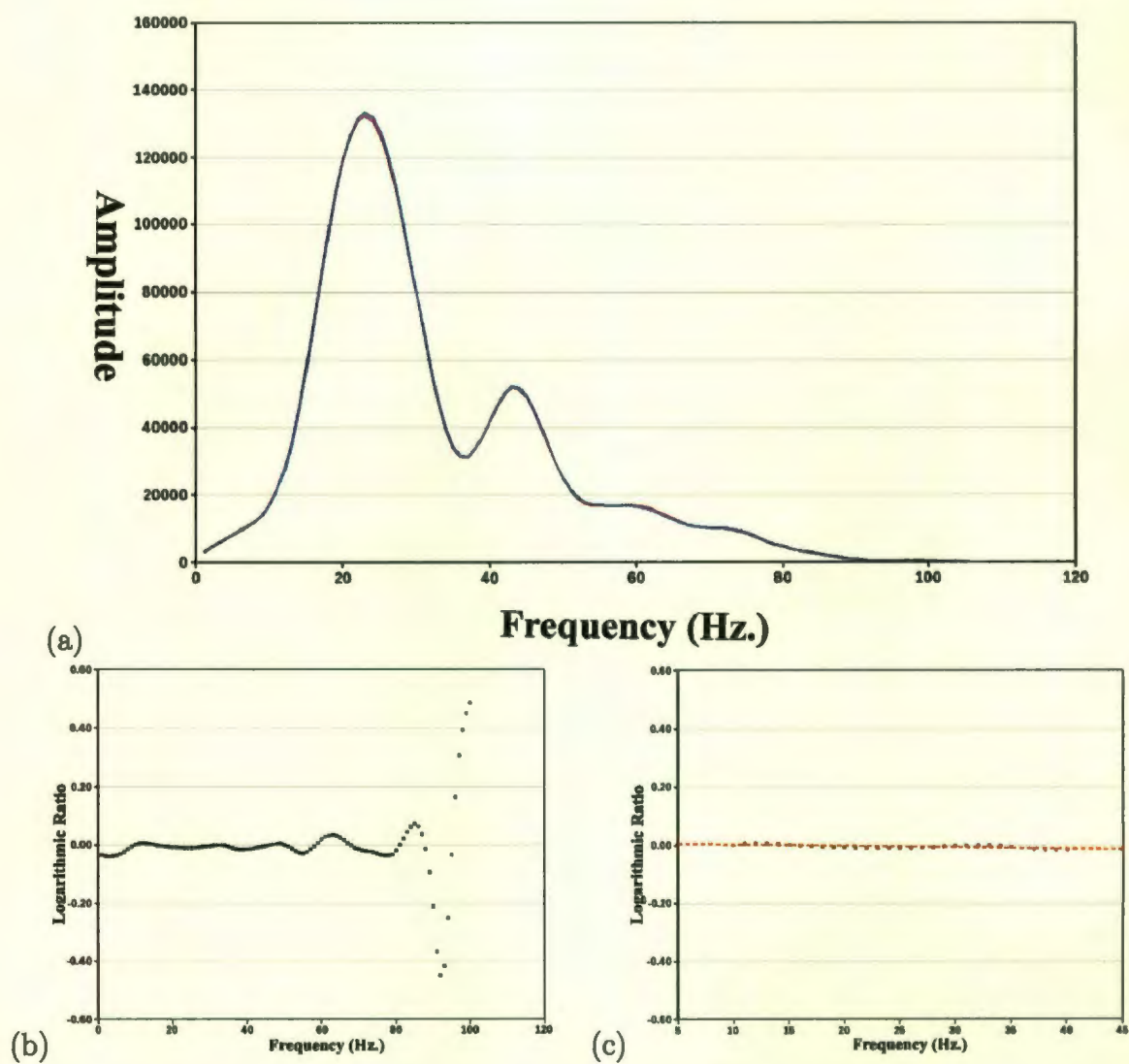


Figure 5.8: Amplitude spectra and spectral ratio of the traces recorded at 2540m (blue line) and 2570m (red line) depth (a) amplitude spectra (b) logarithmic spectral ratio of total frequency band width (c) logarithmic spectral ratio of 5-35Hz frequency band width

ratio plot of the frequency band width 0-100Hz shows in the Figure-5.8b where the ratio plot represents a positive slope, which means a negative Q value. Apparently it seems that there are some other effect in the spectrum. If we examine the traces shown in the Figure-5.8a very carefully the amplitude spectral difference from 25 to 35 Hz is constant that means there has been some apparent interference. In this part noise can not be suppressed properly or might have some other processing effects. As shown in the Figure-5.8c only the frequencies between 10-35Hz can be used for Q estimation and the rest of the spectra is omitted for having noise interference. The ratio plot in the Figure-5.8c for 10-35Hz frequency bandwidth represents a negative slope which gives a positive Q value.

5.6 Q Computation

5.6.1 Application of SR and CFD Method

Since we saw in the Chapter-4 that both SR and CFD method validate and cross checked in different ideal synthetic models and the Q estimation is reasonable in both methods. The prime goal of this section is to apply these two methods to perform the Q estimation over total VSP depth for each receiver pair and to find out the attenuative zone for characterize the gas bearing zone within the total VSP. To have the optimal Q estimation we applied these two methods after having the downgoing direct arrival event of all 73 traces and doing the all processing steps, i.e. trace editing, filtering, trace normalization, choosing the right frequency band width, minimization

of uncertainty in obtaining the right spectral ratio and slope of its linear plot etc. After doing all of the processing steps the downgoing direct arrival of VSP data strip is ready for SR and CFD Q estimation.

5.6.2 Spectral Ratio Method

The field traces always show the sign of attenuation because of combined effect of extrinsic (geometric spreading, scattering effect etc.) and intrinsic attenuation. In this case attenuation or energy loss happened not only by absorption of media but also it caused by delay or energy sent elsewhere by multiple scattering, reflection or transmission. The geometrical spreading correction and multiple suppression have been done as much as possible. The amplitude spectra picked for 120ms time window of downgoing direct arrival event over all the 73 traces. We observed that the relative loss of spectra decreases linearly with frequency. After examining amplitude spectra of all 73 traces, choose right frequency band width and calculation of logarithmic spectral ratio, we calculated the Q for each trace pair. SR Q estimations were done for different frequency band widths i.e. 0-35Hz and 0-100Hz. Q estimation of most of the receiver pair shows a reasonable value but a few receiver pairs show negative Q values. The apparent Q estimation of gas bearing zone and the average interval Q estimation of each formation also done by SR method.

5.6.3 Centroid Frequency Down Shift Method

Centroid frequency down shift attenuation estimation technique has been applied to the selected VSP survey data after doing all steps of data processing and picking the amplitude spectra of all the 73 traces. Then we calculated the centroid frequency f_c and variance σ^2 of all trace records for windowed data set and the centroid frequency down shift Δf_i of each successive depth levels. The chosen frequency band widths are 0-100Hz and 0-108Hz. We selected a time window of 120ms that isolates the downgoing first arrival event from the total wave field. Here we consider that the shallower trace record (i) is as input source and the deeper trace record ($i + 1$) is as output source for each receiver pair. The first break travel time for each depth level has been picked manually. The Q estimation of gas bearing zone and the average interval Q estimation of each formation also done by CFD method.

5.7 Result and Discussion

Using all the available bore hole log data (e.g. caliper, gamma ray, resistivity, velocity, acoustic, density log etc.) we constructed a 1D lithologic model (Figure-5.9) of total drilled section of the Lalmai Well-3. In the Figure-5.9 the log curves demarcates the lithologic boundaries of Tipam-Bokabil and Bokabil-Bhuban formation and these boundaries are well matched with reflectors in VSP and synthetic seismograms. The interval velocity analysis result shown in the Figure-5.10, illustrated that there are a few low and high velocity zones have been identified within the Bhuban formation.

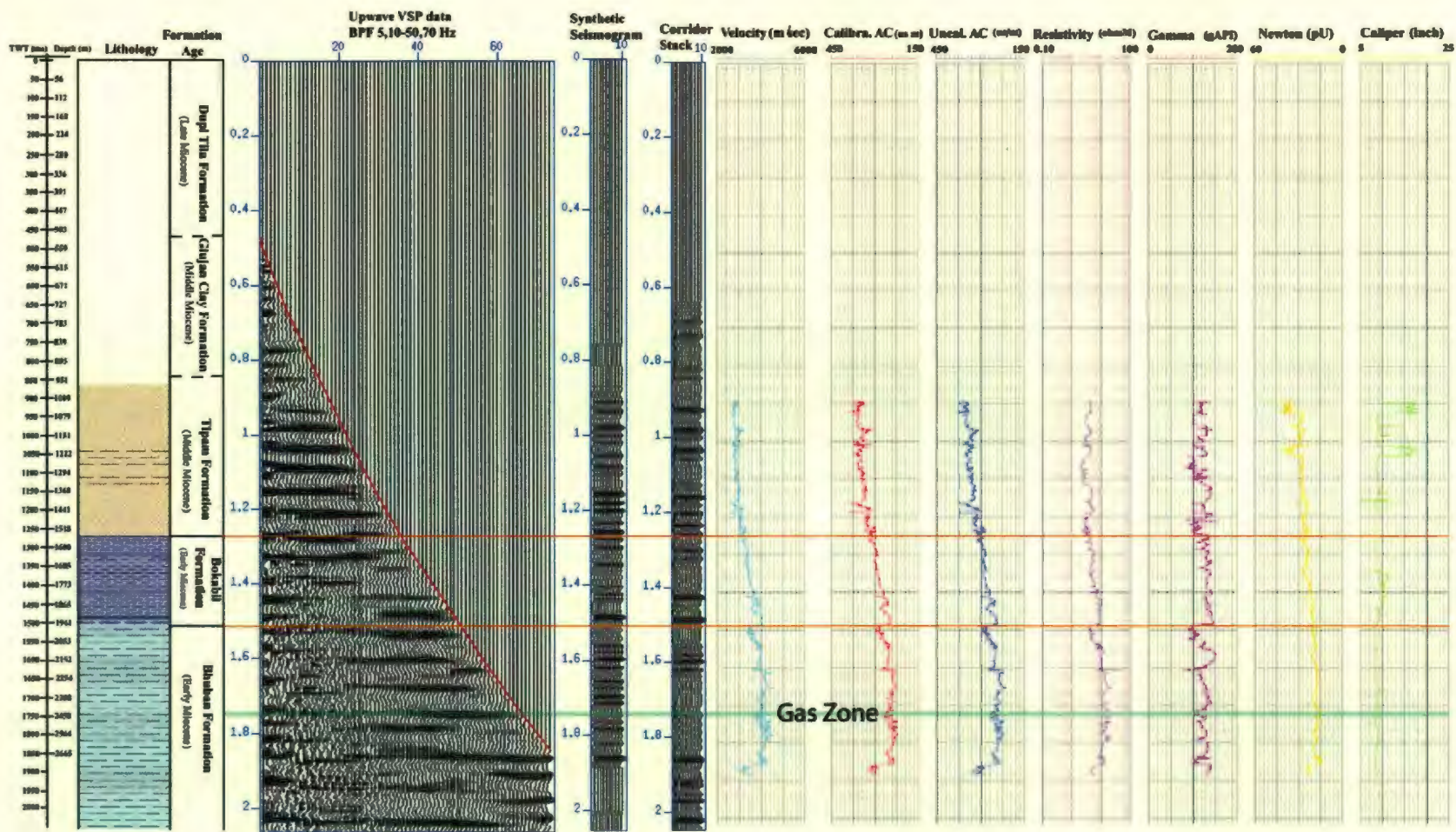


Figure 5.9: Showing the interpretation and correlation of VSP and logs data of Lalmi well-3. Left panel: lithologic unit in both time and depth scale, middle panel: upwave VSP event, synthetic seismogram and corridor stack data, right panel: velocity, calibrated acoustic, uncalibrated acoustic, resistivity, gamma ray, newton porosity and caliper log data. The orange lines indicate formation boundaries.

The low velocity zone at 2420 to 2460m depth which matched with gas bearing zone. Upon the validity study of Q estimation methods on different synthetic models in Chapter-4, we used SR and CFD methods for the forward Q modeling of field VSP data. The 73 VSP trace records between 590 and 2743m depth were kept in account for forward Q modeling scheme. For Q estimation in this study we choose 120ms time window to isolate the total downgoing wave field from the total wave field and this narrow window can minimize the effect of interference of the upgoing waves. The Q estimations have been done on this 120ms time windowed data for each trace pair, over each formation and apparent Q for gas bearing zones at 2420 to 2460m depth separately. Figure-5.11, Figure-5.12 and Figure-5.13 shows the total Q -depth profiles for the VSP data by using the SR and CFD methods. Here we estimated Q between two consecutive traces where the shallower traces are considered as the source spectrum and the deeper one is as the received spectrum. The attenuation analysis of each trace pair gives interval Q instead of average Q values. It shows that both in SR and CFD model, the lower part (Bhuban) and middle part (Bokabil) is comparatively higher attenuative than the upper part (Tipam). In Figure-5.11, Figure-5.12 and Figure-5.13 we also see some physically unrealizable phenomenon of negative attenuation, which has been reported previously in VSP attenuation studies (Jannsen et al., 1985, Matsushima, 2007). This negative attenuation means that the amplitudes of high frequency components are increasing with increasing depth, scattering effect, ambient noise, spectral distortion by imperfect windowing, multiples, interference of other signals or improper choices of receiver pair. The formation wise

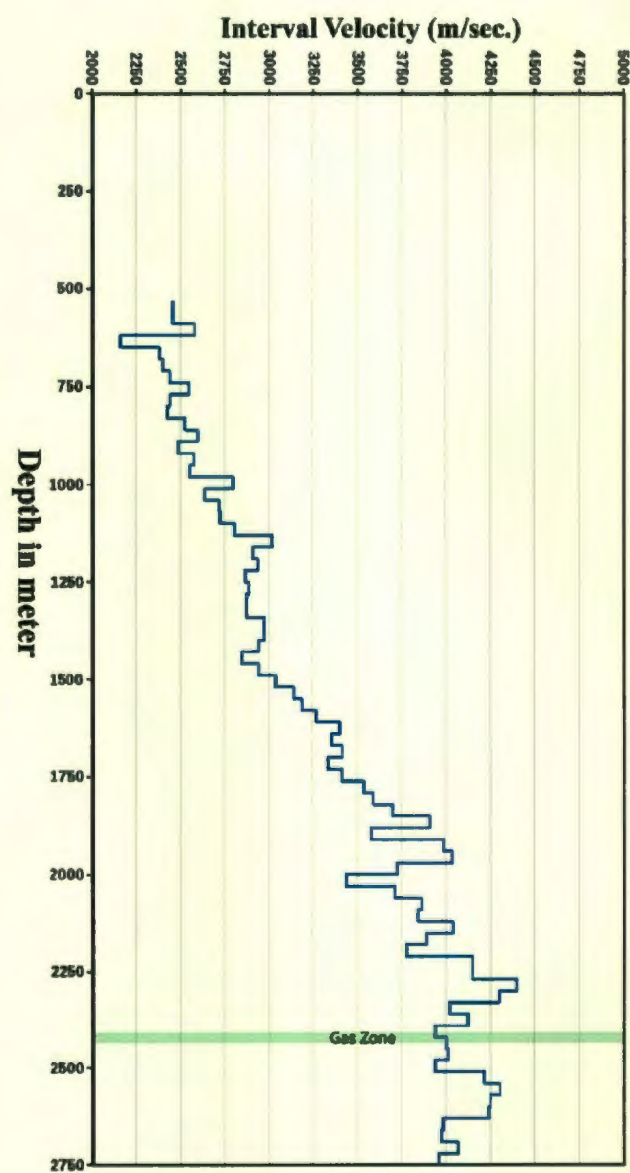


Figure 5.10: Display of interval velocity profile of the VSP data from 530m to 2743m depth

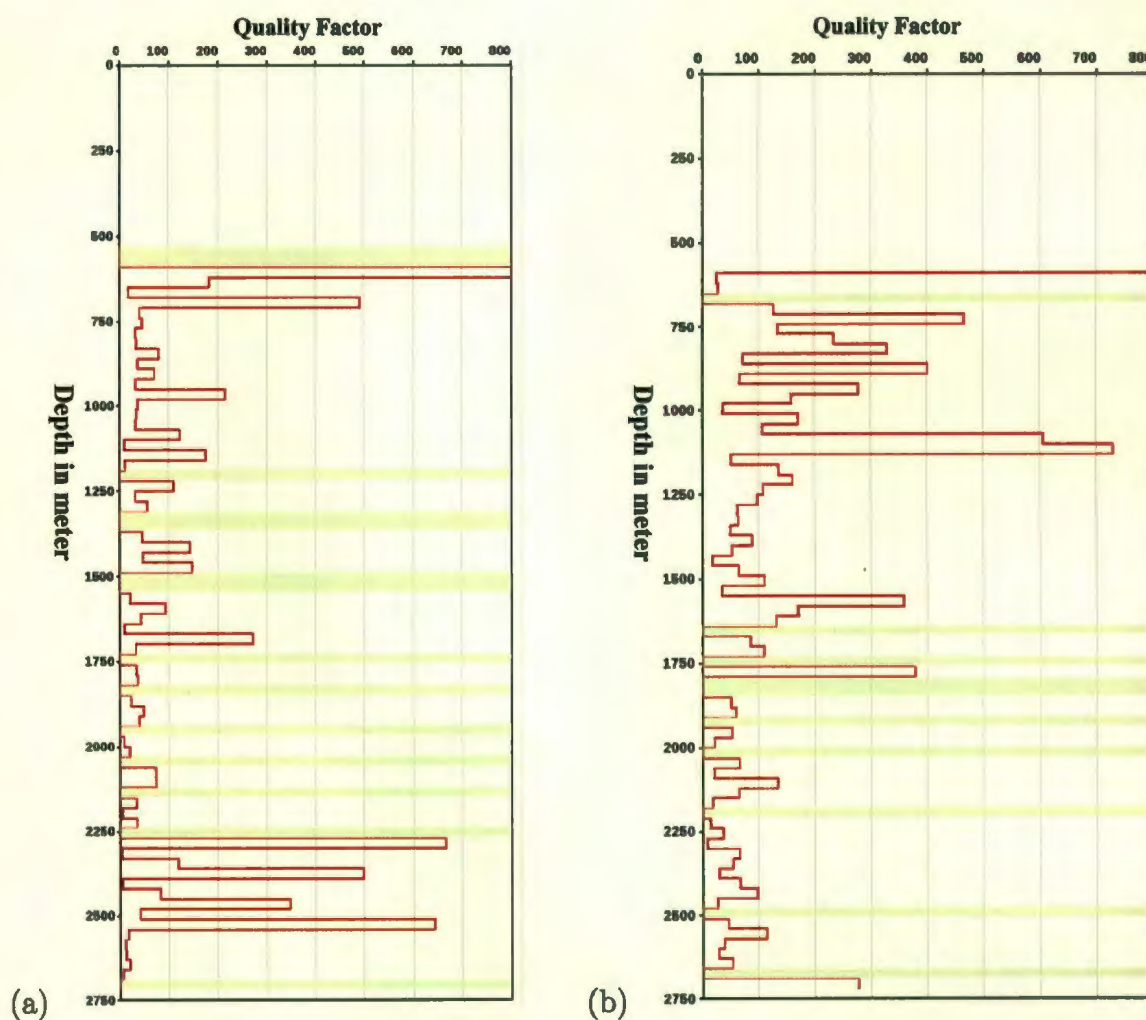


Figure 5.11: Total Q -depth profile for the VSP data of Lalmai well-3 with 30m interval from SR method (a) Q estimated over 0-35Hz frequency band width (b) Q estimated over 0-100Hz frequency band width.

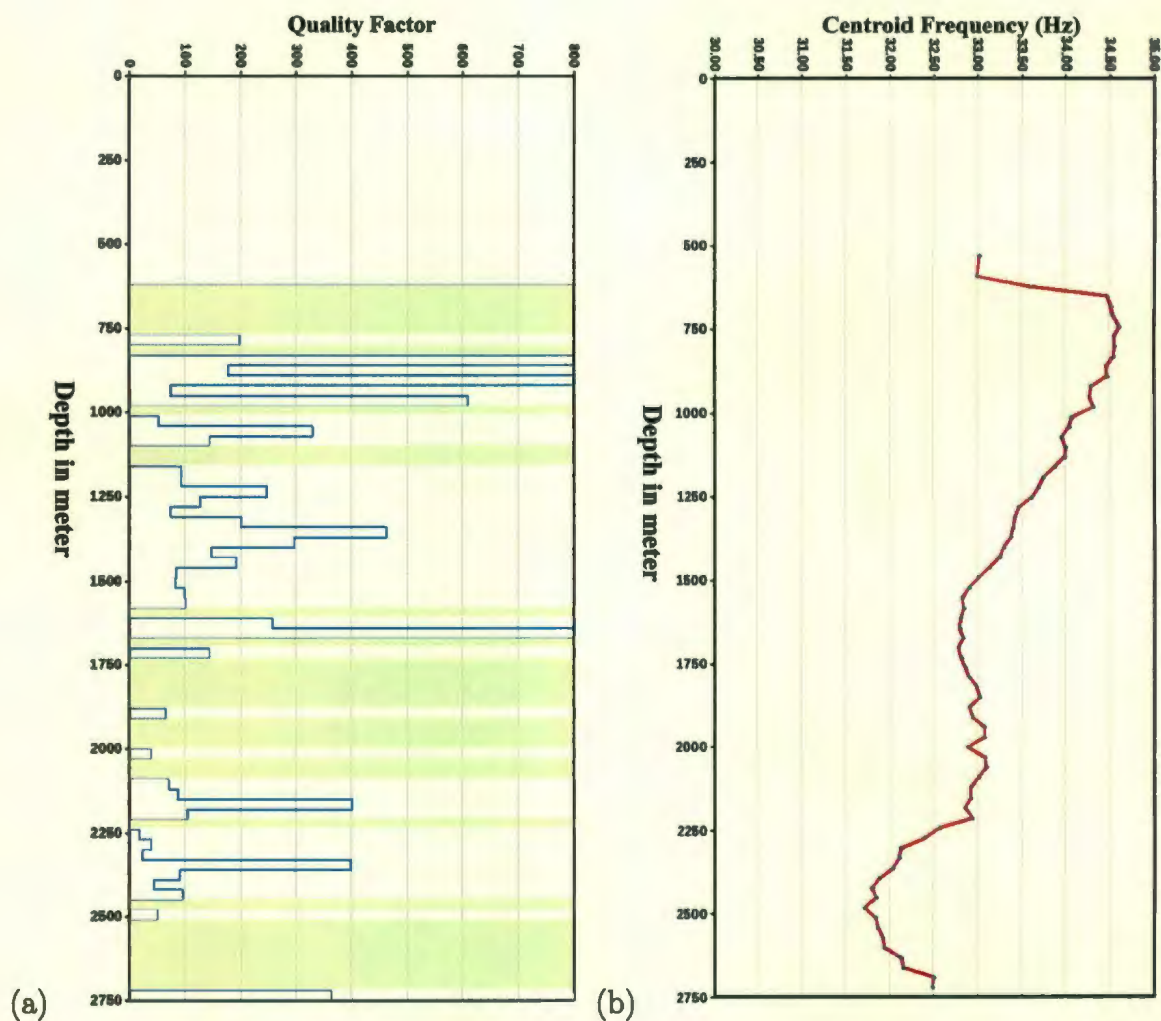


Figure 5.12: Total Q -depth profile for the VSP data of Lalmai well-3 with 30m interval from CFD method (a) Q estimated over 0-100Hz frequency band width (b) centroid frequency-depth profile.

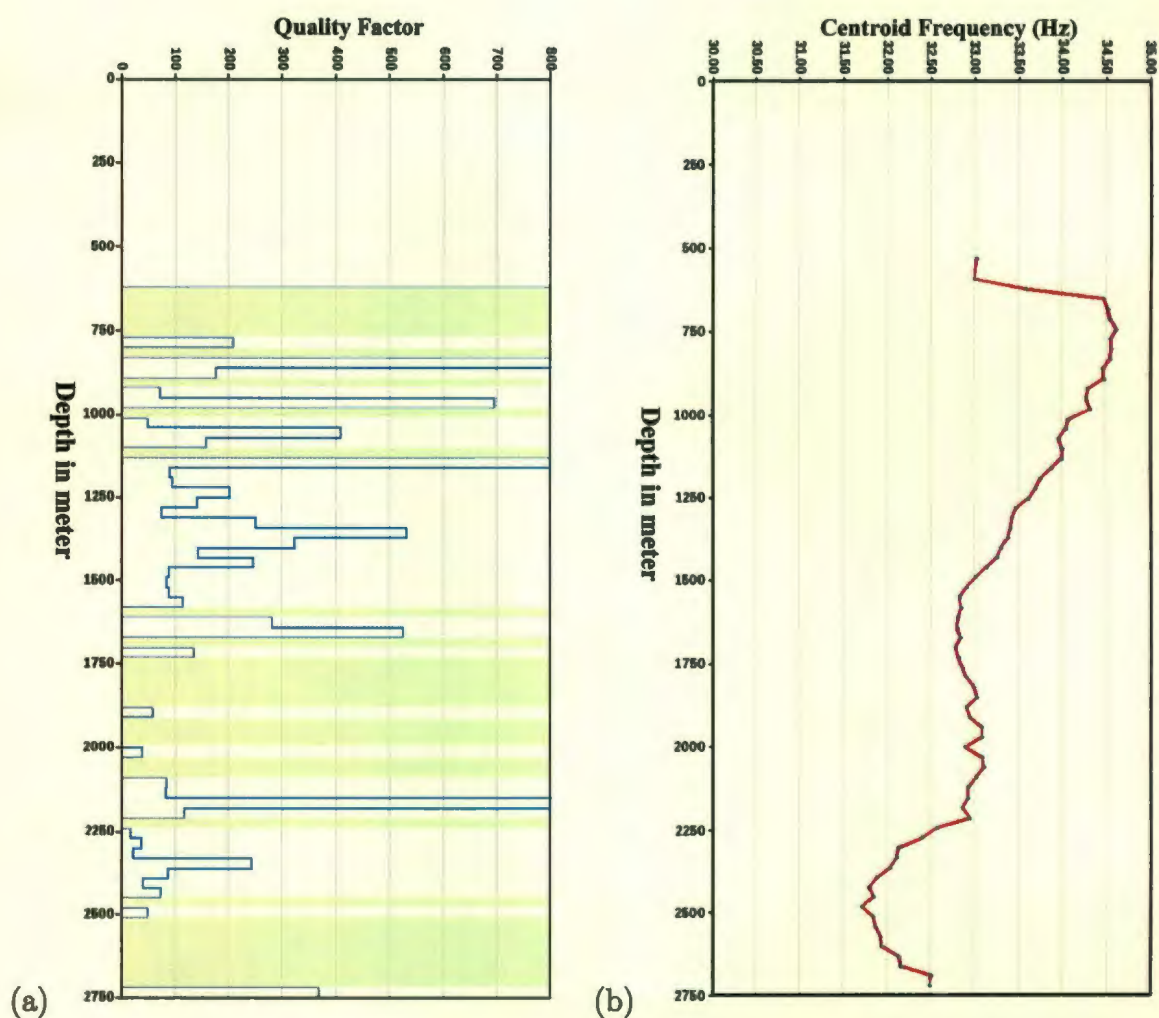


Figure 5.13: Total Q -depth profile for the VSP data of Lalmai well-3 with 30m interval from CFD method (a) Q estimated over frequency band width 0-108 Hz (b) centroid frequency-depth profile.

average Q modeling and apparent Q modeling of gas bearing zone is illustrated in the Figure-5.15. The Tipam formation is composed of sandstone. The result obtained from both SR and CFD methods applied to the VSP data recorded at 1000 to 1520m is 70 and 74.81 respectively which indicates comparatively low attenuative. The Bokabil formation is composed of shale with minor sandstone and the Bhuban formation is composed of sandstone with alternating shale. The attenuation result obtained from the VSP data recorded within these two formations by the SR and CFD methods is 78.04, 69.45, and 58.11, 63.20 respectively. The attenuation of the Bhuban formation is higher than that of Tipam and Bokabil formation. These two techniques yield an average estimation of Q over the whole depth interval. The larger depth interval gives a better Q estimation values and the estimation over a shorter depth interval leads to greater uncertainties. The ultimate goal of relating measured Q to lithology seems unrealistic in some parts of the VSP because thinner layering and velocity gradients may influence the amplitude spectra considerably (Trappe, 1988). The accurate Q estimation of the gas bearing layer is not realistic because the gas bearing layer is also too thin (2420 to 2460m) and there is no receiver pair within this gas bearing layer for interval Q estimation. But we can have some idea about attenuation behavior of this gas bearing layer by studying the amplitude spectra of seismic traces above and below of this zone. Understanding the amplitude behavior is important when studying seismic Q . The amplitude spectra of the traces above, below and within the gas bearing layer examined and interpreted carefully. The Figure-5.14 shows the amplitude spectra of traces at 2420 and 2480m depth levels. The amplitude spectra

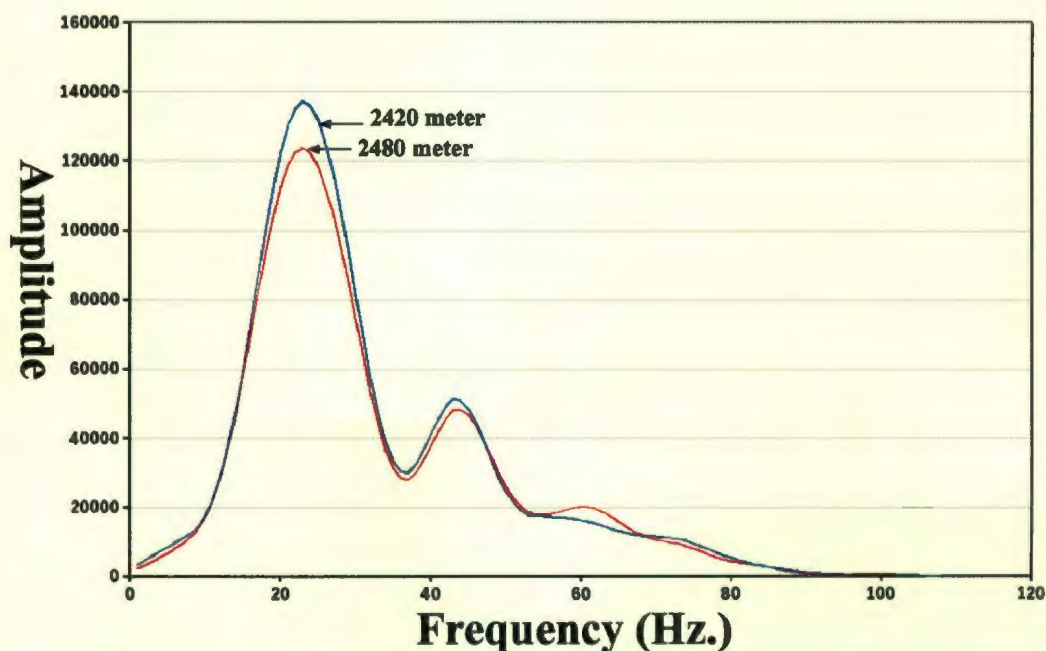


Figure 5.14: Amplitude spectra of the traces recorded at top (2420m, blue line) and bottom (2480m, red line) of the gas bearing zone (2420-2460m)

at 2480m confirmed the amplitude decay is much higher than the spectra at 2420m depth. So it is noted that the gas bearing zone is highly attenuative with huge energy losses from the depth 2420 to 2480m. The shift of the highest peak amplitude towards the low frequencies is also another indication of seismic wave attenuation. It is hard to say about the quantity of attenuation by examining the relative amplitude decay of two traces but one can consider that there might be has some high attenuative media within these receiver pair. The amplitude spectral decay of this zone is very high with respect to other receiver pairs in the total VSP depth. Here we estimated an apparent Q value for the gas bearing zone (2420 to 2460m) choosing the receiver pairs at the top (2420m) and the bottom (2480m) of this zone (Figure-5.15). The Q computed for this zone with SR and CFD method is 28.37 and 23.15 respectively.

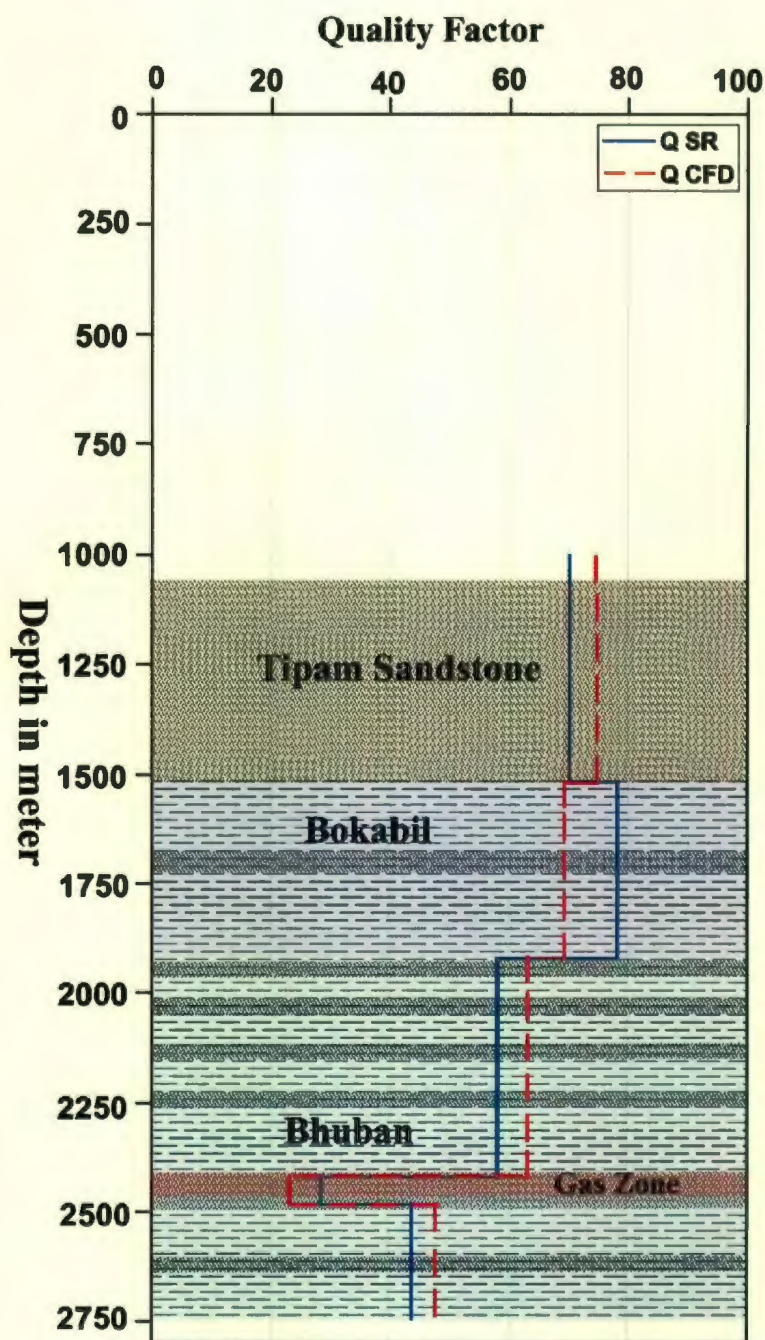


Figure 5.15: Showing the Q -depth profile of each individual formation and apparent Q of the gas bearing zone; SR (blue line) Q estimation is done over 0-35Hz frequency band width and CFD (red line) Q estimation is done over 0-108Hz frequency band width.

5.8 Conclusion

Seismic attenuation analysis of the field VSP data of Lalmai well-3, onshore Bangladesh, has been done by using the SR and CFD methods which have been tested and validated in Chapter-4. The seismic Q estimation of field VSP data is quite satisfactory through the total VSP section but a few receiver pairs represent negative Q values. This physically unrealizable phenomenon of negative values means that the amplitudes of high frequency components are increasing with increasing depth, scattering effect, ambient noise, spectral distortion by imperfect windowing, multiples, interference of other signals or improper choices of receiver pair. In the SR estimation it shows that the Q values are more satisfactory over 0-35Hz frequency band width than 0-100Hz frequency band width. On the other hand the CFD estimation shows better results in wider frequency band width. The larger depth interval gives a better result over a shorter depth interval. The formation boundaries and gas bearing zones have been characterized by carefully interpreting and analyzing all the available borehole data and velocity analysis. The result of formation wise average Q estimation indicates that the lower part (Bhuban formation) and middle part (Bokabil formation) are comparatively higher attenuative than that of the upper part (Tipam formation). The estimated Q of the zone that includes the gas bearing layer (2420-2460m) is remarkably low at about 28 (SR) and 23 (CFD), which represents a highly attenuative zone. It is necessary to take extra care to analyze seismic properties of the highly attenuative thin layer like gas bearing layer. It is proven that thin

layers and layer impurities appreciable affects seismic signal both in size and shape. Reverbration within this thin gas bearing zone has been come from due to thinness of layer and in-layer shale that add some delay and change of amplitude spectra of direct arrival downgoing event. In fact it is a big challenge of understanding, eliminating all these effects from the seismic signal and prepare the data set for precise Q estimation of this highly attenuative thin gas zone. In conclusion, the SR and CFD methods used to estimate attenuation factor in this study is quite successful in both field and model VSP data.

5.9 Suggested Future Work

In this study we applied forward modeling techniques to compute compressional wave attenuation factors. Future work of this study should include: (1) to do attenuation analysis of both zero-offset and far-offset VSP of more complex geological models; (2) to perform S-wave attenuation modeling and (3) to do inverse Q modeling to verify the forward modeling results.

Bibliography

- K. Aki and P.G. Richards. *Quantitative seismology: theory and practice*. W. H. Freeman Co., 1980.
- A. I. Best, C. McCann, and J. Sothcott. The relationships between the velocities, attenuations, and petrophysical properties of reservoir sedimentary rocks. *Geophysical Prospecting*, 42:151–178, 1994.
- R. Dasgupta and R. A. Clark. Estimation of Q from surface seismic reflection data. *Geophysics*, 63:2120–2128, 1998.
- R.W. Graves. Simulating seismic wave propagation in 3d elastic media using staggered-grid finite differences. *Bulletin of the Seismological Society of America*, 86:1091–1106, 1996.
- B. A. Hardage. *Vertical Seismic Profiling: Principles, Third Updated Revised Edition*. Pergamon: An Imprint of Elsevier Science Limited, 2000.
- B.M. Imam and M. Hussain. A review of hydrocarbon habitats in bangladesh. *Journal of Petroleum Geology*, 25 (1):31–52, 2002.
- D. Jannsen, J. Voss, and F. Theilen. Comparison of methods to determine q in shallow marine sediments from vertical reflection seismograms. *Geophysical Prospecting*, 23: 479–497, 1985.
- F. H. Khan. *Geology of Bangladesh*. Wiley Eastern Limited, 1991.
- J. Matsushima. Seismic attenuation from vsp data in methane hydrate-bearing sediments. *The Bulletin of the Australian Society of Exploration Geophysicists*, 38: 29–36, 2007.
- P. Newman. Divergence effects in a layered earth. *Geophysics*, 38:481–488, 1973.
- Y. Quan and J. M. Harris. Seismic attenuation tomography using the frequency shift method. *Geophysics*, 62:895–905, 1997.
- M. Schoenberger and F. K. Levin. Apparent attenuation due to intrabed multiples. *Geophysics*, 39:278–291, 1974.
- M. Schoenberger and F. K. Levin. Apparent attenuation due to intrabed multiples: II. *Geophysics*, 43:730–737, 1978.
- R. E. Sheriff and L. P. Geldart. *Exploration seismology, 2nd Edition*. Cambridge University Press, 1995.

- G. Solana and D. R. Schmitt. Vsp study of attenuation in oil sand. *CSEG National Convention*, 2004.
- S.D. Stainsby and M. H. Worthington. Q estimation from vertical seismic profile data and anomalous variation in the north sea. *Geophysics*, 50:615–626, 1985.
- M. N. Toksoz, D. H. Johnston, and A. Timur. Attenuation of seismic waves in dry and saturated rocks: I, laboratory measurements:. *Geophysics*, 44:681–690, 1979.
- R. Tonn. The determination of the seismic quality factor q from vsp data: a comparison of different computational method. *Geophysical Prospecting*, 39:1–27, 1991.
- H. Trappe. Seismic attenuation in the vicinity of the geothermal anomaly at urach obtained from near-vertical reflection profiles. *Geophysical Prospecting*, 36:149–166, 1988.
- R.E. White. The accuracy of estimating q from seismic data. *Geophysics*, 57:1508–1511, 1992.
- K. Winkler and A. Nur. Pore fluids and seismic attenuation in rocks. *Geophys. Res. Lett.*, 6:1–4, 1979.

Appendix A: Seismic modeling and finite difference formulation

A.1 Equations of Motion

The following sets of equations in time-domain describe wave propagation within 2-dimensional, linear, isotropic elastic media. Equations of momentum conservation:

$$\begin{aligned}\rho\delta_{tt}u_x &= \delta_x\tau_{xx} + \delta_z\tau_{zx} + f_x, \\ \rho\delta_{tt}u_z &= \delta_x\tau_{xz} + \delta_z\tau_{zz} + f_z\end{aligned}\tag{A.1}$$

Stress strain relations:

$$\begin{aligned}\tau_{xx} &= 2\mu\delta_xu_x + \lambda(\delta_xu_z + \delta_zu_x), \\ \tau_{zz} &= 2\mu\delta_zu_z + \lambda(\delta_zu_x + \delta_xu_z), \\ \tau_{xz} &= \mu(\delta_zu_x + \delta_xu_z)\end{aligned}\tag{A.2}$$

Where (u_x, u_z) are the displacement components; (τ_{xx}, τ_{zz}) are the stress components; (f_x, f_z) are the body-force components; ρ is the density; λ and μ are Lamé coefficients; and the symbols δ_x, δ_z and δ_{tt} are shorthand representations of the differential operators $\partial/\partial x, \partial/\partial z$ and $\partial^2/\partial t^2$. These equations can be formulated into a set of 1st-order

differential equations by first differentiating equations (A.2) with respect to time and then substituting the velocity components (v_x, v_z) for the time-differentiated displacements $\delta_t(u_x, u_z)$. The resulting sets of equations are given by

$$\begin{aligned}\delta_t v_x &= b(\delta_x \tau_{xx} + \delta_z \tau_{xz} + f_x), \\ \delta_t v_z &= b(\delta_x \tau_{xz} + \delta_z \tau_{zz} + f_z)\end{aligned}\tag{A.3}$$

where $b = 1/\rho$ is the buoyancy, and

$$\begin{aligned}\delta_t \tau_{xx} &= 2\mu \delta_x v_x + \lambda(\delta_x v_x + \delta_z v_z), \\ \delta_t \tau_{zz} &= 2\mu \delta_z v_z + \lambda(\delta_z v_z + \delta_x v_x), \\ \delta_t \tau_{xz} &= \mu(\delta_z v_x + \delta_x v_z)\end{aligned}\tag{A.4}$$

A.2 Finite-difference implementation

The system of equations (A.3) and (A.4) is easily solved using a staggered-grid finite-difference technique (Graves, 1996). Details of this type of formulation can be found in the above articles, along with numerical accuracy and stability analysis. Figure A1, illustrates the layout of the wave-field variables and media parameters on the staggered-grid mesh. One of the attractive features of the staggered-grid approach is that the various difference operators are all naturally centered at the same point in space and time. Thus, the system is not only staggered on a spatial grid but also temporally, so that the velocities are updated independently from the stresses. This allows for a very efficient and concise implementation scheme. The discrete form of equations (A.3) and (A.4) is given by;

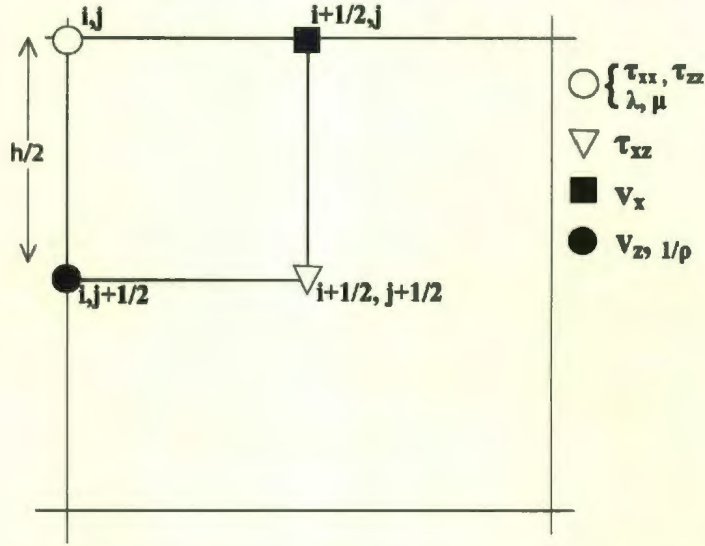


Figure A.1: Grid tensile for staggered-grid formulation. A unit cell consists of the wavefield variables and media parameters that are defined at a specific node. The model space is then made up of series of repeated unit cells that occupy a 2D space. The indices (i, j) represent values of the spatial coordinates (x, y) and the grid spacing h is defined as the length between the centers of two adjacent grid cells.

$$v_{xi+1/2,j}^{n+1/2} = v_{xi+1/2,j}^{n-1/2} + [\Delta t b_x (D_x \tau_{xx} + D_z \tau_{xz} + f_x)]|_{i+1/2,j}^n, \quad (\text{A.5})$$

$$v_{zi,j+1/2}^{n+1/2} = v_{zi,j+1/2}^{n-1/2} + [\Delta t b_z (D_x \tau_{xz} + D_z \tau_{zz} + f_z)]|_{i,j+1/2}^n$$

for the velocities, and

$$\begin{aligned} \tau_{xxi,j}^{n+1} &= \tau_{xxi,j}^n + \Delta t [(\lambda + 2\mu) D_x v_x + \lambda D_z v_z]|_{i,j}^{n+1/2}, \\ \tau_{zzi,j}^{n+1} &= \tau_{zzi,j}^n + \Delta t [(\lambda + 2\mu) D_z v_z + \lambda D_x v_x]|_{i,j}^{n+1/2}, \end{aligned} \quad (\text{A.6})$$

$$\tau_{xxi+1/2,j+1/2}^{n+1} = \tau_{xxi+1/2,j+1/2}^n + \Delta t [\bar{\mu}_{xz}^H (D_z v_x + D_x v_z)]|_{i+1/2,j+1/2}^{n+1/2}$$

for the stresses. In the above equations, the subscripts refer to the spatial indices, and the superscripts refer to the time index. Thus, with a grid spacing of h and a time step of Δt , the expression

$$v_{xi+1/2,j}^{n+1/2} \quad (\text{A.7})$$

represents the x component of velocity evaluated at the point $x = [i + (1/2)]h$, $z = jh$, and at time $t = [n + (1/2)]\Delta t$ (Figure-A.1). We have used a second-order approximation for the time derivatives in these expressions, and the symbols D_x , and D_z represent the discrete forms of the spatial differential operators δ_x and δ_z . Here, we have also introduced the effective media parameters given by:

$$\begin{aligned}\bar{b}_x &= 1/2[b_{i,j} + b_{i+1,j}], \\ \bar{b}_z &= 1/2[b_{i,j} + b_{i,j+1}]\end{aligned}\tag{A.8}$$

for the buoyancy, and

$$\bar{\mu}_{xz}^H = [1/4(1/\mu_{i,j} + 1/\mu_{i+1,j} + 1/\mu_{i,j+1} + 1/\mu_{i+1,j+1})]^{-1}\tag{A.9}$$

for the rigidity. Two important points should be noted regarding the numerical implementation of equations (A.5) and (A.6). First, the differential operators only act on the wave-field variables, not on the media parameters, thus differencing of the media coefficients is not necessary in this scheme, and the complexity of the media has no impact on the form of the differential terms. Second, the time updates are computed such that the velocity field at time $[n + (1/2)]\Delta t$ is determined explicitly from equations (A.5) using the velocity field at time $[n - (1/2)]\Delta t$ and the stress field (and, possibly, body forces) at time $n\Delta t$. At time $(n + 1)\Delta t$, the stress field is then updated explicitly with equations (A.6) from the stress field at time Δt and the previously updated velocity field at time $[n + (1/2)]\Delta t$.



